Ultrafast Deactivation Dynamics of Structurally Modified and Hydrogen-Bonded DNA and RNA Building Blocks

Dissertation

zur Erlangung des Doktorgrades

der Mathematisch-Naturwissenschaftlichen Fakultät

der Christian-Albrechts-Universität zu Kiel

vorgelegt von

Katharina Röttger

Kiel 2013

Erster Gutachter: Prof. Dr. Friedrich Temps
Zweiter Gutachter: Prof. Dr. Jürgen Grotemeyer

Tag der mündlichen Prüfung: 3. Juli 2013
Zum Druck genehmigt: 3. Juli 2013

gez. Prof. Dr. Wolfgang J. Duschl, Dekan

ERKLÄRUNG

Hiermit erkläre ich, dass die vorliegende Abhandlung - abgesehen von der Beratung durch meinen Betreuer Herrn Prof. Dr. Friedrich Temps - nach Inhalt und Form meine eigene Arbeit ist.

Diese Arbeit hat weder in Auszügen noch in ganzer Form einer anderen Stelle im Rahmen eines Prüfungsverfahrens vorgelegen. Sie wurde in ihrer Gesamtheit nicht veröffentlicht und auch nicht zur Veröffentlichung eingereicht. Teile dieser Arbeit wurden in fachwissenschaftlichen Zeitschriften veröffentlicht. Dies bezieht sich auf die folgenden Kapitel:

Kapitel 4
Katharina Röttger, Ron Siewertsen, Friedrich Temps, Ultrafast Electronic Deactivation Dynamics of the Rare Natural Nucleobase Hypoxanthine, *Chem. Phys. Lett.* **2012**, *536*, 140-146.

Kapitel 5
Katharina Röttger, Frank D. Sönnichsen, Friedrich Temps, Ultrafast Electronic Deactivation Dynamics of the Inosine Dimer - A Model Case for H-Bonded Purine Bases, *Photochem. Photobiol. Sci.*, **2013**, DOI: 10.1039/c3pp50093d.

Kapitel 6
Katharina Röttger, Nina K. Schwalb, Friedrich Temps, Electronic Deactivation of Guanosine in Extended Hydrogen-Bonded Self-Assemblies, *J. Phys. Chem. A*, **2013**, *117*, 2469-2478.

Die Arbeit ist unter Einhaltung der Regeln guter wissenschaftlicher Praxis der Deutschen Forschungsgemeinschaft entstanden.

Kiel, im Juli 2013

Katharina Röttger

ABSTRACT

The main goal of the present Thesis was the investigation of the complex interplay of structural modifications and hydrogen bonds on the ultrafast electronic deactivation dynamics of DNA and rare RNA building blocks by means of femtosecond time-resolved transient absorption and fluorescence up-conversion spectroscopy.
(i) The transient absorption experiments on nucleobases called for the design of an improved, highly sensitive setup allowing for simultaneous broadband (near-UV/VIS) and single-color (deep-UV) transient absorption detection. Typical sensitivities of the experiment that was developed in this Thesis were of the order of 2×10^{-5} (broadband) and 5×10^{-6} (single-color).
(ii) The investigation of two structurally modified 6-oxopurines, xanthosine monophosphate (XMP) and hypoxanthine (Hyp), provided detailed insight into the correlation of electronic deactivation channels and substitution at the C(2) position in the purine ring. XMP features a carbonyl bond at the C(2) position and showed a barrierless relaxation through a conical intersection back to the electronic ground state after electronic excitation. The relaxation coordinate was discussed to be the out-of-plane deformation of the 5-membered ring, which is unique among the purine bases. Compared to guanine, Hyp lacks the exocyclic amino group at the C(2) position. It was found to exhibit one of the shortest excited-state lifetimes of purine bases reported so far. The relaxation pathway is expected to proceed along the out-of-plane deformation coordinate of the six-membered ring as is common for purine bases.
(iii) Time-resolved experiments on several dimers and larger aggregates in aprotic solvents provided basic insight regarding the influence of hydrogen bonds on the ultrafast deactivation dynamics of nucleobases. As a basic model system, the symmetric dimer of Hyp was investigated. The observed dynamics were similar to those of the monomer, presumably because neither the C(2) nor the N(3) atoms are involved in the dimerization. A completely different picture emerged for the electronic deactivation of larger guanine aggregates. Here, a complex excited-state depopulation on time scales spanning four orders of magnitude was observed. This revealed large modifications of the excited-state topography and energetic shifts compared to monomeric guanine, showing the outstanding influence of hydrogen bonds on the deactivation of guanine. Experiments on the excited-state dynamics of the Watson-Crick G·C dimer gave evidence for the formation of a $(G{-}H)^{\cdot}$ radical, which is possibly the first direct observation of an electron-driven proton transfer process in the Watson-Crick G·C base pair.

ZUSAMMENFASSUNG

Das Hauptaugenmerk dieser Dissertation lag auf der Untersuchung des komplexen Zusammenspiels von strukturellen Modifikationen und Wasserstoffbrückenbindungen auf die ultraschnelle elektronische Desaktivierung von DNA- und RNA-Bausteinen durch Femtosekunden-zeitaufgelöste transiente Absorptionsspektroskopie und Fluoreszenzaufwärtskonvertierung.
(i) Die transiente Absorptionsspektroskopie an Nukleobasen erforderte die Entwicklung eines neuen, hochempfindlichen experimentellen Aufbaus, der die gleichzeitige breitbandige (UVA/vis) und Einzelfarben-Detektion (UVB-UVC) erlaubt. Typische Empfindlichkeiten des in dieser Arbeit entwickelten Experiments lagen in der Größenordnung von 2×10^{-5} (Breitband) and 5×10^{-6} (Einzelfarbe).
(ii) Die Untersuchung zweier strukturell modifizierter 6-Oxopurine, Xanthosin-Monophosphat (XMP) und Hypoxanthine (Hyp), erlaubte einen detaillierten Einblick in den Zusammenhang der Substitution an der C(2)-Position im Purin-Grundgerüst mit elektronischen Desaktivierungskanälen. XMP besitzt eine Carbonylgruppe an der C(2)-Position und zeigt nach elektronischer Anregung eine barrierelose Relaxation in den elektronischen Grundzustand durch eine konische Durchschneidung. Als Relaxationskoordinate wurde die Deformationsschwingung des 5-Rings diskutiert, was unter den Purinbasen einzigartig ist. Im Vergleich zu Guanine besitzt Hyp keine exozyklische Aminogruppe an der C(2)-Position. Für dieses Molekül wurde eine der kürzesten für Purinbasen bisher bekannten Lebensdauern im elektronisch angeregten Zustand gefunden. Die Relaxationskoordinate ist wahrscheinlich wie bei anderen Purinbasen eine Deformationsschwingung des 6-Rings.
(iii) Zeitaufgelöste Messungen an verschiedenen Dimeren und größeren Aggregaten in aprotischen Lösungsmitteln lieferten grundlegende Informationen über den Einfluss von Wasserstoffbrücken auf die ultraschnelle elektronische Desaktivierung von Nukleobasen. Das Hyp-Dimer wurde hierbei als elementares Modellsystem untersucht. Die gefundene Dynamik ist ähnlich zu der des Monomers, wahrscheinlich da weder die C(2)- noch die N(3)-Position an der Dimerbildung beteiligt sind. Ein anderes Bild ergibt sich für die elektronische Desaktivierung von größeren Guanin-Aggregaten. Hierbei wurde eine komplexe Depopulation des angeregten Zustandes beobachtet, die sich auf Zeitskalen über vier Größenordnungen erstreckt. Die Ergebnisse lassen auf ausgeprägte Modifikationen der Topographie der angeregten Zustände und mögliche Verschiebungen der Energieniveaus schließen. Dies zeigt den außergewöhnlichen Einfluss von Wasserstoffbrücken auf die Desaktivierung von Guanin. Experimente am Watson-Crick G·C Basenpaar zur Dynamik im angeregten Zustand ergaben Hinweise auf die Bildung eines $(G{-}H)^{\bullet}$-Radikals. Dies ist möglicherweise die erste direkte Beobachtung eines Elektronen-getriebenen Protonentransfers im G·C Basenpaar.

CONTENTS

Part I

INTRODUCTION AND EXPERIMENTAL DETAILS

1 INTRODUCTION

The complexity of life on Earth is encrypted by the stunningly small number of four building blocks, the nucleobases. They constitute the deoxyribonucleic acid (DNA), which comprises all information that is necessary for the functions of a living organism. The entirety of DNA, the genome, is in case of the human genome made up of two main parts, the nuclear genome and the mitochondrial genome. The former is present in the nuclei of cells and consists of some 3000000000 nucleobases organized in 24 chromosomes, including about 35000 protein-encoding parts, which are called genes. The mitochondrial genome is a circular DNA molecule located in the mitochondria and it consists of some 17000 nucleobases forming 37 genes. The complete sequence of the humane genome was obtained in an international research project, the Humane Genome Project, which ended in 2003.[1–3] However, a complete understanding of the protein-coding and non-coding functions of the genome is a challenging scientific task, and another international research project, the ENCODE (Encyclopedia of DNA Elements) consortium, is presently working on that task.[4,5]

Generally, the genome expression starts with the transcription of protein-encoding DNA parts into ribonucleic acid (RNA) and the resulting so-called transcriptome is subsequently translated into proteins. The overall process of genome expression is based on an interplay of a multitude of proteins and special RNA molecules. DNA and RNA are both highly complex systems with a humongous variety of structural modifications, biochemical functions and photophysical properties. The complete understanding in each of these fields, not to mention the interplay of all properties and functions, is still missing. A detailed description is beyond the scope of the present Thesis, but is given in a number of textbooks.[6–8]

The present Thesis is concerned with the inherent molecular dynamics of some of the simplest building blocks of DNA and RNA after excitation by absorption of UV light. The focus lies on single purine bases with structural modifications (rare natural bases), and on small-sized hydrogen bonded assemblies. This Introduction gives a concise overview of general structural properties of DNA and RNA, and summarizes the current state of knowledge regarding the photochemical and photophysical properties of single purine and pyrimidine bases and larger, in particular hydrogen-bonded aggregates that are related to the work in this Thesis.

1.1 STRUCTURAL PROPERTIES OF DNA AND RNA

The monomeric building blocks of DNA are composed of three subunits, which are (i) one of the four nucleobases guanine (Gua), adenine (Ade), thymine (Thy) or cytosine (Cyt), (ii) β-D-2′-deoxyribose, and (iii) a phos-

phate group. The four DNA bases are depicted in Figure 1.1. The free nucleobases are connected to the deoxyribose unit via an *N*-glycosidic bond, thus forming the four nucleosides deoxyguanosine (Guo, G), deoxyadenosine (Ado, A), thymidine (Thd, T) and deoxycytidine (Cyd, C). Nucleosides with a phosphate group attached to the 5′ position of the ribose via an ester bond are called nucleotides or nucleoside monophosphates, i.e., deoxyguanosine monophosphate (dGMP), deoxyadenosine monophosphate (dAMP), thymidine monophosphate (TMP) and deoxycytidine monophosphate (dCMP).[1] In a single DNA strand, the backbone is formed

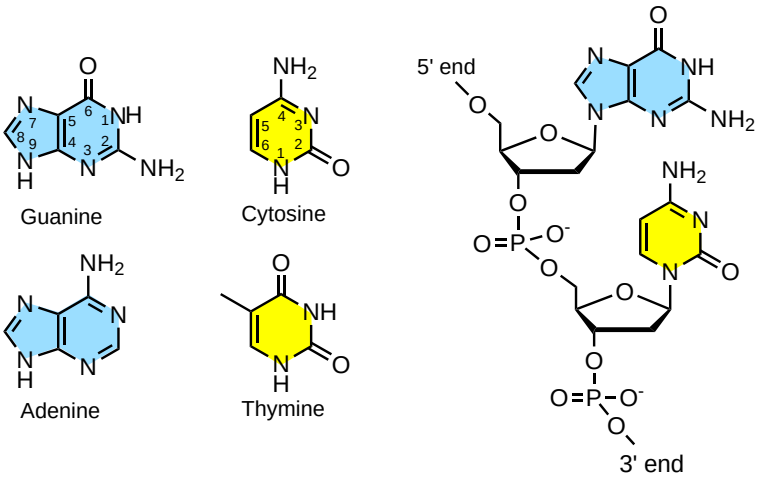

Figure 1.1: Structures of the four DNA bases with the common numbering scheme of the purine and pyrimidine backbones (highlighted in blue and yellow), respectively. On the left hand side, a single DNA strand composed of guanine and cytidine is shown.

by phosphate ester bonds of one nucleotide with the 3′ OH group of the adjacent nucleotide (Fig. 1.1). In RNA, thymine is replaced by uracil (Ura) and the sugar is β-D-ribose instead of deoxyribose. The latter difference has several implications on the structure as well as the function of RNA: The additional hydroxy group at the 2′ position enables the branching of RNA strands by forming phosphate ester bonds at the 2′, 3′ and 5′ position, resulting in a greater variety of possible structures and functions compared to DNA. The flexibility of RNA, on the other hand, is reduced by the steric constraints induced by the additional functional group. Some of these topics will be discussed in the following Sections. Besides the four main nucleobases G, A, C and U, RNA consists to ≈ 10% of rare natural nucleobases.[9]

DNA normally exists double stranded, i.e., two single strands form a double helix structure which is stabilized by hydrogen bonds between the single strands. Usually, these hydrogen bonds are formed between in G·C and A·T base pairs in the so-called Watson-Crick (WC) configuration, displayed in Figure 1.2. The WC base pairing allows for a reliable replication and translation, and the two WC base pairs fit almost perfectly in

1 Throughout this Thesis, the abbreviations G, A, C and T will be used synonymously for free nucleobases, nucleosides and nucleotides where the meaning is obvious from context.

any sequence in the double helix structure.[10] Besides this binding pattern, non-standard base pairs in (reverse) Hoogsteen, wobble, or reverse WC configurations are also known to exist in DNA double strands and telomeres,[9–16] and in different RNA double strands such as in tRNA and rRNAs.[9,10,16] In DNA, these mismatches are potentially mutagenic and are removed by enzymatic repair mechanisms.[9,16] Every nucleobase features several hydrogen bonding donor and acceptor sides, as shown in Figure 1.2. This enables DNA and RNA double strands to form additional hydrogen bonds, e.g., to proteins or to a third single strand, resulting in triple helices.[7–9,16]

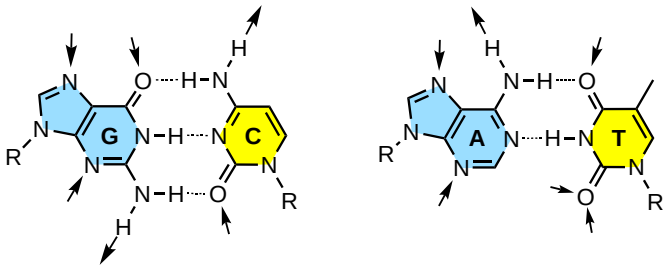

Figure 1.2: Structure of the Watson-Crick (WC) base pairs. Arrows depict potential hydrogen bonding sites that are not incorporated in the WC base pair. Arrows point away from donor and toward acceptor sites.

The DNA double helix exists mainly as A-, B-, or Z-DNA, each featuring a set of individual characteristics including helix handedness and twist, diameter, groove depths, and sugar conformation. The details for each helix structure can be found in common textbooks,[6,7,9,10,16] and only the main features will be discussed in the following. Generally, the double helix, formed by hydrogen bonds between complementary nucleobases, is a structure where the nucleobases are oriented to the inside of the double helix and the negatively charged phosphate groups are located on the outside. Within the single strands, stacking interactions of the aromatic purine and pyrimidine rings occur. In A- and B-DNA, the helix structure is insensitive to the nucleobase sequence, whereas Z-DNA is formed preferentially in regions with alternating purine-pyrimidine sequences, mainly G and C.[10] In all double helix types, the two single strands run in opposite directions regarding the sugar-phosphate backbone (Fig. 1.3(a)). The aromatic systems of the nucleobases in B-DNA are nearly parallel to each other, which can be seen in Figure 1.3(b). However, the relative orientation of adjacent nucleobases depends on helix type and base sequence in case of A- and B-DNA.[10,17] Z-DNA was found to be more rigid, as long as the purine-pyrimidine alteration is undisturbed.[17] Details of the distribution of local orientations for each helix type are given by, e.g., Bloomfield[10] and Shakked.[17] In Figure 1.3(c), the B-DNA is depicted as calotte model with colored nucleobases and a black sugar-phosphate backbone. In this representation, two important structural features of B-DNA can be seen: First, the helix structure leads to the formation of a major and a minor groove that coil around the helix. Secondly, the hydrogen bonding donor

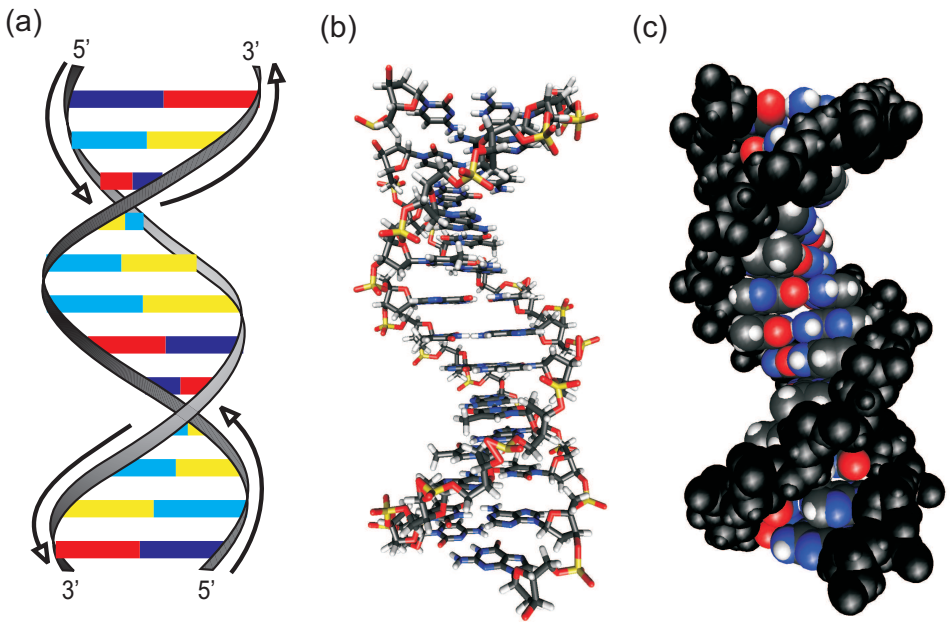

Figure 1.3: Structure of B-DNA. (a) Schematic representation. The $5' \rightarrow 3'$ directions of the sugar-phosphate backbone are indicated by arrows. (b) Molecular structure. (c) Calotte model. The sugar-phosphate backbone is shown in black, oxygen atoms in red and nitrogen atoms in blue. Carbon and hydrogen atoms are depicted in dark and light gray, respectively.

and acceptor sides, which are not incorporated in the WC base pairs in the inner helix, point to the outside and are thus accessible for hydrogen bond formation. This feature is prerequisite for the formation of DNA-protein complexes, which play crucial roles during a number of processes like replication and repair of DNA, transcription initiation and regulation, and functions during the translation process.[8,10]

1.2 EXCITED-STATE DYNAMICS OF DNA AND RNA BUILDING BLOCKS

The absorption of sunlight by living organisms leads to a number of important reactions such as the conversion of CO_2 to O_2 during photosynthesis or the process of vision. In case of DNA, however, absorption of UV-photons potentially induces irreversible photochemical reactions leading to a damage of the genetic code. Among these reactions is the well-known intrastrand dimerization of pyrimidine bases, especially thymine,[18–22] which occurs barrierless in less than 1 ps in case of pre-oriented molecules as given in stacked thymine molecules in a DNA single strand.[23–26] Whether the involvement of triplet states in this reactions is necessary for dimerization of thymine[26,27] as well as for cytosine is still a matter of debate.[28] Another important photoproduct is the $6-4$-dimer of adjacent pyrimidine bases,[6,8,29] which is potentially more lethal for humans since the repair enzyme (6-4) photoproduct photolyase is missing.[8] Beside dimerization, the formation of oxidation products such as 8-oxo-7,8-dihydroguanine (8-oxoguanine) is possible under oxidative conditions in-

duced by, e.g., high-energy radiation.[30–34] These structural modifications affect replication and genome expression and consequently are potentially carcinogen or mutagen, if not repaired by suitable enzymatic mechanisms. However, the restoration of the original structure is costly for organisms.

Beside enzymatic repair, intrinsic protection mechanisms lead to a drastic reduction of quantum yields of photochemically induced lesions to $\Phi_{\text{reac}} \leqslant 10^{-3}$.[35] A hint at the origin of the low amount of structural changes upon UV absorption is given by the fluorescence quantum yields of the nucleobases, which are of the order of $\Phi_{\text{fluo}} \approx 10^{-4}$, thus indicating very short excited electronic state lifetimes.[36] The investigation of molecular dynamics on the respective picosecond to femtosecond time scales became feasible some 20 years ago with the development of femtosecond lasers and suitable spectroscopic techniques.[37–39] Since then, a picture has emerged in which electronic excitation of DNA building blocks by absorption of UV photons is followed by an ultrafast deactivation through conical intersections (CI), leading to an ultrafast dissipation of energy to the surrounding molecules. Conical intersections are non-adiabatic crossings of potential energy surfaces and play a major role in almost all photophysical processes of organic molecules where internal conversion to lower electronic states occurs on a sub-picosecond timescale.[40–43]

The current understanding of excited-state dynamics of DNA is based on a systematic investigation of small DNA model systems, i.e., naturally occurring and/or structurally modified monomers, H-bonded or π-stacked dimers, microhydrated nucleobases in the gas phase, and larger aggregates composed of several structure-determining monomer units. Many of them turned out to be useful to gain insight into the complex interplay of several aspects of DNA structure.[44–46]

1.2.1 DYNAMICS OF SINGLE DNA BASES

The investigation of photophysical behavior after electronic excitation of the four naturally occurring DNA bases forms the basis for studies of larger systems with inter-base interactions such as hydrogen-bonding and π stacking. The picture emerging from the last $\approx$ 15 years of research on these molecules permits a coarse partition into purine and pyrimidine deactivation mechanisms.[44,45,47]

In general, the lowest-lying electronic transitions in all nucleobases are two close-lying optically bright $\pi\pi^*$ transitions.[48] Additionally, one or more $n\pi^*$ transitions, due to numerous heteroatoms with electron lone pairs, can be observed.[48] Moreover, triplet states may also play a role, especially for the deactivation of pyrimidine bases.[49–53] The relative ordering of these states depend on the nucleobase and on solvent polarity. All of these states play a significant role in the ultrafast deactivation of electronically excited nucleobases. This will be discussed in the following for the purine and the pyrimidine bases. Special attention is given to guanine and cytosine, owing to their relevance for the results presented in the second part of this Thesis. The focus in this Chapter lies on the theoretical

results, as the most important experimental findings will be discussed in context with the presently obtained results below.

Dynamics of Purine Bases

The purine bases feature two optically bright $\pi\pi^*$ transitions categorized as ^1L_a and ^1L_b depending on the relative orientation of the transition dipole moment.[54] Both naturally occurring purine bases adenine and guanine are known to exist as a mixture of several keto, imino and enol tautomers in the gas phase[55–61] and as 7H and 9H keto tautomers in aqueous solution.[62,63] The following discussion of the photophysics of guanine will concentrate on the 9H tautomer of guanine, since this is the canonical (i.e. naturally occurring) tautomer.

A number of *ab initio* and molecular dynamics simulations were dedicated to the deactivation mechanism after population of the Franck-Condon regions.[47,64–77] Most theoretical studies agree on the importance of a direct relaxation from the initially prepared $\pi\pi^*$ state to the electronic ground state. The two dominating pathways are (i) the relaxation via an out-of-plane-deformation of the six-membered ring by out-of-plane motion of the C(2) atom, and (ii) a distortion of the exocyclic amino group.[47,64–77] Additionally, the involvement of several close-lying optically dark states with $\pi\sigma^*$ and $n\pi^*$ character in the electronic deactivation mechanism is discussed in a number of *ab initio* and molecular dynamics simulations.[68–72] In particular, Barbatti et al. found in surface hopping simulations in the gas phase a deactivation via an $n\pi^*$ state located at the carbonyl group for $\approx$ 5 % of the population. The deactivation was found to take place on the time scale of some hundred femtoseconds for the direct relaxation pathways, which is in good agreement with experimental results in the gas phase.[72] However, the accessibility of $n\pi^*$ and $\pi\sigma^*$ states in water is questionable, although in a recent experimental study the latter has been discussed to be populated during the deactivation of guanine in water.[78] Marian proposed the population of a Rydberg-like state with diffuse charge distribution during electronic deactivation. This charge distribution would be stabilized by the large static dipole moment of 6.8 D.[68]

Experimental measurements of excited lifetimes of guanine in the gas phase by femtosecond time-resolved pump-probe resonant ionization revealed a bifurcation of excited-state lifetimes into 0.148 ± 0.015 and 0.36 ± 0.04 ps.[79] In an earlier study, a lifetime of 0.8 ps was found.[80] Canuel et al.[79] in accordance with Serrano-Andrés et al.[69] and Barbatti et al.[72] attributed the faster decaying components to the rapid relaxation via the $(\pi\pi^*(L_a)/gs)$ CI and the slightly longer component to the population of an optically dark $n\pi^*$ state, possibly via an $n\pi^*/\pi\pi^*(L_b)$ state switch.

A recent QM/MM dynamics simulation in water[77], in accordance with surface-hopping calculations in the gas phase,[72,75] also predicted the direct deactivation via deformation of the six-membered ring, mainly by an out-of-plane motion of the C(2) atom, and the out-of-plane displacement of the exocyclic amino group to be the most important pathways in water.

The respective calculations showed that approximately two thirds of the initial population of the Franck-Condon region in the $\pi\pi^*(L_a)$ state decay via the former pathway, while one third follows the latter mechanism to reach a CI with the electronic ground state.

Recent studies of GMP in aqueous solutions measured fluorescence lifetimes of 0.16 ps and $\leqslant$ 3 ps[81] and transient absorption decays of $\approx$ 0.2 ps, $\approx$ 1 and 2.5 ps.[74] Previous investigations of guanosine and GMP in aqueous solution yielded mono-exponential excited-state decay within $0.46 \pm 0.04 - 0.69 \pm 0.1$ ps.[82–84] The proposed relaxation mechanism on the basis of these experimental findings and theoretical predictions (see above) is an initial, ultrafast transition from the upper $\pi\pi^*(L_b)$ to the lower $\pi\pi^*(L_a)$ in $\leqslant$ 100 fs. The ensuing dynamics are governed by a direct relaxation to the electronic ground state through a $(\pi\pi^*(L_a)/gs)$ CI within some hundreds of femtoseconds. The somewhat different findings from fluorescence and transient absorption measurements are probably due to the existence of one or more shallow, optically less bright minima or plateaus on the $\pi\pi^*(L_a)$ surface, where part of the excited-state population might be trapped for some picoseconds. The involvement of $n\pi^*$ states in the relaxation mechanism was predicted to be less likely in aqueous solution.[74] In the most recent combined transient absorption and fluorescence decay study of guanosine and GMP in water and methanol, the authors claimed the population of a longer-lived weakly emissive state to be responsible for the complex behavior.[78] In their picture, the direct relaxation mechanism via the above discussed $(\pi\pi^*(L_a)/gs)$ CI competes with a relaxation via a supposed $\pi\sigma^*$ state located at the exocyclic amino group.

The dynamics of 9H adenine follow an analogous relaxation route. The dynamics have been investigated in a number of theoretical and experimental studies.[85–96] Most authors agree that in aqueous solution, the relaxation of the 9H-Ade starts with an ultrafast depopulation of the FC region on the initially populated $\pi\pi^*(L_a)$ state. This relaxation seems to occur within $\leqslant$ 100 fs. Subsequently, a ring distortion at the six-membered ring similar to that found for guanine leads to a conical intersection with the electronic ground state, resulting in a sub-picosecond electronic lifetime. Another deactivation routes involve transitions to the close-lying, optically dark $n\pi^*$ and the $\pi\pi^*(L_b)$ states, but these are less favored in aqueous environments.

Dynamics of Cytosine

The photodynamics of the pyrimidine bases after excitation into the optically bright $\pi\pi^*$ state have been the subject of a lively discussion over the last ten years. The picture is governed by a number of ab initio quantum chemical studies and QM/MM dynamics simulations on the one hand and thorough experimental investigations of cytosine and several derivatives. A detailed and comparative summary of the state of knowledge until 2010, especially from the theoretical point of view, was given by González-Vázquez and González.[97] The situation in cytosine is characterized by the existence of at least three close lying excited states, namely the $\pi\pi^*$, $n_N\pi^*$

and $n_O\pi^*$ states.[97–109] Further complication arises from the existence of triplet states, whose involvement in the deactivation dynamics is discussed as well.[49,51–53] The relative ordering of these states strongly depends on calculation method and molecular geometry, but most theoreticians identified the $\pi\pi^*$ state as the lowest in energy in the Franck-Condon region, at least in the gas phase.

One possible decay route after electronic excitation of cytosine starts with an ultrafast radiationless decay of the initial $\pi\pi^*$ population towards a two-state[100,105–107,109] or three state[101,108] conical intersection with the electronic ground state. Some of these pathways were found to include a minimum or barrier on the order of $\approx 0.1 - 0.2$ eV en route to the ($\pi\pi^*$/gs) CI.[106,107,109] The most likely structure at the two-state CI is characterized by torsion of the C_5-C_6 bond, which leads to a biradical or zwitterionic geometry similar to the one found for the deactivation of ethylene.[106,107] Zgierski et al. proposed the population of an additional state with biradical character before repopulation of the electronic ground state.[103,104,110] Other relaxation mechanisms include the population transfer to optically dark $n_O\pi^*$ and $n_N\pi^*$ states via ($\pi\pi^*$/$n\pi^*$) CIs and possible adiabatic state switches from $n_O\pi^*$ to $n_N\pi^*$ states. The subsequent decay to the electronic ground state takes place through ($n_O\pi^*$/gs) and ($n_N\pi^*$/gs) CIs.[99,100,102,105–107]

In aqueous solution, this picture does not change dramatically, although the solvent leads to a stabilization of the $\pi\pi^*$/gs CI with its biradical, zwitterionic character.[111–114] This is expected to make the direct relaxation more likely than the deactivation routes including $n\pi^*$ states, but the latter are still energetically accessible.

Several recent molecular dynamics simulations allowed a closer look on the relative populations and decay times of the relaxation pathways mentioned above in the gas phase as well as in aqueous solution.[97,109,114–116] Experimental time-resolved experiments in the gas phase and in (aqueous) solution such as transient absorption and fluorescence measurements revealed indeed complex dynamics on a variety of time scales ranging from sub-picosecond decay times to excited-state lifetimes of some hundred picosecond.[82–84,117–124] A discussion of these results in comparison with the results obtained for the deactivation of cytidine in $CHCl_3$ is given in Chapter 7.

The relaxation pathways for thymine and uracil are similar, though not necessarily equal,[103,105,125–132] and attempts have been made to find a unified relaxation mechanism for all pyrimidine bases.[105]

1.2.2 Dynamics of structurally modified purine bases

Structural modification of the six-membered ring is of special interest since the most important deactivation pathways of adenine and guanine involve a distortion located at this ring. Two structurally modified purine bases, namely hypoxanthine and xanthine, have been studied in this Thesis in this context. The results, together with discussions of the present state

of knowledge regarding these molecules, can be found in Chapters 3, 4 and 5. Two of the most prominent and well-known examples of purine derivatives are the adenine isomer 2-aminopurine (2AP) and the alkylated species *N,N*-dimethyladenine (DMA), shown in Figure 1.4. These two mo-

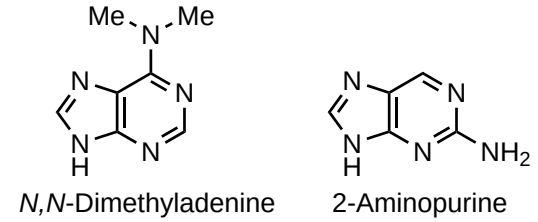

Figure 1.4: Structures of 2-aminopurine and *N,N*-dimethyladenine.

lecules show the large impact of structural modifications on the deactivation of purine bases.

2-Aminopurine has been the subject of several experimental and computational studies. The results show a dramatic increase of the electronic lifetime to $\approx$ 10 ns and possibly a substantial alteration of the deactivation mechanism compared to adenine.[91,133–140] 2AP exists in two tautomeric forms, 9H-2AP and 7H-2AP, of which the former seems to be the dominant species in the gas phase[141] and in solution.[135] Although a number of theoretical and experimental studies dealt with 2AP, there is still some confusion about the energetic ordering of the three lowest electronic states. Serrano-Andrés et al. claimed on the basis of *ab initio* calculations the optically bright $\pi\pi^*(L_a)$ state to be the lowest at the ground state minimum geometry, followed by an optically dark $n\pi^*$ and the $\pi\pi^*(L_b)$ state. They predicted, in agreement with Perun et al., the deactivation via a distortion mode of the six-membered ring, i.e., twisting of the endocyclic CN bonds and therefore a large movement of the C(2) atom, and a direct deactivation via a $\pi\pi^*(L_a)$/gs conical intersection.[91,137] The drastically increased lifetime compared to adenine is explained by the existence of a minimum on that pathway, which leads to a substantial energy barrier of several kJ/mol due to the sterical hindrance induced by the large amino group at the C(2) position. After excitation to the $\pi\pi^*(L_b)$ state, a conical intersection leads to a population of the $\pi\pi^*(L_a)$ state and subsequent relaxation back to the electronic ground state. This was discussed by the authors to be responsible for the different lifetimes found in transient absorption measurements of 2AP in aqueous solution.[142] Additionally, the initially populated $\pi\pi^*(L_a)$ and the intermediate $n\pi^*$ states exhibit dipole moments whose orientation differ considerably from that of the electronic ground state in case of 2AP.[137] Therefore, a large solvent rearrangement can be expected upon electronic excitation, which would explain some of the dramatic differences of adenine and 2AP, as was discussed by Perun et al.[137,143]

In summary and following the authors of the above discussed works, the structural alteration leads to a change of the excited-state topography, but not to an altogether different deactivation channel compared to adenine.

Two recent experimental investigations in the gas phase using resonant two-photon ionization (R2PI) revealed a different picture.[136,140] Lobsiger et al. found the $n\pi^*$ state to be 1.08 eV lower in energy than the $\pi\pi^*(L_a)$ state.[140] They showed in accordance with Seefeld et al.[136] the population of a triplet state with a lifetime of $\geqslant 5$ µs during relaxation from the initially excited $\pi\pi^*(L_a)$ state which is not observed in the case of 9H adenine. Additionally, population of the optically dark $n\pi^*$ state via a non-radiative decay channel state was also observed by Lobsiger et al. and Feng et al.[139] for 9H-2AP. These results, although not unambiguous in their interpretation, show the impact of the substitution pattern in the purine system. Not only is the energetic ordering of excited states different for 9H-Ade and 2AP, but also the couplings of these states and consequently the relaxation pathways.

A detailed study of the adenine derivative *N,N*-dimethyladenine was carried out using time-resolved fluorescence measurements by Schwalb et al.[144,145] and the results were confirmed by time-resolved transient absorption spectroscopy.[146,147] The fluorescence measurements revealed a complex excited-state topography and several fluorescence decay times ranging from the femtosecond to nanosecond time scale. The dual fluorescence observed in the static fluorescence spectra as well as in time-resolved experiments is attributed to the population of a locally excited (LE) state and a subsequently populated intramolecular charge transfer (ICT) state that is not accessible in 9H-Ade. This is explained by the enhanced electron donor and acceptor qualities of the dimethyl-amino group and the six-membered ring, respectively.[148–150] Beside this deactivation channel, a direct relaxation comparable to the one found for 9H-Ade and population transfer to an $n\pi^*$ or $\pi\pi^*(L_b)$ state was observed in the time-resolved fluorescence measurements, but not in the transient absorption experiments. However, both studies agree that the deactivation differs dramatically from that of 9H-Ade, again showing the strong dependence of excited-state topography and couplings on the substitution of the purine ring.

1.2.3 Dynamics of hydrogen-bonded assemblies

Hydrogen bonds are known to have a large impact on the photophysics of purine and pyrimidine bases. Regarding the number of heteroatoms and hence hydrogen-bonding acceptor and donor sides in the nucleic acid bases, it is not surprising that hydrogen bonds are ubiquitous in DNA and RNA. In natural systems, they exist as inter-strand H-bonds between complementary bases in DNA double helices,[151,152] they can form a variety of complexes with water[153–155], they are responsible for a number of DNA-protein interactions and for triplex and quadruplex formation.[9,156–160]

A number of theoretical and experimental studies are concerned with possible structures, binding energies and solvatochromic shifts of complexes between nucleic acid bases and water molecules.[113,161–169] The *dynamical* changes upon hydrogen bonding are investigated in different systems and environments. Canuel et al.[92] compared deactivation pathways

of isolated and hydrated 9-methyladenine by time-resolved photoelectron imaging spectroscopy and mass-selected ion spectroscopy. The relaxation pathway changed dramatically upon complexation with water: The direct relaxation via a $\pi\pi^*$/gs CI became the dominant one, whereas for the isolated base, the relaxation occurs mainly through a $\pi\pi^*/n\pi^*$ state switch and subsequent decay to the electronic ground state.[92] A similar behavior was found for complexed guanine.[74,79]

Shukla et al. calculated changes of the lowest $\pi\pi^*$ states of guanine upon complexation with a different number of water molecules and found remarkable changes in the excited state geometry of hydrated guanine compared to uncomplexed guanine.[162,170] A recent dynamics simulation by Zelený et al. revealed the influence of hydrogen bonding on the photophysics of guanine and cytosine.[76] The electronic lifetime of guanine was found to be increased from 0.22 ps for the free base to $\geqslant$ 0.5 ps for the guanine incorporated in a DNA double helix. Regarding the geometrical distortions of the amino group that is expected to be necessary for the electronic deactivation of guanine, this result is not surprising, though by no means less important. In the same study, the dynamics of cytosine were found to be nearly unchanged upon incorporation in a double strand. This was explained by the smaller spatial requirements for the ring puckering that is the major relaxation route for the electronic deactivation of cytosine.[76] Vibrational excess energy is generally more efficiently dissipated in the presence of a water shell, in some cases accompanied by proton transfer or dissociation.[154,155,171]

Beside the formation of complexes with surrounding water molecules, the pairing of nucleic acid bases with each other is important. A number of model systems have been investigated and the findings revealed a rather complex and heterogeneous picture. In 1965, Löwdin et al. predicted on the basis of theoretical considerations that a double proton-transfer (DPT) process might occur within DNA base pairs. Experimentalists and theoreticians indeed observed this process for the deactivation of 7-azaindole dimers, which are regarded as simple model systems for DNA base pairs.[172–177] Whether DPT occurs via a stepwise or a concerted mechanism is still a matter of discussion. This model system, however, lacks amino groups that are involved in the natural occurring Watson-Crick base pairing of A, T, G and C.

Sobolewski, Domcke, Yamazaki and coworkers predicted this amino group to be an important factor for the electronic deactivation of the G·C base pair in its Watson-Crick conformation.[178–181] They assumed that an electron-coupled proton transfer between G and C occurs en route to the electronic ground state. This reaction starts with excitation of the guanine and a subsequent electron transfer to cytosine. This charge-transfer (CT) state leads efficiently to a conical intersection with the electronic ground state via a proton transfer from the guanine radical cation to the cytosine radical anion along the central H-bond. Several dynamics simulation studies confirmed this picture.[182–185] In all cases, the major part of all trajectories decayed to the electronic ground state via an electron-driven

proton transfer (EDPT) process within some hundred femtoseconds. After crossing the conical intersection with the electronic ground state that comes along with an electron transfer back to G, the energetic minimum is reached by a back-transfer of the central proton and the initial structure is restored.[182]

Shortly after the first prediction of an EDPT reaction in the WC G·C base pair and the 2-aminopyridine dimer (2APy·2APy), Schultz et al.[186] studied the electronic deactivation of the latter system via femtosecond time-resolved mass spectroscopy. Indeed, they found a single proton transfer to be responsible for the relaxation to the electronic ground state. A number of subsequent experimental and theoretical studies by Schultz and coworkers confirmed this picture.[187,188]

Abo-Riziq et al. found a strong broadening of UV absorption in IR-UV hole burning experiments of the WC G·C dimers in the gas phase, which can be seen as a strong hint for a dramatic shortening of excited-state lifetimes compared to other, non-WC conformations.[189] Time-resolved fluorescence measurements of the G·C dimer in $CHCl_3$ showed a reduction of lifetimes compared to the monomer deactivation.[190,191] The lifetime of the optically bright state, which was extracted from the data, was 300 fs and hence in good agreement with the results obtained in the dynamics simulations.[182–185] Recently, Biemann et al. published a combined study of time-dependent density functional theory (TD-DFT) calculations, taking into account the solvent with the polarizable continuum model (PCM), and transient absorption measurements on the deactivation of the G·C base pair in $CHCl_3$. They claimed an EDPT process to be unlikely in solution due to high energy barriers. Their study, however, is incomplete because they excited the dimer at an excitation wavelength of 283 nm, which leads to an excitation mainly of C. Since the EDPT process starts with a charge transfer from G to C, this is a possible reason for the small difference found for the dimer and monomer transient absorption signals. The employment of PCM instead of a QM/MM treatment, where couplings of solute and solvent are considered, might also lead to an underestimation of the importance of EDPT in the deactivation of the G·C base pair, as the authors themselves claimed.[192]

There are several theoretical studies that are concerned with the accessibility of a double-proton transfer in the G·C base pair.[181,193,194] Yamazaki and Taketsugu discussed the feasibility of all possible reactions upon excitation of the G·C base pair with UV photons, i.e., (i) monomer-like deactivation via G and C like deactivation pathways, (ii) the electron-driven proton transfer described above, (iii) single-proton transfer from C to G, and (iv) double-proton transfer.[181] In this study, the monomer-like deactivation and EDPT pathways were found to be equally accessible, while the latter two seems to be more unlikely due to high potential energy barriers. In Chapter 7, the results for electronic deactivation of the G·C base pair will be discussed in context of transient absorption experiments on that system which were part of this Thesis.

Several studies on the A·T base pair showed that the electronic relaxation might follow a pathway that is different from the G·C base pair. An experimental investigation of relaxation dynamics by Schultz and coworkers revealed a relaxation pathway not present in the monomers, which was discussed to be a proton transfer.[195] Several theoretical works predicted the existence of an energetically accessible double proton transfer process on the basis of *ab initio* calculations.[193,194] In opposition to these results, Perun et al. predicted a *single* proton transfer with a similar mechanism as was predicted for the WC G·C base pair to be responsible for the ultrafast deactivation of the WC A·T base pair.[196] Recently, the applicability of the (2APy·2APy) dimer as a model system for the A·T base pair has been investigated on the basis of TD-DFT calculations and Monte Carlo kinetic simulations.[197] Although the topography of the PES seems to be different due to different geometric constraints in both systems, the observed Monte-Carlo kinetics were found to be similar. Regarding the discussed potential differences of A·T and G·C base pairs, however, this means that the results for the 2APy·2APy dimer should be taken with caution if they are used for the explanation of WC base pair relaxation mechanisms.

The above discussion covered the radiationless deactivation of base pairs after direct irradiation. Another process that potentially leads to DNA damages such as proton transfer reactions, i.e., structural changes of the single molecules or strands is the reaction with exogenously or endogenously generated radical species, e.g., via the ionization with UV photons. The electrons and/or holes generated in such processes can be transferred through the DNA. Owing to its low ionization potential,[198] guanine is a sink for delocalized holes in the DNA strand and forms radical cations. Cytosine and thymine, on the other hand, possess the highest ionization potential of the four DNA bases, and are consequently prone to form radical anions with delocalized electrons. The mechanisms, products and implications of these reactions have been a matter of intense research over the last decades. A review by Kumar and Sevilla gives an overview of the current state of knowledge regarding proton transfer reactions in DNA until 2010.[34]

1.3 Aims of this thesis

The main topics of this Thesis were the influence of structural modifications and hydrogen bonding on the ultrafast deactivation dynamics of 6-oxopurines. The results helped to shed light on the deactivation pathways of guanine, which is possibly the most prominent 6-oxopurine. In Figure 1.5, the structurally modified molecules which were investigated in this Thesis are shown. All of these molecules exhibit a different substitution at the C(2) position, which is expected to play a crucial role for the deactivation after electronic excitation of 6-oxopurines (cf. Sec. 1.2). Xanthine, shown in Figure 1.5(a), possesses a carbonyl group at the C(2) position and therefore no double bond at C(2)-N(3). The poor solubility of xanthine in polar solvents prevents the investigation in water, but the

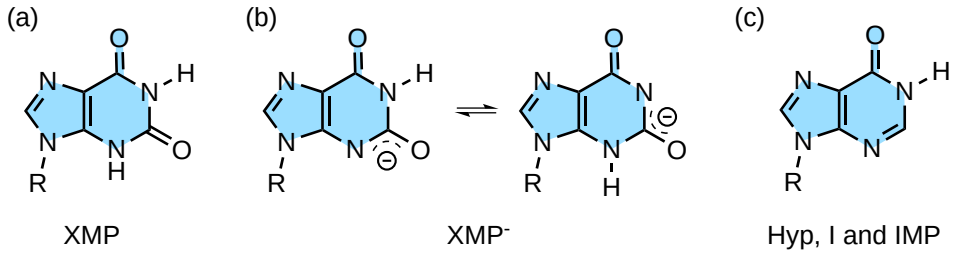

Figure 1.5: Structures of the 6-oxopurines that were investigated as part of this Thesis. R corresponds to H in case of hypoxanthine (Hyp) and xanthine, ribosyl in case of inosine (I) and ribosyl monophosphate in case of inosine monophosphate (IMP) and xanthosine monophosphate (XMP). The 6-oxopurine backbones are highlighted in blue.

respective nucleotide xanthosine monophosphate (XMP) is accessible for such experiments. XMP features unique acid-base properties among the purine bases: At pH$\geqslant$ 5.5, the xanthine moiety is deprotonated and the tautomeric equilibrium shown in Figure 1.5(b) is present.[199] The neutral and the anionic forms have been studied using time-resolved fluorescence and absorption spectroscopy. In contrast to the results for other purine bases, where the deactivation was found to take place through deformation of the six-membered ring, the deactivation is most likely mediated by an out-of-plane puckering mode of the five-membered ring as it was proposed theoretically.[200] The results, including a detailed discussion about possible reasons and implications, are given in Chapter 3.

The second investigated structurally modified 6-oxopurine is hypoxanthine (Hyp), which is closely related to the guanine structure, but lacks the exocyclic amino group (Fig. 1.5(c)). The results of time-resolved experiments on Hyp, its nucleoside inosine (I) and nucleotide inosine monophosphate (IMP) in water are presented in Chapter 4 and show a drastic acceleration and simplification of excited-state depopulation pathways compared to guanine, where quite complex deactivation dynamics were observed.[74,78,81]

The results obtained for the deactivation of Hyp were used as a basis for the second main topic of this Thesis, the influence of hydrogen bonds on the deactivation after electronic excitation. The hydrogen-bonded inosine dimer, shown in Figure 1.6, turned out to exhibit no significant changes of the deactivation dynamics compared to the monomer apart from a slight increase of excited-state lifetimes. These are possibly due to some steric restraints induced by the hydrogen bonds, which are located at the six-membered ring. These rather straightforward results, presented in Chapter 5, qualifies the inosine dimer as an excellent test case for more complicated systems such as the larger hydrogen-bonded assemblies of guanine and the G·C base pair. The results of the former show pronounced differences to the deactivation dynamics of the monomer. A detailed discussion can be found in Chapter 6. The Watson-Crick G·C base pair has been the subject of a number of theoretical and experimental investigations over the last decade (cf. Sec.1.2). In Chapter 7, experimental evidence for the pres-

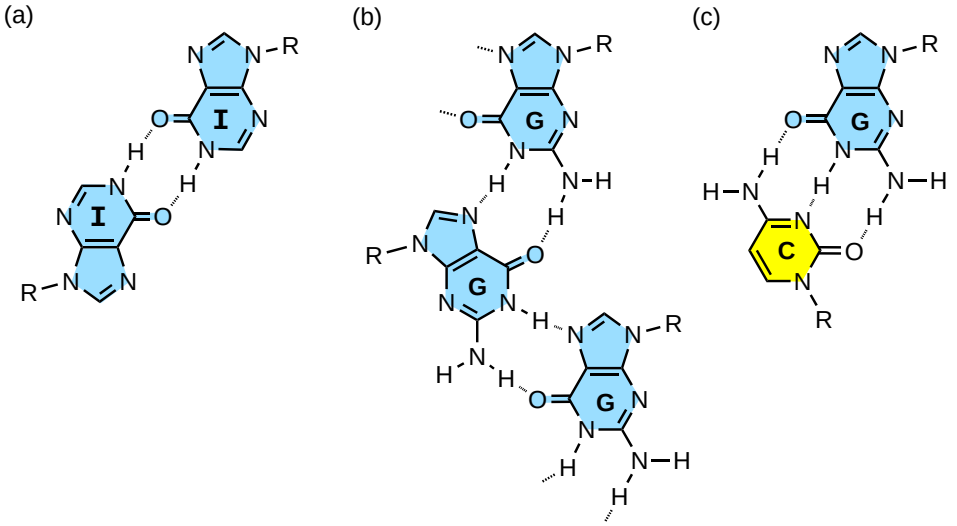

Figure 1.6: Structures of the hydrogen-bonded assemblies that were investigated in the course of this Thesis: (a) Inosine dimer in $CHCl_3$, (b) example of guanine assembly in *n*-hexane, (b) G·C Watson-Crick base pair in $CHCl_3$. R corresponds to 2′,3′,5′-O-TBDMS protected ribosyl residues. The 6-oxopurine backbones are highlighted in blue, the pyrimidine backbone in yellow.

ence of the electron-driven process will be given that might answer the long-lasting question of whether or nor this pathway is relevant for the deactivation inside DNA. All hydrogen-bonded model systems were accessible for spectroscopy using solutions of the respective 2′,3′,5′-O-TBDMS protected nucleosides in $CHCl_3$ and n-hexane.

Before the presentation of the experimental results on the above topics, Chapter 2 will present the experimental techniques with a strong focus on new developments. At the end of this Thesis, Chapter 8 will give a summary and outlook.

BIBLIOGRAPHY

[1] International Human Genome Sequencing Consortium, *Nature* **2001**, *409*, 860–921.

[2] Venter, J. C. et al. *Science* **2001**, *291*, 1304–1351.

[3] International Human Genome Sequencing Consortium, *Nature* **2004**, *431*, 931–945.

[4] The ENCODE Project Consortium, *Nature* **2007**, *447*, 799–816.

[5] Dunham, I. et al. *Nature* **2012**, *489*, 57–74.

[6] Nelson, D.; Cox, M. *Biochemie*; Springer, 2011.

[7] Berg, J. M.; Tymoczko, J. L.; Stryer, L. *Biochemistry*; Freeman: New York, 2010.

[8] Brown, T. A. *Genomes 3*, 3rd ed.; Garland Science: New York, 2007.

[9] Saenger, W. *Principles of Nucleic Acid Structure*; Springer: New York, 1983.

[10] Bloomfield, V. A.; Crothers, D. M.; Jr., I. T. *Nucleic Acids*; University Science Books: Sausalito, California, 1999.

[11] Brown, T.; Kennard, O.; Kneale, G.; Rabinovich, D. *Nature* **1985**, *315*, 604–606.

[12] Kneale, G.; Brown, T.; Kennard, O.; Rabinovich, D. *J. Mol. Biol.* **1985**, *186*, 805–814.

[13] Ho, P. S.; Frederick, C. A.; Quigley, G. J.; Van der Marel, G. A.; Van Boom, J. H.; Wang, A. H. J.; Rich, A. *EMBO J.* **1985**, *4*, 3617–3623.

[14] Brown, T.; Hunter, W. N.; Kneale, G.; Kennard, O. *Proc. Natl. Acad. Sci. U. S. A.* **1986**, *83*, 2402–2406.

[15] Hunter, W.; Brown, T.; Anand, N. N.; Kennard, O. *Nature* **1986**, *320*, 552–555.

[16] Blackburn, G. M., Gait, M. J., Eds. *Nucleic Acids in Chemistry and Biology*; IRL Press at Oxford University Press, 1990.

[17] Shakked, Z.; Rabinovich, D. *Prog. Biophys. Mol. Biol.* **1986**, *47*, 159–195.

[18] Wulff, D. L.; Fraenkel, G. *Biochim. Biophys. Acta* **1961**, *51*, 332–339.

[19] Johns, H. E.; Pearson, M. L.; LeBlanc, J. C.; Helleiner, C. W. *J. Mol. Biol.* **1964**, *9*, 503–524.

[20] Varghese, A. J.; Wang, S. Y. *Science* **1967**, *156*, 955–957.

[21] Varghese, A. J.; Wang, S. Y. *Science* **1968**, *160*, 186–187.

[22] Serrano-Perez, J. J.; González-Ramírez, I.; Coto, P. B.; Merchán, M.; Serrano-Andrés, L. *J. Phys. Chem. B* **2008**, *112*, 14096–14098.

[23] Marguet, S.; Markovitsi, D. *J. Am. Chem. Soc.* **2005**, *127*, 5780–5781.

[24] Boggio-Pasqua, M.; Groenhof, G.; Schaefer, L. V.; Grubmueller, H.; Robb, M. A. *J. Am. Chem. Soc.* **2007**, *129*, 10996–10997.

[25] Schreier, W. J.; Schrader, T. E.; Koller, F. O.; Gilch, P.; Crespo-Hernandez, C. E.; Swaminathan, V. N.; Carell, T.; Zinth, W.; Kohler, B. *Science* **2007**, *315*, 625–629.

[26] Schreier, W. J.; Kubon, J.; Regner, N.; Haiser, K.; Schrader, T. E.; Zinth, W.; Clivio, P.; Gilch, P. *J. Am. Chem. Soc.* **2009**, *131*, 5038–5039.

[27] Climent, T.; González-Ramírez, I.; González-Luque, R.; Merchán, M.; Serrano-Andrés, L. *J. Phys. Chem. Lett.* **2010**, *1*, 2072–2076.

[28] Roca-Sanjuan, D.; Olaso-González, G.; González-Ramírez, I.; Serrano-Andrés, L.; Merchán, M. *J. Am. Chem. Soc.* **2008**, *130*, 10768–10779.

[29] Mitchell, D. L. *Photochem. Photobiol.* **1988**, *48*, 51–57.

[30] Sheu, C.; Foote, C. S. *J. Am. Chem. Soc.* **1995**, *117*, 6439–6442.

[31] Cadet, J.; Douki, T.; Ravanat, J.-L. *Acc. Chem. Res.* **2008**, *41*, 1075–1083.

[32] Sanche, L. *Nature* **2009**, *461*, 358–359.

[33] Kanvah, S.; Joseph, J.; Schuster, G. B.; Barnett, R. N.; Cleveland, C. L.; Landman, U. *Accts. Chem. Res.* **2010**, *43*, 280–287.

[34] Kumar, A.; Sevilla, M. D. *Chem. Rev.* **2010**, *110*, 7002–7023.

[35] Douki, T.; Angelov, D.; Cadet, J. *J. Am. Chem. Soc.* **2001**, *123*, 11360–11366.

[36] Daniels, M.; Hauswirth, W. *Science* **1971**, *171*, 675–677.

[37] Dantus, M.; Rosker, M. J.; Zewail, A. H. *J. Chem. Phys.* **1987**, *87*, 2395–2397.

[38] Gruebele, M.; Zewail, A. H. *Phys. Today* **1990**, *43*, 24–33.

[39] Zewail, A. H. *Prix Nobel* **2000**, 110–203.

[40] Klán, P.; Wirz, J. *Photochemistry of Organic Compounds - From Concepts to Practice*; Postgraduate Chemistry Series; Wiley, 2009.

[41] Turro, N. J.; Ramamurthy, V.; Scaiano, J. C. *Principles of Molecular Photochemistry - An Introduction*; University Science Books, 2009.

[42] Domcke, W., Yarkony, D. R., Köppel, H., Eds. *Conical Intersections - Electronic Structure, Dynamics and Spectroscopy*; Advanced Series in Physical Chemistry; World Scientific, 2004; Vol. 15.

[43] Domcke, W., Yarkony, D. R., Köppel, H., Eds. *Conical Intersections - Theory, Computation and Experiment*; Advanced Series in Physical Chemistry; World Scientific, 2011; Vol. 17.

[44] Crespo-Hernández, C. E.; Cohen, B.; Hare, P. M.; Kohler, B. *Chem. Rev.* **2004**, *104*, 1977–2019.

[45] Middleton, C. T.; de La Harpe, K.; Su, C.; Law, Y. K.; Crespo-Hernández, C. E.; Kohler, B. *Annu. Rev. Phys. Chem.* **2009**, *60*, 217–239.

[46] Schwalb, N. K.; Siewertsen, R.; Renth, F.; Temps, F. *Conical Intersections. Theory, Computation and Experiment. Advanced Series in Physical Chemistry* **2011**, *17*, 669 – 714.

[47] Serrano-Andrés, L.; Merchán, M. *J. Photochem. Photobiol. C* **2009**, *10*, 21–32.

[48] Voet, D.; Gratzer, W. B.; Cox, R. A.; Doty, P. *Biopolymers* **1963**, *1*, 193–208.

[49] Gut, I. G.; Wood, P. D.; Redmond, R. W. *J. Am. Chem. Soc.* **1996**, *118*, 2366–2373.

[50] Wood, P. D.; Redmond, R. W. *J. Am. Chem. Soc.* **1996**, *118*, 4256–4263.

[51] Abouaf, R.; Pommier, J.; Dunet, H.; Quan, P.; Nam, P.-C.; Nguyen, M. T. *J. Chem. Phys.* **2004**, *121*, 11668–11674.

[52] Merchán, M.; Serrano-Andrés, L.; Robb, M. A.; Blancafort, L. *J. Am. Chem. Soc.* **2005**, *127*, 1820–1825.

[53] Richter, M.; Marquetand, P.; Gonzalez-Vazquez, J.; Sola, I.; Gonzalez, L. *J. Phys. Chem. Lett.* **2012**, *3*, 3090–3095.

[54] Platt, J. R. *J. Chem. Phys.* **1949**, *17*, 484–495.

[55] Nir, E.; Kleinermanns, K.; Grace, L.; de Vries, M. S. *J. Phys. Chem. A* **2001**, *105*, 5106–5110.

[56] Nir, E.; Janzen, C.; Imhof, P.; Kleinermanns, K.; de Vries, M. S. *J. Chem. Phys.* **2001**, *115*, 4604–4611.

[57] Mons, M.; Dimicoli, I.; Piuzzi, F.; Tardivel, B.; Elhanine, M. *J. Phys. Chem. A* **2002**, *106*, 5088–5094.

[58] Nir, E.; Plützer, C.; Kleinermanns, K.; de Vries, M. *Eur. Phys. J. D* **2002**, *20*, 317–329.

[59] Nir, E.; Hünig, I.; Kleinermanns, K.; de Vries, M. S. *ChemPhysChem* **2004**, *5*, 131–137.

[60] Mons, M.; Piuzzi, F.; Dimicioli, I.; Gorb, L.; Leszczynski, J. *J. Phys. Chem. A* **2006**, *110*, 10921–10924.

[61] Seefeld, K.; Brause, R.; Häber, T.; Kleinermanns, K. *J. Phys. Chem. A* **2007**, *111*, 6217–6221.

[62] Pfeiderer, W. *Justus Liebigs Ann. Chem.* **1961**, *647*, 167–173.

[63] Dreyfus, M.; Dodin, G.; Bensaude, O.; Dubois, J. E. *J. Am. Chem. Soc.* **1975**, *97*, 2369–2376.

[64] Fülscher, M. P.; Serrano-Andrés, L.; Roos, B. O. *J. Am. Chem. Soc.* **1997**, *119*, 6168–6176.

[65] Langer, H.; Doltsinis, N. L. *Phys. Chem. Chem. Phys.* **2003**, *5*, 4516–4518.

[66] Langer, H.; Doltsinis, N. L. *Phys. Chem. Chem. Phys.* **2004**, *6*, 2742–2748.

[67] Chen, H.; Lu, S. *J. Chem. Phys.* **2006**, *124*, 154315.

[68] Marian, C. M. *J. Phys. Chem. A* **2007**, *111*, 1545–1553.

[69] Serrano-Andrés, L.; Merchán, M.; Borin, A. C. *J. Am. Chem. Soc.* **2008**, *130*, 2473–2484.

[70] Yamazaki, S.; Domcke, W. *J. Phys. Chem. A* **2008**, *112*, 7090–7098.

[71] Yamazaki, S.; Domcke, W.; Sobolewski, A. L. *J. Phys. Chem. A* **2008**, *112*, 11965–11968.

[72] Barbatti, M.; Szymczak, J. J.; Aquino, A. J. A.; Nachtigallová, D.; Lischka, H. *J. Chem. Phys.* **2011**, *134*, 014304.

[73] Doltsinis, N. L.; Markwick, P. R. L.; Nieber, H.; Langer, H. In *Radiation Induced Molecular Phenomena in Nucleic Acids*; Shukla, M. K., Leszczynski, J., Eds.; Springer, 2008; pp 265–299.

[74] Karunakaran, V.; Kleinermanns, K.; Improta, R.; Kovalenko, S. A. *J. Am. Chem. Soc.* **2009**, *131*, 5839–5850.

[75] Lan, Z.; Fabiano, E.; Thiel, W. *Chem. Phys. Chem.* **2009**, *10*, 1225–1229.

[76] Zelený, T.; Ruckenbauer, M.; Aquino, A. J.; Müller, T.; Lankaš, F.; Dršata, T.; Hase, W. L.; Nachtigallova, D.; Lischka, H. *J. Am. Chem. Soc.* **2012**, *134*, 13662–13669.

[77] Heggen, B.; Lan, Z.; Thiel, W. *Phys. Chem. Chem. Phys. 14*, 8137–8146.

[78] Cheng, C. C.-W.; Ma, C.; Chan, C. T.-L.; Ho, K. Y.-F.; Kwok, W.-M. *Photochem. Photobiol. Sci.* **2013**, DOI: 10.1039/C3PP25450J.

[79] Canuel, C.; Mons, M.; Piuzzi, F.; Tardivel, B.; Dimicoli, I.; Elhanine, M. *J. Chem. Phys.* **2005**, *122*, 074316.

[80] Kang, H.; Lee, K. T.; Jung, B.; Ko, Y. J.; Kim, S. K. *J. Am. Chem. Soc.* **2002**, *124*, 12958–12959, PMID: 12405817.

[81] Miannay, F.-A.; Gustavsson, T.; Banyasz, A.; Markovitsi, D. *J. Phys. Chem. A* **2010**, *114*, 3256–3263.

[82] Pecourt, J.-M. L.; Peon, J.; Kohler, B. *J. Am. Chem. Soc.* **2000**, *122*, 9348–9349.

[83] Pecourt, J.-M. L.; Peon, J.; Kohler, B. *J. Am. Chem. Soc.* **2001**, *123*, 10370–10378.

[84] Peon, J.; Zewail, A. H. *Chem. Phys. Lett.* **2001**, *348*, 255–262.

[85] Sobolewski, A. L.; Domcke, W. *Eur. Phys. J. D* **2002**, *20*, 369–374.

[86] Marian, C. M. *J. Chem. Phys.* **2005**, *122*, 104314.

[87] Perun, S.; Sobolewski, A. L.; Domcke, W. *Chem. Phys.* **2005**, *313*, 107–112.

[88] Perun, S.; Sobolewski, A. L.; Domcke, W. *J. Am. Chem. Soc.* **2005**, *127*, 6257–6265.

[89] Chen, H.; Li, S. *J. Phys. Chem. A* **2005**, *109*, 84438446.

[90] Serrano-Andrés, L.; Merchán, M.; Borin, A. C. *Chem. Eur. J.* **2006**, *12*, 6559–6571.

[91] Serrano-Andrés, L.; Merchán, M.; Borin, A. C. *Proc. Natl. Acad. Sci. U.S.A.* **2006**, *103*, 8691–8691.

[92] Canuel, C.; Elhanine, M.; Mons, M.; Piuzzi, F.; Tardivel, B.; Dimicoli, I. *Phys. Chem. Chem. Phys.* **2006**, *8*, 3978–3987.

[93] Barbatti, M.; Lischka, H. *J. Am. Chem. Soc.* **2008**, *130*, 6831–6839.

[94] Conti, I.; Garavelli, M.; Orlandi, G. *J. Am. Chem. Soc.* **2009**, *131*, 16108–16118.

[95] Ludwig, V.; da Costa, Z. M.; do Amaral, M. S.; Borin, A. C.; Canuto, S.; Serrano-Andrés, L. *Chem. Phys. Lett.* **2010**, *492*, 164–169.

[96] Lan, Z.; Lu, Y.; Fabiano, E.; Thiel, W. *ChemPhysChem* **2011**, *12*, 1989–1998.

[97] González-Vazquez, J.; González, L. *ChemPhysChem* **2010**, *11*, 3617–3624.

[98] Fuelscher, M. P.; Roos, B. O. *J. Am. Chem. Soc.* **1995**, *117*, 2089–2095.

[99] Ismail, N.; Blancafort, L.; Olivucci, M.; Kohler, B.; Robb, M. A. *J. Am. Chem. Soc.* **2002**, *124*, 6818–6819.

[100] Merchán, M.; Serrano-Andrés, L. *J. Am. Chem. Soc.* **2003**, *125*, 8108–8109.

[101] Blancafort, L.; Robb, M. A. *J. Phys. Chem. A* **2004**, *108*, 10609–10614.

[102] Tomic, K.; Tatchen, J.; Marian, C. M. *J. Phys. Chem. A* **2005**, *109*, 8410–8418.

[103] Zgierski, M. Z.; Patchkovskii, S.; Lim, E. C. *J. Chem. Phys. 123*, 081101.

[104] Zgierski, M. Z.; Patchkovskii, S.; Fujiwara, T.; Lim, E. C. *J. Phys. Chem. A* **2005**, *109*, 9384–9387.

[105] Merchán, M.; González-Luque, R.; Climent, T.; Serrano-Andrés, L.; Rodriguez, E.; Reguero, M.; Pelaez, D. *J. Phys. Chem. B* **2006**, *110*, 26471–26476.

[106] Blancafort, L. *Photochem. Photobiol.* **2007**, *83*, 603–610.

[107] Kistler, K. A.; Matsika, S. *J. Phys. Chem. A* **2007**, *111*, 2650–2661.

[108] Kistler, K. A.; Matsika, S. *J. Chem. Phys.* **2008**, *128*, 215102.

[109] Hudock, H. R.; Martínez, T. J. *ChemPhysChem* **2008**, *9*, 2486–2490.

[110] Zgierski, M. Z.; Alavi, S. *Chem. Phys. Lett.* **2006**, *426*, 398–404.

[111] Blancafort, L.; Migani, A. *J. Photochem. Photobiol., A* **2007**, *190*, 283–289.

[112] Shterev, I. G.; Delchev, V. B. *Monatsh. Chem.* **2012**, *143*, 763–770.

[113] Kistler, K. A.; Matsika, S. *J. Phys. Chem. A* **2009**, *113*, 12396–12403.

[114] Kistler, K.; Spiridoula, M. *Phys. Chem. Chem. Phys. 12*, 5024–5031.

[115] Valiev, M.; Kowalski, K. *J. Chem. Phys.* **2006**, *125*, 211101.

[116] Lan, Z.; Fabiano, E.; Thiel, W. *J. Phys. Chem. B* **2009**, *113*, 3548–3555.

[117] Onidas, D.; Markovitsi, D.; Marguet, S.; Sharonov, A.; Gustavsson, T. *J. Phys. Chem. B* **2002**, *106*, 11367–11374.

[118] Nir, E.; Müller, M.; Grace, L. I.; de Vries, M. S. *Chem. Phys. Lett.* **2002**, *355*, 59–64.

[119] Sharonov, A.; Gustavsson, T.; Carre, V.; Renault, E.; Markovitsi, D. *Chem. Phys. Lett.* **2003**, *380*, 173–180.

[120] Nir, E.; Huenig, I.; Kleinermanns, K.; De Vries, M. S. *Phys. Chem. Chem. Phys.* **2003**, *5*, 4780–4785.

[121] Malone, R. J.; Miller, A. M.; Kohler, B. *Photochem. Photobiol.* **2003**, *77*, 158–164.

[122] Blancafort, L.; Cohen, B.; Hare, P. M.; Kohler, B.; Robb, M. A. *J. Phys. Chem. A* **2005**, *109*, 4431–4436.

[123] Hare, P. M.; Crespo-Hernandez, C. E.; Kohler, B. *Proc. Natl. Acad. Sci. U. S. A.* **2007**, *104*, 435–440.

[124] Kotur, M.; Weinacht, T. C.; Zhou, C.; Kistler, K. A.; Matsika, S. *J. Chem. Phys.* **2011**, *134*, 184309.

[125] Matsika, S. *J. Phys. Chem. A* **2004**, *108*, 7584–7590.

[126] Matsika, S. *J. Phys. Chem. A* **2005**, *109*, 7538–7545.

[127] Perun, S.; Sobolewski, A. L.; Domcke, W. *J. Phys. Chem. A* **2006**, *110*, 13238–13244.

[128] Hare, P. M.; Crespo-Hernandez, C. E.; Kohler, B. *J. Phys. Chem. B* **2006**, *110*, 18641–18650.

[129] Zechmann, G.; Barbatti, M. *J. Phys. Chem. A* **2008**, *112*, 8273–8279.

[130] Gustavsson, T.; Banyasz, A.; Lazzarotto, E.; Markovitsi, D.; Scalmani, G.; Frisch, M. J.; Barone, V.; Improta, R. *J. Am. Chem. Soc.* **2006**, *128*, 607–619.

[131] Hudock, H. R.; Levine, B. G.; Thompson, A. L.; Satzger, H.; Townsend, D.; Gador, N.; Ullrich, S.; Stolow, A.; Martínez, T. J. *J. Phys. Chem. A* **2007**, *111*, 8500–8508.

[132] Asturiol, D.; Lasorne, B.; Robb, M. A.; Blancafort, L. *J. Phys. Chem. A* **2009**, *113*, 10211–10218.

[133] Ward, D. C.; Reich, E.; Stryer, L. *J. Biol. Chem.* **1969**, *244*, 1228–1228.

[134] Holmén, A.; Broo, A.; Albinsson, B.; Nordén, B. *J. Am. Chem. Soc.* **1997**, *119*, 12240–12240.

[135] Neely, R. K.; Magennis, S. W.; Dryden, D. T. F.; Jones, A. C. *J. Phys. Chem. B* **2004**, *108*, 17606–17606.

[136] Seefeld, K. A.; Plützer, C.; Löwenich, D.; Häber, T.; Linder, R.; Kleinermanns, K.; Tatchen, J.; Marian, C. M. *Phys. Chem. Chem. Phys.* **2005**, *7*, 3021–3021.

[137] Perun, S.; Sobolewski, A. L.; Domcke, W. *Mol. Phys.* **2006**, *104*, 1113–1121.

[138] Ludwig, V.; do Amaral, M. S.; da Costa, Z. M.; Borin, A. C.; Canuto, S.; Serrano-Andrés, L. *Chem. Phys. Lett.* **2008**, *463*, 201–205.

[139] Feng, K.; Engler, G.; Seefeld, K.; Kleinermanns, K. *ChemPhysChem* **2009**, *10*, 886–889.

[140] Lobsiger, S.; Sinha, R. K.; Trachsel, M.; Leutwyler, S. *J. Chem. Phys.* **2011**, *134*, 114307–114307.

[141] Broo, A.; Holmen, A. *Chem. Phys.* **1996**, *211*, 147–147.

[142] Larsen, O. F.; van Stokkum, I. H.; Groot, M.-L.; Kennis, J. T.; van Grondelle, R.; van Amerongen, H. *Chem. Phys. Lett.* **2003**, *371*, 157–163.

[143] Rachofsky, E. L.; Osman, R.; Ross, J. B. A. *Biochemistry* **2001**, *40*, 946–956.

[144] Schwalb, N. K.; Temps, F. *Phys. Chem. Chem. Phys.* **2006**, *8*, 5229–5235.

[145] Schwalb, N. K.; Temps, F. *J. Phys. Chem. A* **2009**, *113*, 13113–13123.

[146] Stuhldreier, M. Femtosekunden-zeitaufgelöste transiente Absorptionsspektroskopie an Adenin und N^6,N^6-Dimethyladenin. Diploma Thesis, Christian-Albrechts-Universität zu Kiel, 2008.

[147] Demeter, A.; Druzhinin, S. I.; Kovalenko, S. A.; Senyushkina, T. A.; Zachariasse, K. A. *J. Phys. Chem. A* **2011**, *115*, 1521–1537.

[148] Albinsson, B. *J. Am. Chem. Soc.* **1997**, *119*, 6369–6375.

[149] Andreásson, J.; Holmén, A.; Albinsson, B. *J. Phys. Chem. B* **1999**, *103*, 9782–9789.

[150] Parusel, A. B. J.; Rettig, W.; Rotkiewicz, K. *J. Phys. Chem. A* **2002**, *106*, 2293–2299.

[151] Chargaff, E. *Experientia* **1950**, *6*, 201–209.

[152] Watson, J. D.; Crick, F. H. C. *Nature* **1953**, *171*, 737–738.

[153] Brandes, R.; Rupprecht, A.; Kearns, D. *Biophys. J.* **1989**, *56*, 683–691.

[154] Szyc, L.; Dwyer, J. R.; Nibbering, E. T. J.; Elsaesser, T. *Chem. Phys.* **2009**, *357*, 36–44.

[155] Szyc, L.; Yang, M.; Elsaesser, T. *J. Phys. Chem. B* **2010**, *114*, 7951–7957.

[156] Kielkopf, C. L.; White, S.; Szewczyk, J. W.; Turner, J. M.; Baird, E. E.; Dervan, P. B.; Rees, D. C. *Science* **1998**, *282*, 111–115.

[157] Stormo, G. D.; Fields, D. S. *Trends Biochem. Sci.* **1998**, *23*, 109–113.

[158] Gellert, M.; Lipsett, M. N.; Davies, D. R. *Proc. Nat. Acad. Sci. USA* **1962**, *48*, 2013–2018.

[159] Guschlbauer, W.; Chantot, J.-F.; Thiele, D. *J. Biomol. Struct. Dyn.* **1990**, *8*, 491–511.

[160] Davis, J. T. *Angew. Chem. Int. Ed.* **2004**, *43*, 668–698.

[161] Shukla, M. K.; Leszczynski, J. *J. Mol. Struct.: THEOCHEM* **2000**, *529*, 99–112.

[162] Shukla, M. K.; Leszczynski, J. *J. Phys. Chem. B* **2005**, *109*, 17333–17339.

[163] Kagawa, T.; Sato, F.; Aikawa, K.; Kiyohara, T.; Kato, Y.; Iida, T. *Chem. Phys. Lett.* **2006**, *424*, 364–368.

[164] Liu, D.; Wyttenbach, T.; Bowers, M. T. *J. Am. Chem. Soc.* **2006**, *128*, 15155–15163.

[165] Belau, L.; Wilson, K. R.; Leone, S. R.; Ahmed, M. *J. Phys. Chem. A* **2007**, *111*, 7562–7568.

[166] Hunter, K. C.; Wetmore, S. D. *Chem. Phys. Lett.* **2006**, *422*, 500–506.

[167] Miyamoto, K.-I.; Onodera, K.; Yamaguchi, R.-T.; Ishibashi, K.-I.; Kimura, Y.; Niwano, M. *Chem. Phys. Lett.* **2007**, *436*, 233–238.

[168] Saigusa, H.; hei Urashima, S.; Asami, H. *J. Phys. Chem. A* **2009**, *113*, 3455–3462.

[169] Etinski, M.; Marian, C. M. *Phys. Chem. Chem. Phys.* **2010**, *12*, 4915–4923.

[170] Shukla, M. K.; Leszczynski, J. *Chem. Phys. Lett.* **2009**, *478*, 254–259.

[171] Nam, S. H.; Park, H. S.; Song, J. K.; Park, S. M. *J. Phys. Chem. A* **2007**, *111*, 3480–3484.

[172] Ingham, K.; El-Bayoumi, M. A. *J. Am. Chem. Soc.* **1974**, *96*, 1674–1682.

[173] Fuke, K.; Kaya, K. *J. Phys. Chem.* **1989**, *93*, 614–621.

[174] Chachisvilis, M.; Fiebig, T.; Douhal, A.; Zewail, A. H. *J. Phys. Chem. A* **1998**, *102*, 669–673.

[175] Takeuchi, S.; Tahara, T. *J. Phys. Chem. A* **1998**, *102*, 7740–7753.

[176] Douhal, A.; Kim, S. K.; Zewail, A. H. *Nature* **1995**, *378*, 260–263.

[177] Sekiya, H.; Sakota, K. *J. Photochem. Photobiol., C* **2008**, *9*, 81–91.

[178] Sobolewski, A. L.; Domcke, W. *Chem. Phys.* **2003**, *294*, 73–83.

[179] Sobolewski, A. L.; Domcke, W. *Phys. Chem. Chem. Phys.* **2004**, *6*, 2763–2771.

[180] Sobolewski, A. L.; Domcke, W.; Hattig, C. *Proc. Natl. Acad. Sci. U.S.A.* **2005**, *102*, 17903–17906.

[181] Yamazaki, S.; Taketsugu, T. *Phys. Chem. Chem. Phys.* **2012**, *14*, 8866–8877.

[182] Groenhof, G.; Schäfer, L.; Boggio-Pasqua, M.; Goette, M.; Grubmüller, H.; Robb, M. A. *J. Am. Chem. Soc.* **2007**, *129*, 6812–6819.

[183] Markwick, P. R. L.; Doltsinis, N. L. *J. Chem. Phys.* **2007**, *126*, 175102.

[184] Markwick, P. R. L.; Doltsinis, N. L.; Schlitter, J. *J. Chem. Phys.* **2007**, *126*, 045104.

[185] Alexandrova, A. N.; Tully, J. C.; Granucci, G. *J. Phys. Chem. B* **2010**, *114*, 12116–12128.

[186] Schultz, T.; Samoylova, E.; Radloff, W.; Hertel, I. V.; Sobolewski, A. L.; Domcke, W. *Science* **2004**, *306*, 1765–1768.

[187] Samoylova, E.; Smith, V. R.; Ritze, H.-H.; Radloff, W.; Kabelac, M.; Schulz, T. *J. Am. Chem. Soc.* **2006**, *128*, 15652–15652.

[188] Samoylova, E.; Radloff, W.; Ritze, H.-H.; Schultz, T. *J. Phys. Chem. A* **2009**, *113*, 8195–8201.

[189] Abo-Riziq, A.; Grace, L.; Nir, E.; Kabelac, M.; Hobza, P.; de Vries, M. S. *Proc. Natl. Acad. Sci. U.S.A.* **2005**, *102*, 20–23.

[190] Schwalb, N. K.; Temps, F. *J. Am. Chem. Soc.* **2007**, *129*, 9272–9273.

[191] Schwalb, N. K.; Michalak, T.; Temps, F. *J. Phys. Chem. B* **2009**, *113*, 16365–16376, PMID: 19947627.

[192] Biemann, L.; Kovalenko, S. A.; Kleinermanns, K.; Mahrwald, R.; Markert, M.; Improta, R. *J. Am. Chem. Soc.* **2011**, *133*, 19664–19667.

[193] Guallar, V.; Douhal, A.; Moreno, M.; Lluch, J. M. *J. Phys. Chem. A* **1999**, *103*, 6251–6256.

[194] Xiao, S.; Wang, L.; Liu, Y.; Lin, X.; Liang, H. *J. Chem. Phys.* **2012**, *137*, 195101.

[195] Samoylova, A.; Schultz, T.; Hertel, I. V.; Radloff, W. *Chem. Phys.* **2008**, *347*, 376–382.

[196] Perun, S.; Sobolewski, A.; Domcke, W. *J. Phys. Chem. A* **2006**, *110*, 9031–9038.

[197] Ai, Y.-J.; Zhang, F.; Cui, G.-L.; Luo, Y.; Fang, W.-H. *J. Chem. Phys.* **2010**, *133*, 064302–064302.

[198] Steenken, S.; Jovanovic, S. V. *J. Am. Chem. Soc.* **1997**, *119*, 617–618.

[199] Massoud, S. S.; Corfù, N. A.; Griesser, R.; Sigel, H. *Chem.-Eur. J.* **2004**, *10*, 5129–5137.

[200] Yamazaki, S.; Sobolewski, A. L.; Domcke, W. *Phys. Chem. Chem. Phys.* **2009**, *11*, 10165–10174.

2 EXPERIMENTAL METHODS

The research on the deactivation mechanisms of DNA building blocks in the condensed phase is characterized by two major challenges: First, almost all important routes from the electronically excited state back to the electronic ground state lead to a depopulation of the excited state on an ultrafast time scale. The direct, time resolved observation of phenomena such as the decay of fluorescence intensity and transient absorption therefore call for the use of femtosecond spectroscopy that will briefly be introduced in the following Section. Secondly, the low fluorescence quantum yields (cf. Section 1.2) and transient absorption signals of DNA building blocks makes the use of spectroscopic techniques with high sensitivities inevitable.

A major part of the work which lead to the present Thesis was the development of a highly sensitive and versatile transient absorption experiment. Much effort has been invested to ensure a straightforward, stable and reproducible operation of the setup that can be adjusted to the individual needs of different samples within a reasonable amount of time. A detailed description of setup and operation is given in Section 2.1.1, Section 2.1.2 deals with data processing and analysis.

The high sensitivity for the fluorescence decay detection is provided by a fluorescence up-conversion experiment that was described elsewhere[1,2] and has been extensively used for the investigation of DNA building blocks[3–11] and molecular switches[12] in our group. A short description of the setup is given in Section 2.2.

Time-resolved spectroscopy requires a careful investigation regarding structure, purity and integrity of all samples. Details on the materials and static spectroscopic techniques can be found in the experimental Sections of Chapters 3–7.

Some of the hydrogen-bonded nucleobases were also investigated by femtosecond time-resolved IR pump-probe and 2D IR spectroscopy in collaboration with the group of T. Elsaesser and E. Nibbering at the MBI Berlin.[13,14] The results, however, are not part of this Thesis.

2.1 FEMTOSECOND TIME-RESOLVED TRANSIENT ABSORPTION SPECTROSCOPY

Nonlinear optical processes form the basis for the generation and conversion of ultrashort pulses that are needed for femtosecond time-resolved spectroscopy. They play a role when an intense electromagnetic wave interacts with matter and induces a polarization that comprises not only polarization oscillating with the original frequency, but also with higher harmonic terms. This leads to a number of nonlinear effects that are de-

scribed in detail in a number of textbooks[15–18] and in former PhD theses of the work group.[1,19,20] Among those effects are second harmonic generation (SHG) and third harmonic generation (THG), sum frequency generation (SFG), and the generation of spectrally broad "white-light" pulses (supercontinuum generation, SCG). Processes like these provide a toolbox for the generation of ultrashort pulses in a broad wavelength range that are needed for femtosecond time-resolved experiments.

The direct detection of light on this short time scale is not feasible due to the long response time of the respective detectors. Therefore, the applied detection scheme for transient absorption spectroscopy and fluorescence up-conversion is based on the pump-probe principle. In the following, this principle will be discussed for transient absorption spectroscopy, since the major part of results of this Thesis were obtained with that technique. A schematic overview of the respective experiment is given in Figure 2.1.

The first step is the electronic excitation of sample molecules with an ultrashort pump pulse at a given time t_0. The molecular response is then monitored using ultrashort probe pulses that are temporally delayed with respect to the pump pulses by a delay time Δt, thus facilitating the detection at discrete times after excitation. The temporal delay is realized using a variable spatial delay line. The temporal resolution of the experiment is given by the convolution of the temporal widths of pump and probe pulse.

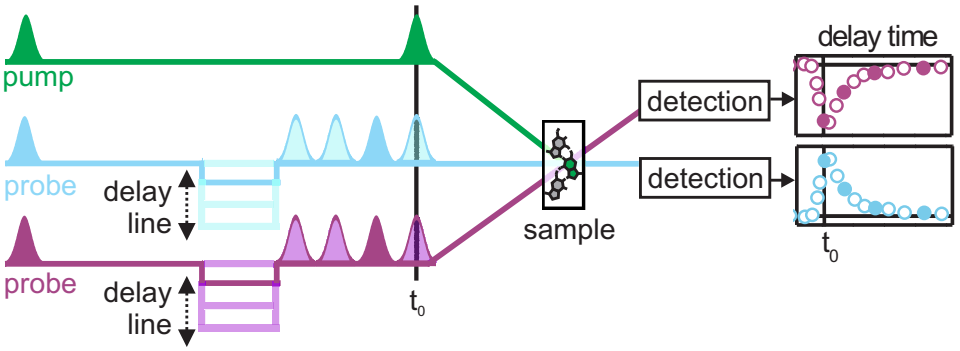

Figure 2.1: Schematic overview of the pump-probe transient absorption experiment. The ultrashort pump pulses excite the sample at a given time t_0 and the molecular response is monitored using ultrashort probe pulses at discrete delay times. The temporal delay between pump and probe pulses is realized by a variable spatial delay line. In the present transient absorption experiment, two probe pulses are available to allow for a simultaneous observation of transient absorption changes at $310 \leqslant \lambda_{probe} \leqslant 700$ nm (shown in blue) and a freely selectable single wavelength (shown in purple), usually employed for the monitoring of ground state recovery and vibrational cooling processes in the deep UV.

In the transient absorption experiment that was built here, two probe pulses are applied, one spectrally broad pulse with a fixed wavelength range of $310 < \lambda_{probe} < 700$ nm and a second, spectrally narrow pulse which can be set to any desired wavelength that is experimentally accessible. The observation of transient absorption in the broadband detection range provide information about individual lifetimes of certain electroni-

cally excited states. It is, however, always possible that molecules evolve to states not showing up in the observed wavelength range. For this reason, it is of great interest to obtain information about the overall excited-state lifetime by observing the repopulation of the ground state, i.e., the ground state recovery (GSR). This contribution appears as a negative transient absorption change since it is caused by the decreased population in the ground state after excitation. GSR can in principle be detected at any wavelength at which the molecule in its ground state absorbs, but to minimize overlap with absorption by vibrationally excited S_0 state molecules (hot ground state absorption, HGA) it is advantageous to look at a wavelength slightly blue to the excitation wavelength. In case of samples absorbing in the UV, the wavelength range of the spectrally broad probe pulse is not always sufficient to cover the respective spectral region. For this reason, the single-color detection was implemented, which allowed for the monitoring of transient absorption changes at probe wavelengths in the deep-UV.

Figure 2.2 shows a schematic overview of the most important molecular contributions to transient absorption signals. After excitation to an

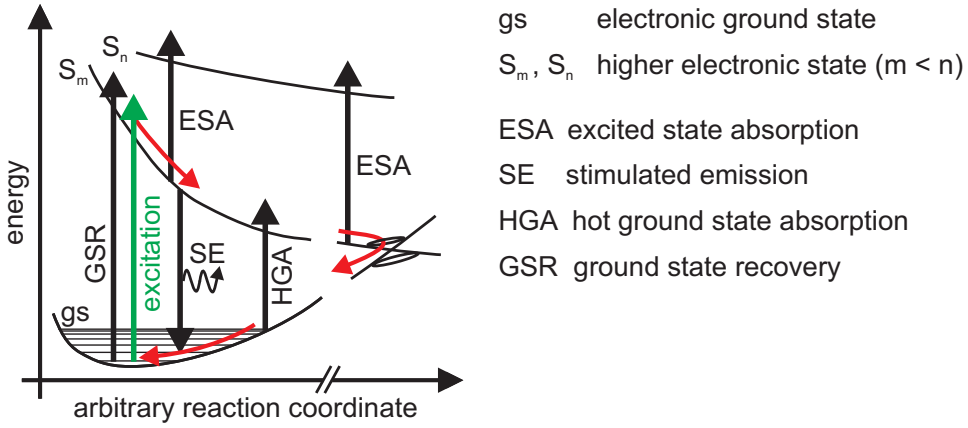

Figure 2.2: Schematic overview of contributions to the transient absorption signal.

electronically excited state, probe photons with a suitable energy can be absorbed and lead to an $S_m \rightarrow S_n$ transition, resulting in a positive signal called excited-state absorption (ESA). ESA can be observed for any $S_m \rightarrow S_n$ transition with sufficient oscillator strength, and S_m might be the initially populated state or a state populated during deactivation. This signal decays when the excited state is depopulated via radiative or non-radiative decay mechanisms, thus giving information about the lifetime of the respective state. When the probe pulses are spectrally resolved, wavelength shifts containing additional information can be observed for some molecules. The quantitative analysis of this information, however, is limited by the knowledge about S_n, since the magnitude of the respective shift depends on the gradients in both states. Another contribution to the observed transient absorption signal is stimulated emission (SE), which is induced by probe photons and usually red-shifted by several hundred cm^{-1} to the excitation wavelength. The observed SE signal is negative.

Once returned to the electronic ground state, the molecules are mostly highly vibrationally excited, thus giving rise to positive hot ground state absorption (HGA). This contribution is also red-shifted by up to some hundred cm^{-1} with respect to the $S_0 \rightarrow S_m$ absorption spectrum, and it usually features a blue-shift of the maximum with increasing delay times.

2.1.1 SETUP AND OPERATION OF THE TRANSIENT ABSORPTION EXPERIMENT

The transient absorption experiment built in the present work was driven by the output of a Ti:Sa laser (Clark-MXR CPA 2001) that was described elsewhere.[1] This laser delivers pulses with pulse lengths of 150 fs (FWHM) at 775 nm. Half of the overall output of 1000 µJ was used for the transient absorption experiment, the other half for the fluorescence up-conversion experiment (see Sec. 2.2) and laser diagnostics.

A sketch of the complete experimental setup as existing at present is given in Figure 2.3. The excitation and single-color probe pulses were each generated in a non-collinear optical parametric amplifier (NOPA) with subsequent temporal compression and frequency doubling. The NOPA process is a nonlinear optical process, during which a weak seed pulse is amplified by an intense pump pulse in a suitable nonlinear medium.[21,22] The broad-band probe pulses were generated using supercontinuum generation (SCG) in CaF_2. Each of the probe pulses were split into probe and reference pulses and the probe and pump pulses spatially and temporally overlayed in the sample cell. Detection was carried out using a prism spectrometer and CCD cameras for the broadband and photodiodes for the single-color pulses. The details of each part will be explained in the following, the focus being on the modified and new parts compared to the earlier setup described in the PhD Thesis of R. Siewertsen.[23] Especially the NOPA and whitelight optimization procedures have been described in some detail by Siewertsen and their description is consequently kept short in the following.

Generation of pump pulses

The NOPA delivering the pump pulses was pumped with ≈ 250 µJ of the laser fundamental. The seed pulses were generated by supercontinuum generation in a sapphire crystal ($d = 2$ mm, Korth Kristalle), yielding chirped whitelight pulses with a spectrum from 450 nm $\leqslant \lambda \leqslant$ 700 nm. The pump pulse was provided by the frequency-doubled laser fundamental ($\lambda = 387$ nm, $E \approx 60$ µJ). Both pulses were focused at an angle of $\approx 6°$ into a β-bariumborate (β-BaB_2O_4, BBO) crystal ($\theta = 32°$, $d = 2$ mm, CASTECH or EKSMA Optics) and spatially and temporally overlapped. The amplified wavelength range was chosen by delaying the pump pulses with respect to the chirped seed pulses. This allows for a selective amplification of a certain part of the spectrum. The generated signal pulses were compressed in a prism pair to obtain pulse lengths of $\approx 20-30$ fs (FWHM).

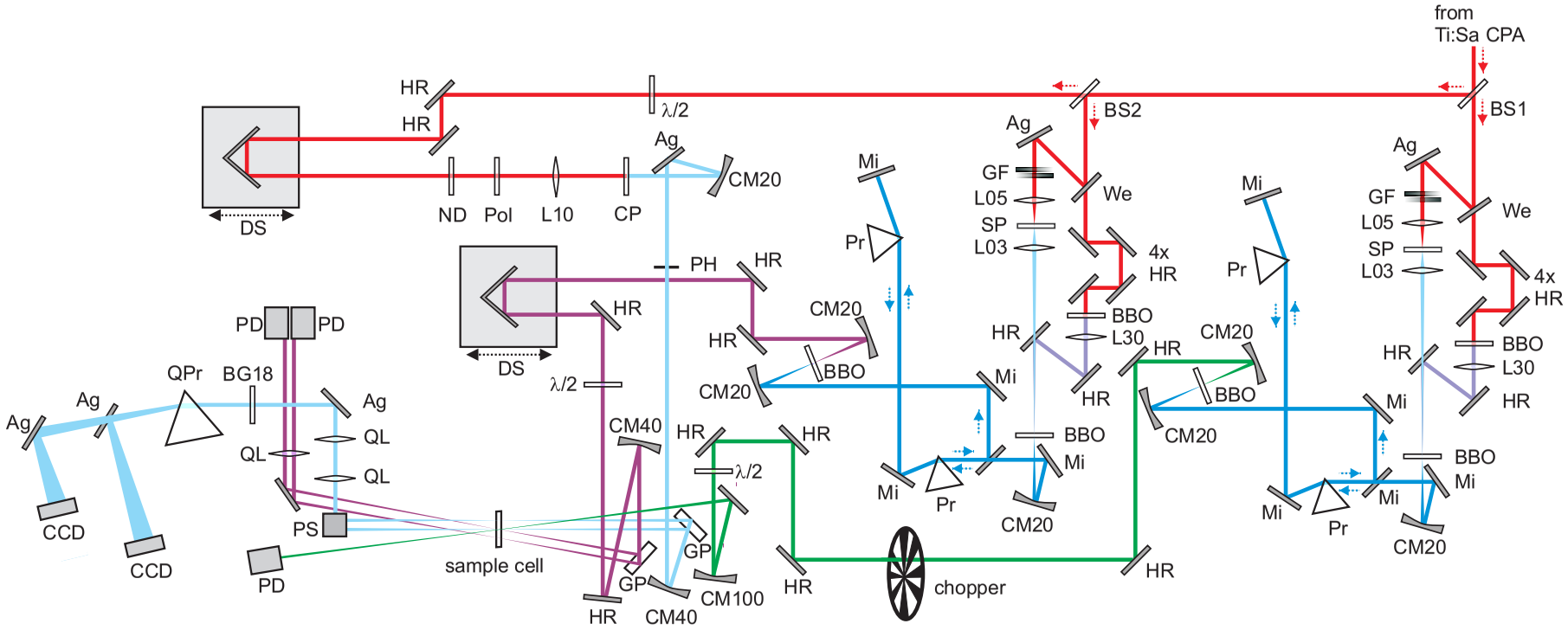

Ag	planar Ag mirror	CM20	concave mirror, rcc = 0.2m	GP	planar quartz glass plate	L30	lens, f = 0.3 m	Pr	BK7 prism
BBO	β-BaB_2O_4 crystal	CM40	concave mirror, rcc = 0.4 m	HR	high reflective mirror	Mi	planar Ag or Al mirror	PS	periscope
BG18	BG18 filter	CM100	concave mirror, rcc = 1 m	$\lambda/2$	half-wave plate	ND	neutral density filter	QL	quartz lens
BS1	beamsplitter, R=50%	CP	CaF_2 plate (d = 2 mm)	L03	lens, f = 30 mm	PD	photodiode	QPr	quartz prism
BS2	beamsplitter, R=70%	DS	delay stage with retroreflector	L05	lens, f = 50 mm	Pol	polarizer	SP	sapphire plate
CCD	FFT-CCD camera	GF	gradient filter	L10	lens, f = 0.1 m	PH	pinhole	We	wedge (30´)

Figure 2.3: Scheme of the transient absorption setup. For the sake of consistency with the actual setup on the optical table, the pulses propagate from the upper right to the lower left. The color scheme was chosen for clarity and does not reflect the experimental wavelengths.

A typical NOPA spectrum and autocorrelation function of the compressed pulse is shown in Figure 2.4. Typical output energies after the prism compressor were $3-10$ µJ. The pulses thus obtained were frequency-doubled

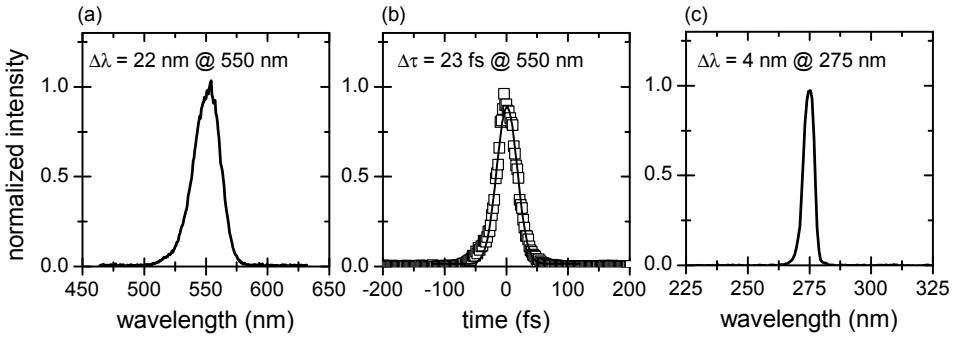

Figure 2.4: (a) Typical NOPA spectrum, (b) autocorrelation function of the compressed pulse, (c) spectrum of frequency-doubled pulse. The value of $\Delta\tau$ is the deconvoluted pulse length assuming a Gaussian shaped pulse.

in a BBO crystal ($d = 0.1$ mm, CASTECH or EKSMA Optics) with a suitable cut angle for the desired output wavelength. The cut angle for a given input wavelength can be calculated using the program SNLO.[24] A typical spectrum of the frequency-doubled pulses is shown in Figure 2.4(c). The bandwidth of 4 nm allows for a Fourier limited pulse length of 28 fs. Depending on the wavelength, pulse energies of $200-800$ nJ were obtained and reduced using a pinhole, if necessary (see below). The pump pulses were set to magic angle polarization with respect to the probe pulses using a $\lambda/2$ waveplate. An optical chopper (MC2000, Thorlabs) equipped with a 10 shot blade (MC1F10, Thorlabs) was used to cut out every second laser pulse, thus enabling the measurement of background signals without excitation.

Generation of broadband probe pulses

For the generation of the broadband probe pulses, ≈ 70 µJ of the laser fundamental was used. The laser pulses passed a delay stage (M-531.DG, Physik Instrumente) equipped with a retroreflector (CVI Melles Griot) and coarsely attenuated to $\leqslant 4$ µJ using an absorptive neutral density filter to avoid damage of the following optics. Fine tuning of the energy was done using a combination of a $\lambda/2$ waveplate and a polarizer (Edmund Optics).[25] The polarizer was set to let s-polarized waves pass. Tuning of the $\lambda/2$ waveplate, placed before the polarizer, provided a simple way of attenuating the pulses evenly over the beam profile, which resulted in a fast and reproducible optimization of the supercontinuum generation. For this, ≈ 2 µJ of the remaining laser fundamental were focused into a CaF_2 plate ($d = 2$ mm, Korth Kristalle or Layertech). This plate was moved vertically and horizontally so that consecutive laser pulses hit different spots on the plate, thus ensuring that the low damage threshold of CaF_2 was not exceeded. The stability and spectral characteristics had to be checked every

day and adjusted by varying energy and focus position in the CaF_2 plate (see Thesis of R. Siewertsen for details[23]).

Generation of single-color probe pulses

The optical pathway for the generation of single-color probe pulses was a replication of the one for pump pulse generation. The NOPA was driven with 180 µJ of the laser fundamental, yielding probe pulses with energies of $200 - 500$ µJ after frequency doubling. These pulses passed a delay stage (M-511.DG, Physik Instrumente) equipped with a retroreflector (CVI Melles Griot).

Optical pathways at the sample cell

All pulses were recollimated using reflective optics to reduce the chirp and obtain an optimal time resolution of the experiment.[23] For the same reason, all optical pathlengths were kept as short as possible. A detailed view of the following optical pathways around sample cell and detection units is given in Figure 2.5. The broadband and single-color probe pulses were split into probe and reference using the front and back reflection of a planar quartz glass plate ($d = 5$ mm, Laser Optik). All pulses were focused into the sample cell using focussing mirrors and the probe pulses (broadband and single color) were spatially overlapped with the pump pulse.

Setting up the optical pathway in front of the sample cell, shown in Figure 2.5, was guided by three considerations:

(i) The angles between the incident pulses were kept as small as possible, thus reducing the chirp of pump and probe pulses and consequently the intensity of coherent signals.[23,26] Since the spectrally broad pulses are especially prone to chirping, tilting of this pathway was avoided as much as possible.

(ii) The reproducible adjustment of the broadband probe pulses beam diameter was ensured using two focusing mirrors after the CaF_2 plate (cf. Fig. 2.3). The first mirror was aligned so that a slight prefocussing was achieved, and the second mirror focused the pulses into the sample cell. This resulted in smaller foci than focussing with only one focussing mirror after the CaF_2 plate as it was done before.[23] Generally, the probe foci were of the order of ≈ 100 µm and the pump pulse focus ≈ 300 µm (determined by knife-edge scans).

(iii) Overlapping of the two reference pulses was avoided by placing the two glass plates at an angle of $\approx 90°$ (see Fig. 2.6). This way, the respective front and back reflections arrive at the sample cell in the configuration shown in Figure 2.6. The flow direction in the sample cell was vertically, so that the excited volume was not pumped in the direction of any of the probe pulses.

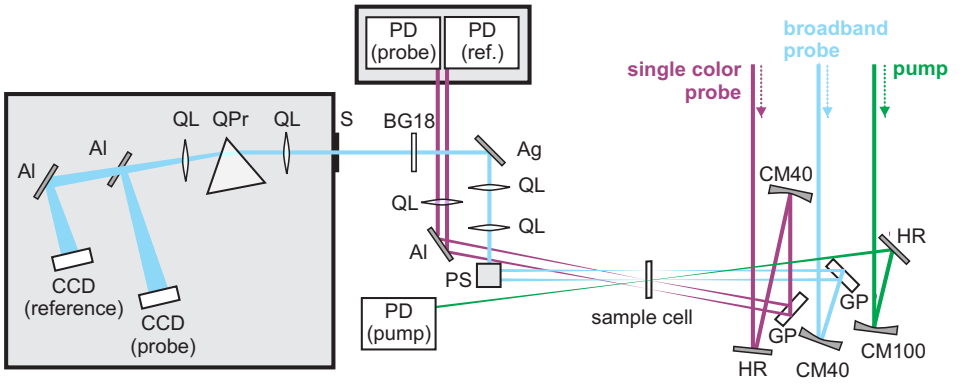

Ag	planar Ag mirror	CM100	concave mirror, rcc = 1 m	QL	quartz lens
Al	planar Al mirror	GP	quartz glass plate (d = 5mm)	QPr	quartz prism
BG18	BG18 filter	HR	high reflective mirror	S	slit
CCD	FFT-CCD cameras	PD	photodiode		black box
CM40	concave mirror, rcc = 0.4 m	PS	periscope		

Figure 2.5: Detailed scheme of the optical pathways at the sample cell and detection units.

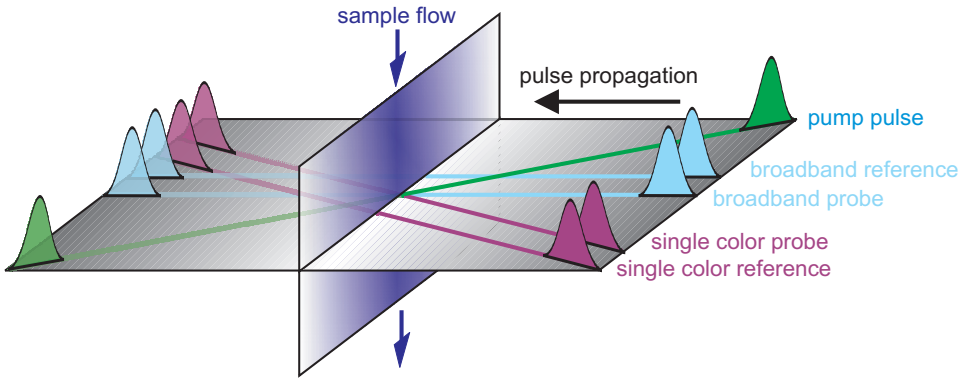

Figure 2.6: Sketch of the pulse propagation at the sample cell. The broadband probe pulses are traveling perpendicular to the sample cell and overlapped with the single-color probe and pump pulses. The two reference pulses are located on the right and left side of the pump and probe pulses. The sample flow is vertically, so that the excited volume is removed without crossing one of the reference pulses.

Sample cell and optimization procedure

The sample cell was, if not otherwise denoted, a flow cell with an optical thickness of d = 0.1 mm built in the institute workshop. It was equipped with two quartz windows (d = 0.2 mm, diameter 15 mm, Korth Kristalle) and a PTFE spacer. For aqueous solutions, the sample was pumped through the flow cell using a peristaltic pump (Reglo Analog MS-2/6, Ismatec) and Ismaprene tubes. For measurements with $CHCl_3$, a gear pump (Reglo-Z analog, Ismatec) equipped with an organic solvent resistant pumphead (Z-186 with PPS gears, Ismatech) and PTFE tubes was employed. Optimization of the pulse overlap was performed starting with the broadband signal by adjusting the pump pulses with the mirror directly in front of the flow cell (cf. Fig. 2.5). Subsequently, the single color signal was maximized by aligning the single color probe pulses. This procedure was done preferably using the molecular signal of the investigated sample. In case of low signals or sensitive molecules, where the exposure time to pump pulses had to be kept as low as possible, the optimization was performed using an identically constructed flow cell filled with a suitable laser dye. The correct position for the sample cell was then adjusted by positioning of the cell, which was placed on a manual translation stage, to the position where both single color and broadband signals were maximal. This is a much faster, but less accurate way of optimizing the overlap, because it is sensitive to some horizontal tilting of the cell, which cannot be completely avoided.

Detection

After passing the sample cell, the relative orientation of broadband probe and reference pulses was rotated from horizontal to vertical using a periscope. The pulses were then recollimated and focussed onto the entrance slit of a prism spectrometer using a combination of two or three quartz lenses. While setting up these lenses, it was made sure that both pulses could be separated after passing the prism and that the focus position was close to the cameras. The exact positions and focal lengths depended on the refractive index of the solvent and the distance between entrance slit and sample cell. An optical filter (BG18, Schott) was used to lower the intensity of residual laser fundamental. In the spectrometer box (Entwicklungsbüro Stresing, Berlin), the pulses passed a quartz lens, an equilateral quartz prism (EDP-50.8-UV, CVI Melles Griot) and a second quartz lens. The vertically displaced probe and reference pulses were separated with a set of two square aluminum mirrors and aligned toward the cameras. The optical pathlength after passing the prism had to be equal for probe and reference pulses to ensure equal horizontal widths of the dispersed pulses at the cameras. The horizontal positions were adjusted so that the pixels of both cameras were equally illuminated using a set of interference filters. For this, a LabView routine[27] allowing for a live scan of the camera signals was employed. The CCD cameras (Series 2000, Entwicklungsbüro Stresing, Berlin) were equipped with back-thinned full frame

transfer (FFT)-CCD image sensors (S7030-0906, Hamamatsu) and quartz windows as protection for the sensors. These possess quantum efficiencies of ≈ 40 % in the wavelength range $300 - 380$ nm and up to 90 % in the visible range of the spectrum. The sensor area was 512 (H) $\times$ 58 (V) pixels (12.3×1.4 mm). In FFT-CCDs, the charge generated at each of the vertical lines is collected in potential wells during the exposure period. The resulting 1D horizontal shift register is subsequently read out before starting the next data collection period. This results in faster readout rates compared to imaging CCD sensors, where every horizontal line must be read out individually to achieve a 2D picture. The FFT-CCD cameras were triggered with the laser frequency of 1010 Hz.

The single color probe and reference pulses were detected using a set of slow Si photodiodes (S1227-66BQ, Hamamatsu) that were read out using differential signaling to reduce noise due to electromagnetic interference. Additionally, the pump pulse intensity was monitored with a third photodiode to discriminate sample (pump pulse unblocked) and background (pump pulse blocked) signals. The respective photodiode signals were streamed into the data flow of the cameras.

The detection unit consisting of prism spectrometer, photodiodes and controller was developed in close collaboration with Gerhard Stresing (Entwicklungsbüro Stresing, Berlin), who also provided drivers and simple LabVIEW examples. The main features of the home-written LabVIEW program used for controlling the transient absorption experiment are given in Appendix A.

2.1.2 SIGNAL PROCESSING AND DATA ANALYSIS

Calculation of transient absorption

The calculation of transient absorption was done on-line using a LabVIEW routine. In transient absorption experiments, the observed time- and wavelength dependent signal is the difference $\Delta OD(\lambda, \Delta t)$ of absorption of excited and unexcited molecules A^* and A^0, respectively:

$$\Delta OD(\lambda, \Delta t) = A^*(\lambda, \Delta t) - A^0(\lambda) = (-\log T^*(\lambda, \Delta t)) - \left(-\log T^0(\lambda)\right) \ . \quad (1)$$

The sample and background transmission $T^*(\lambda, \Delta t)$ and $T^0(\lambda)$, respectively, were calculated according to

$$T^*(\lambda, \Delta t) = \frac{I^*_{pr}(\lambda, \Delta t)}{I^*_{ref}(\lambda, \Delta t)} \quad (2)$$

and

$$T^0(\lambda) = \frac{I^0_{pr}(\lambda)}{I^0_{ref}(\lambda)} \ , \quad (3)$$

with $T^*(\lambda, \Delta t)$ and $T^0(\lambda)$ being the transmissions of consecutive laser pulses. The background transmission was recorded to account for the different intensities of probe and reference pulses. The relative transmission

$$T_{rel}(\lambda, \Delta t) = \frac{T^*(\lambda, \Delta t)}{T^0(\lambda)} \tag{4}$$

was subsequently converted to the change of optical density

$$\Delta OD(\lambda, \Delta t) = -\log T_{rel}(\lambda, \Delta t) = (-\log T^*(\lambda, \Delta t)) - \left(-\log T^0(\lambda)\right) \tag{5}$$

which is equivalent to Equation 1. Instead of using probe and reference pulses, it is also common to use successive probe pulse intensities $I^*(\lambda, t)$ and $I^0(\lambda)$ as sample and background signal, respectively, calculating the change of optical density simply according to $\Delta OD(\lambda, t) = -\log \frac{I^*(\lambda,t)}{I^0(\lambda)}$. Although the respective experimental setup is less complicated, this procedure makes the measurement more dependent on pulse-to-pulse fluctuations.

Wavelength calibration

The pixels were assigned to wavelengths by placing a set of 9 band-pass interference filters with central wavelengths at 330 nm $\leqslant \lambda_{CWL} \leqslant$ 645 nm (Schott and Edmund Optics) in front of the cameras. The resulting transmission curves, together with a typical whitelight spectrum and the respective calibration curve are given in Figure 2.7.

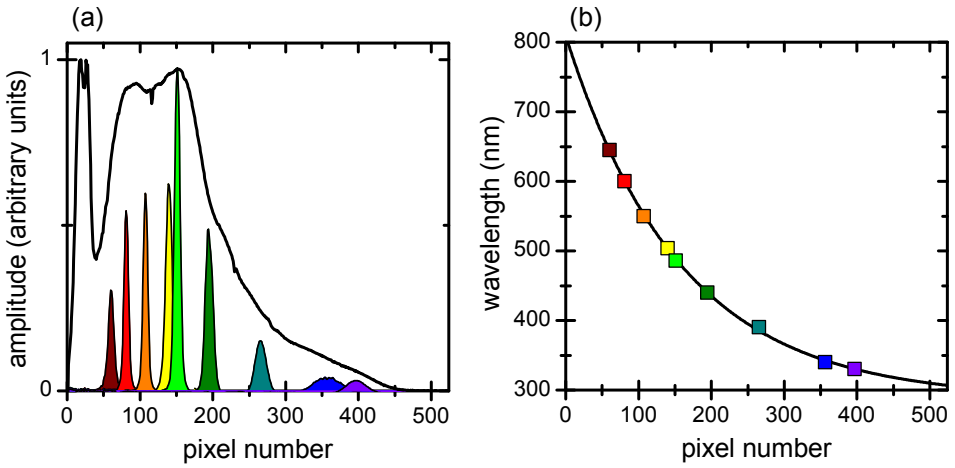

Figure 2.7: (a) Transmission curves of band-pass interference filters (colored) for wavelength calibration and whitelight spectrum (black line). (b) Plot of wavelength as function of pixel number. The squares indicate the transmission maxima of the interference filters, the black line is the calibration curve.

Sensitivity and single shot analysis

The reason for applying a single-shot readout rate is that the pulse-to-pulse noise of the laser fundamental is of the order of $\ll 0.5$ % (rms), while laser fluctuations are more pronounced on the time scale of a few seconds.[28] Consequently, when sample and background transmissions ($T^*(\lambda, \Delta t)$ and $T^0(\lambda)$) are averaged each over several hundred laser shots before calculating $\Delta OD(\lambda, \Delta t)$, the correlation of both is at least partially lost, resulting in a higher noise. The sensitivities that can be achieved with the single-shot readout mode are depicted in Figure 2.8(a) as gray squares for the broadband detection, expressed as standard deviation of ΔOD as a function of number of single measurements. The correlation of both is

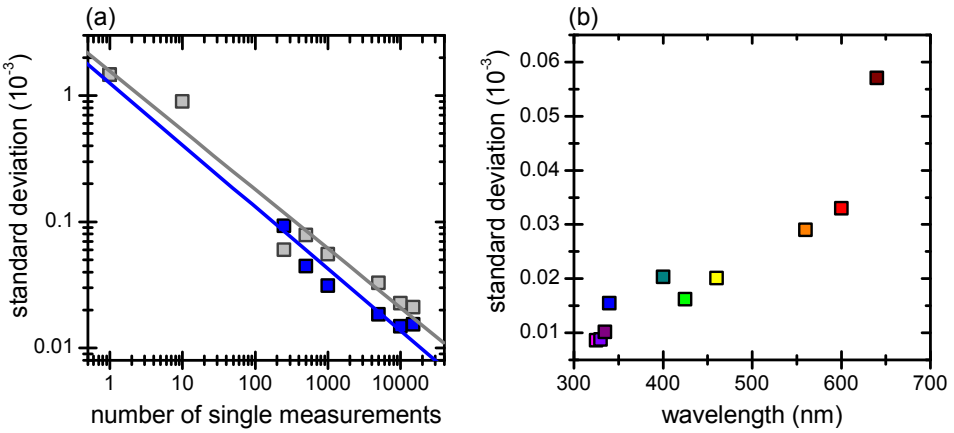

Figure 2.8: Standard deviations of change of optical density ΔOD at $\lambda_{probe} = 350nm$ (a) as function of number of single measurements before (gray) and after (blue) single shot analysis and (b) as function of probe wavelength (averaged over 5 nm and 5000 single measurements).

linear with a slope of ≈ 0.5, and transient absorption measurements with sensitivities ranging from $\approx 2 \times 10^{-3}$ in a single shot mode to $\leqslant 1 \times 10^{-5}$ when averaging over several thousand single measurements are feasible. The single-shot readout rate also allowed for a pulse discrimination to eliminate poor single measurements resulting from, e.g., dust particles in the optical pathway. This was performed on-line with a LabVIEW routine. Towards these ends, the mean value $\langle \Delta OD(\lambda) \rangle$ and the deviations $|\langle \Delta OD(\lambda) \rangle - \Delta OD(\lambda)|$ of single measurements were calculated. If the deviation from the mean exceeded a certain, experimentally optimized limit, the respective single measurements were discarded. Typically, a fraction of < 1 % of single measurements was eliminated. In Figure 2.8(a), the sensitivities after this correction are shown in blue, and the sensitivity increase by this single-shot analysis using $\geqslant 500$ single measurements per delay step is evident. For a smaller number of measurements, the applied simple discrimination method is not feasible. However, a more sophisticated approach would require more computing capacity or computing time, the latter leading to longer overall measuring times.

Recording $\geqslant$ 10000 single measurements per delay step should be avoided due to the high amount of data that is produced during such a measurement, which often results in LabVIEW bugs and erroneous results of the single-shot analysis. This becomes visible in the non-linear behavior of the "corrected" standard deviation at large numbers of single measurements in Figure 2.8(a). The best results were obtained using a series of scans each with 5000 single measurements per delay step.

The resulting sensitivities of such an experiment, averaged over three scans and consequently 15000 single measurements, are shown in Figure 2.8(b). Here, the sensitivities are plotted as function of probe wavelengths, each averaged over a constant wavelength range of 5 nm. The increase of sensitivity with decreasing probe wavelength is due to the higher spectral resolution toward the UV range (see above). Higher sensitivities in the visible were available by averaging over a constant energy range, if necessary.

In Figure 2.9, the sensitivity as function of number of single measurements is shown for the single-color detection, and a linear dependence with a slope of $\approx$ 0.5 is clearly visible. The sensitivity is generally slightly

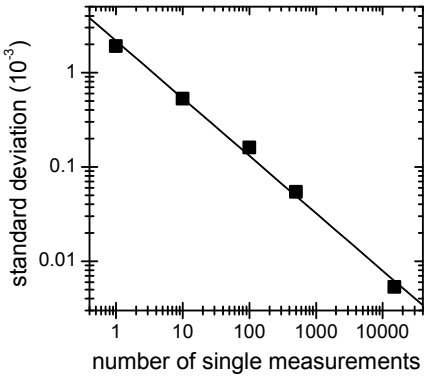

Figure 2.9: Standard deviations of change of optical density ΔOD for single color detection at $\lambda_{probe} = 260$ nm.

better than for the broadband detection, but this depends highly on precise experimental conditions and probe wavelength. The single-shot analysis was equivalent to that of the broadband detection, and the same statements made above hold true for this case.

Data analysis

The chirp of the broadband probe pulses results in a shift of the experimental t_0 dependent on probe wavelength. The transient absorption signals were corrected for that chirp as described elsewhere.[23,25] Time profiles were obtained by averaging over 5 nm, which corresponds to $\approx$ 15 pixels in the UV and $\approx$ 3 pixels at $\lambda_{probe} \geqslant$ 600 nm. The time profiles were described in a global data analysis using a sum of exponentials of the form

$$S_\lambda(t) = \sum_i A_i \times \exp\left(-\frac{t}{\tau_i}\right) \tag{6}$$

with A_i as amplitude, t as delay time and τ_i as decay time. To take into account the instrument response function (IRF), limited by the respective temporal pump and probe pulse widths, the exponentials were convoluted with a Gaussian shaped function $G(t, \sigma_{IRF})$, resulting in

$$\Delta OD_\lambda(t) = S_\lambda(t) \otimes G(t, \sigma_{IRF}) \,, \tag{7}$$

with $IRF_{FWHM} = \sqrt{8 \times \ln 2} \times \sigma_{IRF}$ and σ_{IRF} as the time resolution of the experiment, which was usually ≈ 50 fs for broadband detection and ≈ 80 fs for single-color detection. Coherent and long-lived artifacts were taken into account by adding a solvent correction function $C_\lambda(t)$ that will be explained in the following.

Correction for transient artifacts

Beside the molecular contributions to transient absorption signals (cf. Sec. 2.1), there are always coherent signals present around $\Delta t = 0$. Among these are cross-phase modulation (XPM), resulting from the time-dependent modulation of refractive indices by the intense pump pulse and consequently a modulation of spectral distribution in the spectrally broad probe pulse. XPM leads to signals whose form and intensity is highly dependent on the chirp of the probe pulse and the intensity of the pump pulse.[26,29,30] Another coherent contribution is multi-photon absorption (MPA), usually a two-photon absorption (TPA), resulting in Gaussian-shaped contributions. Both XPM and MPA occur in sample cell windows and solvent.

The distinction and subsequent separation of artifacts and molecular contributions require a measurement of neat solvent and the determination of suitable scaling factors. These scaling factors are necessary due to the reduction of pump pulse intensity by absorption of sample molecules, resulting in less intense artifacts. A detailed analysis of the respective correlation was given by Lorenc et al.[26] and Dobryakov et al.[29,30] Although coherent artifacts can in some cases provide information about experimental parameters such as time resolution and chirp of pump and probe pulses,[23,26] their intensity needs to be reduced as much as possible to allow for a reliable analysis of transient absorption measurements. Therefore, the incident angles of pump and probe pulses and the pump pulse intensity were kept as low as possible. A further improvement was achieved by reducing the optical pathway to $d = 0.1$ mm. This is shown in Figure 2.10, where a comparison of coherent artifacts in flow cells filled with *n*-hexane with $d = 1$ mm and $d = 0.1$ mm is given. Here, it becomes clearly visible that the decrease of optical thickness results in a decreased magnitude and a reduction of the temporal width of coherent artifacts.

In water, MPA leads to the formation of solvated electrons, and the resulting long-lived solvated electron absorption (SEA) is a broad and unstructured absorption band at $\lambda_{probe} \geqslant 450$ nm.[31–37] The investigation of the formation and properties of solvated electrons in water have been the subject of intense research over the last decades.[31–33,35–40] A review by Siefermann and Abel gives a concise overview of this complex topic until

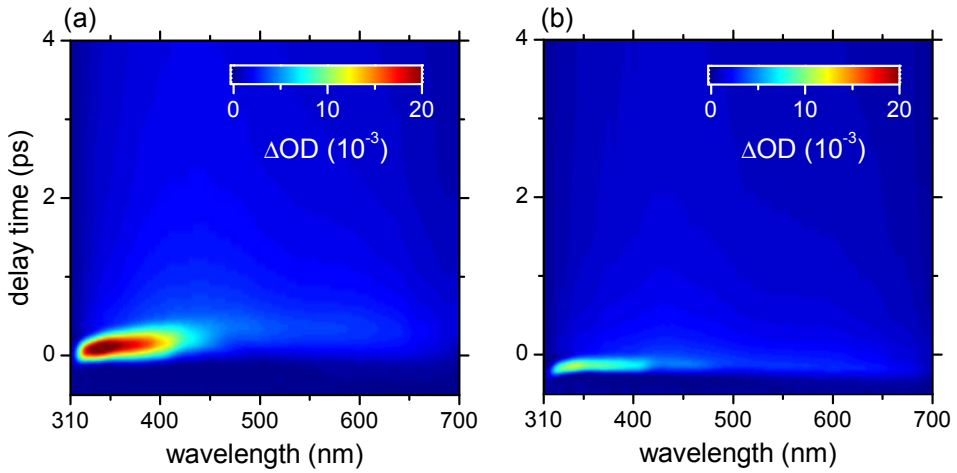

Figure 2.10: Two-dimensional representation of coherent artifacts at $\lambda_{pump} = 260$ nm measured in neat n-hexane using flow cells with optical path-length of (a) $d = 1$ mm and (b) $d = 0.1$ mm.

2011.[41] A distinction of coherent artifacts and SEA is vital for a reliable analysis of time profiles since the scaling factors are not identical, if the dependence on pump energy is different for both contributions. Figure 2.11(a) shows a typical result of a transient absorption experiment on neat water. In the UV range, coherent artifacts are more pronounced, while

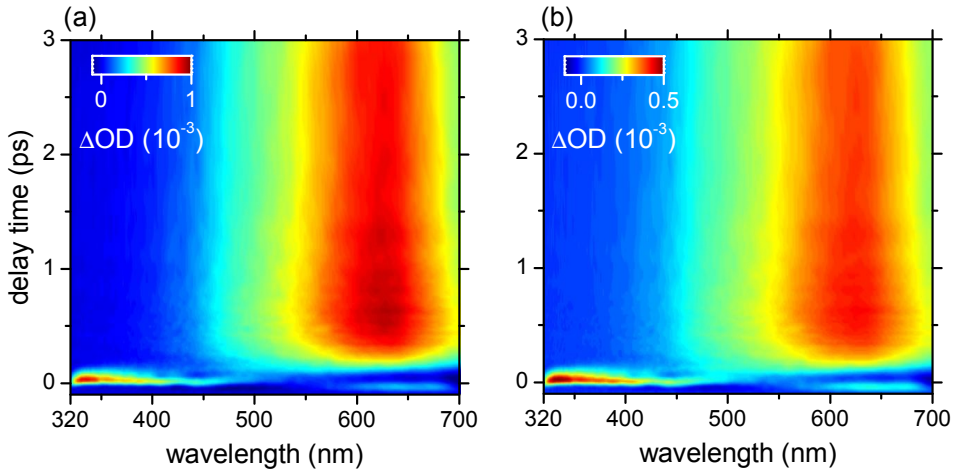

Figure 2.11: Two-dimensional representation of coherent signals and longer-lived solvated electron absorption in water excited at $\lambda_{pump} = 260$ nm ((a) unscaled result of transient absorption, (b) result scaled according to Equation 10

SEA dominates in the visible at $\lambda_{probe} \geqslant 450$ nm. This becomes also visible in Figure 2.12, where time profiles at $\lambda_{probe} = 335$ nm and $\lambda_{probe} = 640$ nm of the water measurement shown in Figure 2.11 are given. The coherent artifacts were described using a sum of Gaussian shaped functions $G_i(t)$, shown in red in Figure 2.12, and the long-lived SEA contribution with a sum of exponentials convoluted with a Gaussian ($F_j(t)$) equivalent

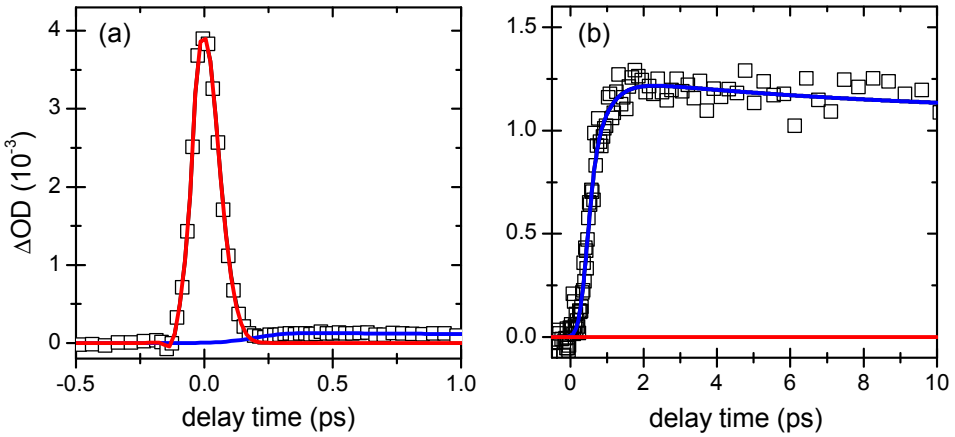

Figure 2.12: Time profiles of water at (a) $\lambda_{probe} = 335$ nm and (b) $\lambda_{probe} = 640$ nm after excitation at $\lambda_{pump} = 260$ nm. Open squares represent the data points, red lines indicate a sum of Gaussian shaped functions describing coherent artifacts, blue lines a sum of exponentials describing SEA.

to Equation 7, shown in blue. The overall function describing the solvent contribution was

$$C_\lambda^0(t) = \sum_i G_i(t) + \sum_j F_j(t) \,, \tag{8}$$

which was extended by the scaling factors d and e for coherent and long-lived contributions, respectively:

$$C_\lambda(t) = d \times \sum_i G_i(t) + e \times \sum_j F_j(t) \tag{9}$$

with $0 < d < 1$ and $0 < e < 1$. Equation 9 was employed for the global data analysis of time profiles with d and e as free-floating parameters.

The respective correction of the two-dimensional plots and transient spectra was performed using the resulting scaling factors. If d and e were found to be different, this correction was done using a suitable switching function that allowed for a smooth transition from the region around t_0, where coherent contributions dominate, to delay times $\gg t_0$, where SEA is present. The difficulty is the description of the transition range, because SEA shows a delayed rise[33,34] and is overlapping with the coherent signal for ≈ 200 fs. This becomes visible in Figure 2.13, where a typical water signal was averaged over all probe wavelength. A model fit according to Equation 8 was applied, yielding rise time σ_{solv} and "time zero" $t_{0,solv}$ of SEA. These parameters were then included in a suitable tanh function that describes the above mentioned smooth transition from coherent to long-lived contributions. If $d > e$, this functions is

$$\gamma = -\tanh\left(\frac{t - t_{0,solv}}{\sigma_{solv}}\right) \times \frac{d-e}{2} + \frac{|d-e|}{2} + e \tag{10}$$

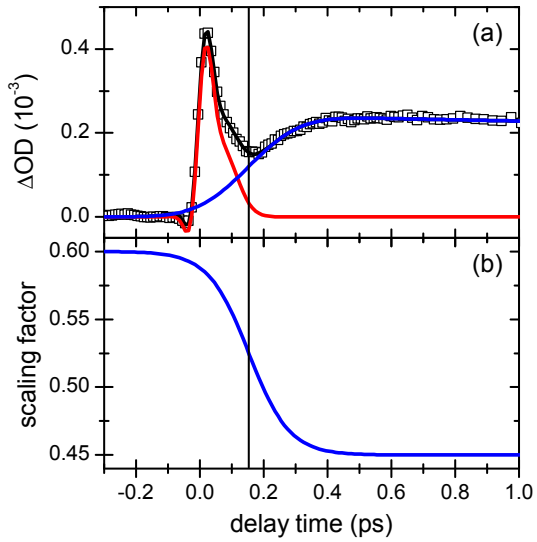

Figure 2.13: (a) Transient absorption of water, averaged over all probe wavelength. Open squares represent the data points, red lines indicate a sum of Gaussian shaped functions describing coherent artifacts, blue lines a sum of exponentials describing SEA. (b) Resulting correction function according to Equation 10 for the water signal with $d = 0.6$ and $e = 0.45$. The vertical line indicates $t_{0,solv}$.

and if $e > d$

$$\gamma = -\tanh\left(\frac{t - t_{0,solv}}{\sigma_{solv}}\right) \times \frac{d - e}{2} + \frac{|d - e|}{2} + d\,. \tag{11}$$

The respective function was multiplied with the results of the solvent measurement and this scaled solvent signal subtracted from the sample measurement. Figure 2.11(b) shows such a scaled signal. It can be seen that the relative intensities of coherent artifacts and SEA are reversed compared to the unscaled signal in Figure 2.11(a). Fortunately, in most experimental measurements performed in this Thesis, the coherent contribution and SEA were small (SEA being almost negligible in some cases) compared to the molecular signals of interest.

2.2 Femtosecond time-resolved fluorescence up-conversion spectroscopy

A scheme of the femtosecond time-resolved fluorescence up-conversion experiment that was used in this Thesis is shown in Figure 2.14. As for the transient absorption experiment, a pump-probe scheme was applied for the time-resolved detection of fluorescence photons. In this experiment, an ultrashort pump pulse excites the molecules and the emitted fluorescence photons are up-converted with the laser fundamental, which serves as probe or gate pulse and can be delayed with respect to the pump pulse. Detection of the resulting sum frequency allows to follow the decay of fluorescence intensity at discrete times after excitation. Many more theo-

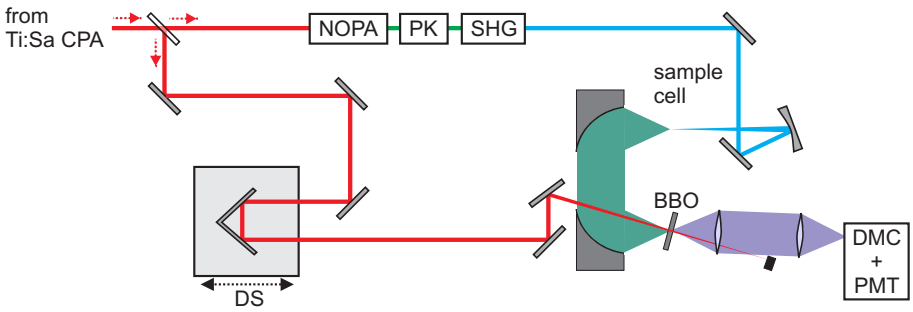

BBO	β-BaB_2O_4 crystal	PK	prism compressor
DMC	double monochromator	PMT	photomultiplier (connected to PC)
DS	delay stage with retroreflector	SHG	second harmonic generation
NOPA	non-collinear optical parametric amplifier		

Figure 2.14: Schematic overview of the fluorescence up-conversion experiment. The color scheme was chosen for clarity and does not reflect the experimental wavelengths.

retical and experimental details on the up-conversion experiment can be found in several previous PhD Thesis.[1,2]

Briefly, the pump pulses were generated in a NOPA with subsequent pulse compression and frequency doubling (see transient absorption setup, Sec. 2.1.1). The fluorescence photons were collected using two 90° off-axis parabolic mirrors and focussed into a BBO optimized for type I sum frequency generation. For the time-delayed gate pulses, $\approx$ 70 µJ of the laser fundamental were used. The up-converted photons were detected with a double monochromator equipped with a single photon counting unit in the wavelength range $211 \leqslant \lambda_{SFG} \leqslant 325$ nm, corresponding to fluorescence wavelength of $290 \leqslant \lambda_{fl} \leqslant 560$ nm. Suitable filters (Schott) were used to block the frequency-double laser fundamental at $\lambda = 387$ nm and residual pump pulse intensity. Flow cells with optical pathlengths of 1 mm were used and the concentrations adjusted to optical densities of $\leqslant 0.5$ at the respective excitation wavelengths.

BIBLIOGRAPHY

[1] Pancur, T. Untersuchung der Isomerisierungsdynamik von Azobenzolen und der strahlungslosen Desaktivierung von Nukleobasen mit Hilfe der Femtosekunden-Fluoreszenzspektroskopie. Ph.D. Thesis, Christian-Albrechts-Universität zu Kiel, 2004.

[2] Schwalb, N. K. Ultrafast Electronic Deactivation Dynamics in DNA Model Systems by Femtosecond UV Fluorescence Spectroscopy. Ph.D. Thesis, Christian-Albrechts-Universität zu Kiel, 2009.

[3] Schwalb, N. K.; Temps, F. *J. Am. Chem. Soc.* **2007**, *129*, 9272–9273.

[4] Schwalb, N. K.; Temps, F. *J. Photochem. Photobiol., A* **2009**, *208*, 164–170.

[5] Schwalb, N. K.; Temps, F. *J. Phys. Chem. A* **2009**, *113*, 13113–13123.

[6] Schwalb, N. K.; Michalak, T.; Temps, F. *J. Phys. Chem. B* **2009**, *113*, 16365–16376.

[7] Stuhldreier, M. C.; Schüler, C.; Kleber, J.; Temps, F. *Ultrafast Phenomena XVII* **2011**, 553–555.

[8] Stuhldreier, M. C.; Temps, F. *Faraday Discuss.* **2013**, *163*, DOI: 10.1039/C3FD00003F.

[9] Stuhldreier, M. C.; Malicki, M.; Röttger, K.; Schüler, C.; Kleber, J.; Muskat, T.; Temps, F. **2013**, manuscript in preparation.

[10] Röttger, K.; Schwalb, N. K.; Temps, F. *J. Phys. Chem. A* **2013**, *117*, 2469–2478.

[11] Röttger, K.; Sönnichsen, F. D.; Temps, F. **2013**, manuscript in preparation.

[12] Bahrenburg, J.; Röttger, K.; Siewertsen, R.; Renth, F.; Temps, F. *Photochem. Photobiol. Sci.* **2012**, *11*, 1210–1219.

[13] Yang, M.; Szyc, L.; Röttger, K.; Fidder, H.; Nibbering, E. T. J.; Elsaesser, T.; Temps, F. *J. Phys. Chem. B* **2011**, *115*, 5484–5492.

[14] Fidder, H.; Yang, M.; Nibbering, E. T. J.; Elsaesser, T.; Röttger, K.; Temps, F. *J. Phys. Chem. A* **2013**, *117*, 845–854.

[15] Mukamel, S. *Principles of Nonlinear Optical Spectroscopy*; Oxford Series in Optical and Imaging Sciences; Oxford University Press: New York, 1995.

[16] Demtröder, W. *Laserspektroskopie: Grundlagen und Techniken*; Springer, Berlin, 2000.

[17] Boyd, R. W. *Nonlinear Optics*; Elsevier Inc., Amsterdam, 2008.

[18] Weiner, A. M. In *Ultrafast Optics*; Boreman, G. D., Ed.; Wiley Series in Pure and Applied Optics; John Wiley & Sons: Hoboken, New Jersey, 2009.

[19] Studzinski, H. Ultrafast Radiationless Dynamics of Selected Electronically Excited Aromatic Molecules by Femtosecond Time-Resolved Mass Spectrometry and Photoelectron Imaging. Ph.D. Thesis, Christian-Albrechts-Universität zu Kiel, 2007.

[20] Foca, M. Investigations of Ultrafast Photoisomerization of Photochromic Molecular Switches by fs-Time-Resolved Transient Absorption Spectroscopy. Ph.D. Thesis, Christian-Albrechts-Universität zu Kiel, 2005.

[21] Wilhelm, T.; Piel, J.; Riedle, E. *Opt. Lett. 22*, 1494–1496.

[22] Cerullo, G.; De Sivestri, S. *Rev. Sci. Instrum.* **2003**, *74*, 1–18.

[23] Siewertsen, R. Ultrafast Photochromic Reactions of Structurally Modified Furylfulgides and a Bridged Azobenzene. Ph.D. Thesis, Christian-Albrechts-Universität zu Kiel, 2011.

[24] SNLO nonlinear optics code available from A. V. Smith, AS-Photonics, Albuquerque, NM. `http://www.as-photonics.com/SNLO`.

[25] Megerle, U.; Pugliesi, I.; Schriever, C.; Sailer, C. F.; Riedle, E. *Appl. Phys. B: Lasers Opt.* **2009**, *96*, 215–231.

[26] Lorenc, M.; Ziolek, M.; Naskrecki, R.; Karolczak, J.; Kubicki, J.; Maciejewski, A. *Appl. Phys. B: Lasers Opt.* **2002**, *74*, 19–27.

[27] LabVIEW 8.6. National Instruments, 2008.

[28] Schriever, C.; Lochbrunner, S.; Riedle, E.; Nesbitt, D. J. *Rev. Sci. Instrum.* **2008**, *79*, 013107/1–013107/9.

[29] Dobryakov, A. L.; Kovalenko, S. A.; Ernsting, N. P. *J. Chem. Phys.* **2003**, *119*, 988–1002.

[30] Dobryakov, A. L.; Kovalenko, S. A.; Ernsting, N. P. *J. Chem. Phys.* **2005**, *123*, 044502.

[31] Pepin, C.; Goulet, T.; Houde, D.; Jay-Gerin, J.-P. *J. Phys. Chem. A* **1997**, *101*, 4351–4360.

[32] Thomsen, C. L.; Madsen, D.; Keiding, S. R.; Thogersen, J.; Christiansen, O. *J. Chem. Phys.* **1999**, *110*, 3453–3462.

[33] Hertwig, A.; Hippler, H.; Unterreiner, A.-N. *Phys. Chem. Chem. Phys.* **1999**, *1*, 5633–5642.

[34] Peon, J.; Hess, G. C.; Pecourt, J.-M. L.; Yuzawa, T.; Kohler, B. *J. Phys. Chem. A* **1999**, *103*, 2460–2466.

[35] Laenen, R.; Roth, T.; Laubereau, A. *Phys. Rev. Lett.* **2000**, *85*, 50–53.

[36] Elles, C. G.; Jailaubekov, A. E.; Crowell, R. A.; Bradforth, S. E. *J. Chem. Phys.* **2006**, *125*, 044515/1–044515/12.

[37] Elles, C. G.; Shkrob, I. A.; Crowell, R. A.; Bradforth, S. E. *J. Chem. Phys.* **2007**, *126*, 164503/1–164503/8.

[38] Hart, E. J.; Boag, J. W. *J. Am. Chem. Soc.* **1962**, *84*, 4090–4095.

[39] Goulet, T.; Pepin, C.; Houde, D.; Jay-Gerin, J.-P. *Radiat. Phys. Chem.* **1999**, *54*, 441–448.

[40] Siefermann, K. R.; Liu, Y.; Lugovoy, E.; Link, O.; Faubel, M.; Buck, U.; Winter, B.; Abel, B. *Nat. Chem.* **2010**, *2*, 274–279.

[41] Siefermann, K. R.; Abel, B. *Angew. Chem., Int. Ed.* **2011**, *50*, 5264–5272.

Part II

RESULTS AND DISCUSSION

3

ULTRAFAST ELECTRONIC DEACTIVATION DYNAMICS OF XANTHOSINE MONOPHOSPHATE

Katharina Röttger, Mayra C. Stuhldreier, Friedrich Temps*

Institut für Physikalische Chemie, Christian-Albrechts-Universität zu Kiel, Olshausenstr. 40, 24098 Kiel, Germany

manuscript in preparation

OWN CONTRIBUTIONS TO THIS MANUSCRIPT:

- Femtosecond time-resolved transient absorption spectroscopy
- Femtosecond time-resolved fluorescence up-conversion spectroscopy (together with Mayra Stuhldreier)
- Static spectroscopy
- Analysis of all time-resolved data
- Writing of the manuscript

* To whom correspondence should be addressed. E-mail: temps@phc.uni-kiel.de

ABSTRACT

The excited-state dynamics of the 6-oxopurine xanthosine monophosphate (XMP) have been investigated by means of femtosecond time-resolved transient absorption and fluorescence up-conversion spectroscopy in dependence of excitation energy and protonation state. The observed excited-state behavior differs significantly from that of other purine bases and was attributed to a dominating relaxation channel via the out-of-plane deformation of the five-membered ring within $\approx$ 1 ps. This excited-state pathway was discussed in terms of structural and electronic properties of XMP compared to other purine nucleotides, where the relaxation occurs via the deformation of the six-membered ring.

3.1 INTRODUCTION

The 6-oxopurine xanthine, its nucleoside xanthosine and the nucleotide xanthosine monophosphate (XMP) play a variety of roles in biological systems. The most important and well-known function is as an intermediate in different metabolic pathways, such as oxidative guanine deamination, the formation of GMP via XMP,[1] and the caffeine biosynthesis by methylation of xanthosine.[2] Additionally, it is a rare RNA base.[1] Xanthine differs from guanine only by a carbonyl group at the C(2) position instead of the amino group and therefore possesses no double bond at the C(2)-N(3) position (see Scheme 3.1). This leads to some remarkable changes of the electronic structure. In particular, it increases the acidity of the N(1)H and N(3)H group in the six-membered ring compared to all other common purine bases. The gas phase and solution structures have been extensively studied during the last decades[3–8], and the electronic properties have been investigated experimentally[9–12] as well as theoretically.[13] In solution, different pH values were employed to investigate tautomerism and protonation state.

The photophysics of the two lowest tautomers of xanthine, the N(9)H and the N(7)H diketo tautomers, have recently been investigated theoretically by Yamazaki et al.[14] They proposed two relaxation mechanisms from the electronically excited state to the electronic ground state: On the one hand, a conical intersection (CI) between the first $\pi\pi^*$ state and the ground state was found which is reached via the out-of-plane deformation of the five-membered ring. This relaxation was predicted to be more likely for the N(7)H tautomer, while the N(9)H tautomer is supposed to exhibit a small potential energy barrier en route to this conical intersection. The second relaxation pathway back to the electronic ground state was found to proceed via NH dissociation in the five-membered ring, which is assumed to be more likely for the N(9)H tautomer. For the nucleoside and nucleotide, this relaxation channel is not possible. The photodynamics should therefore be controlled by the ring puckering of the 5-membered ring as deactivation pathway. This makes for an important difference to other purine bases like guanine and adenine, where the out-of-plane de-

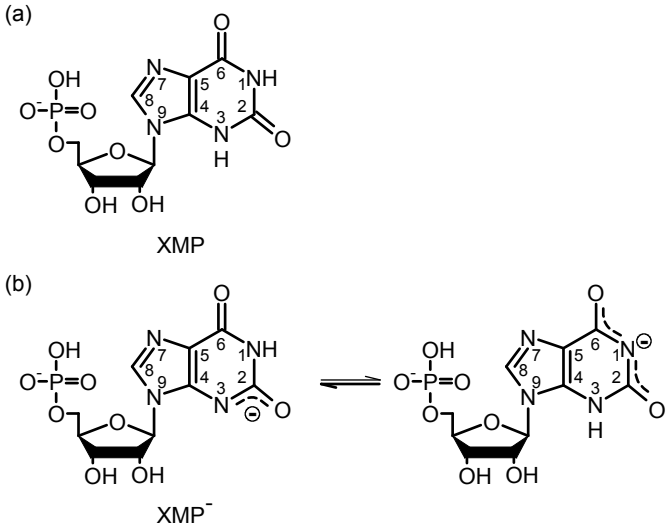

Figure 3.1: Structures and numbering scheme of xanthosine monophosphate at (a) acidic conditions with 1.1 < pH < 5.5 and (b) neutral conditions at pH> 5.5.

formation of the six-membered ring was found to be relevant for electronic deactivation.[15–20]

In this work, we focused on the photodynamics of the nucleotide XMP. This was done for two reasons: First, the number of possible tautomers is reduced to the N(9)R keto form by the ribosyl group at the N(9) position. Secondly, xanthosine monophosphate is, unlike xanthine and xanthosine, soluble in aqueous solution to a degree which allows for time-resolved spectroscopy in solution at room temperature.

Experimental studies on XMP have so far been scarce, but the structural properties and tautomeric equilibria in aqueous solution are well-known by the investigation of micro-acidity constants of the N(1)H and N(3)H group by Massoud et al.[21] Additionally, the structure has been studied by means of resonance Raman spectra by Gogia et al.[8] The results of both groups revealed that in contrast to xanthine, XMP is deprotonated at physiological pH values in the xanthine moiety, preferentially at the N(3) position. Gogia et al. showed that the deprotonation leads to a weakening of both carbonyl bonds, especially at the C(2)O position, due to electron delocalization following the proton loss (cf. Fig. 3.1). In the free, neutral purine base xanthine, on the other hand, a considerable amount of conjugation was found between the NH and the carbonyl groups in the six-membered ring, as was shown by X-ray photoemission and NEXAFS spectroscopy.[12] The electronic structures of both species, namely XMP with the neutral and the anionic xanthine moiety, might therefore be quite similar regarding the degree of delocalization. XMP with a neutral xanthine moiety exist exclusively only at pH < 5.5.[21] In the following, we will refer to the nucleotide with the neutral xanthine moiety as XMP and with the deprotonated xanthine moiety as XMP^{-}.

5′-Xanthosine monophosphate was purchased as disodium salt from Sequoia Research Products and used as received. XMP was prepared in an acetate buffer at pH 3.6 and XMP^- in a phosphate buffer at pH 7. Concentrations of 10 mM and $0.5 - 1$ mM were used for transient absorption and fluorescence up-conversion measurements, respectively. Acetate and phosphate buffer were prepared with double-distilled water purchased from Carl Roth. Sodium acetate, acetic acid, Na_2HPO_4 and NaH_2PO_4 were purchased from Sigma-Aldrich in BioUltra quality. Sodium chloride (Sigma-Aldrich, BioUltra) was added to the phosphate buffer to adjust the salt concentration to the physiological salt concentration. The purity and concentration of each compound was checked before and after each time-resolved experiment with static UV/vis absorption and fluorescence spectroscopy. Static absorption spectra were recorded with a Shimadzu UV-2401 desktop spectrometer. Static fluorescence spectra were measured with a Horiba Jobin Yvon Fluoromax 4 spectrometer.

The setups of the time-resolved transient absorption and fluorescence up-conversion experiments in our laboratory have been described in some detail elsewhere.[22–24] Both experiments were pumped with a regeneratively amplified 1 kHz Ti:Sa laser system (Clark MXR CPA 2001) providing pulses with $\approx$ 150 fs (FWHM) duration and 1000 µJ at $\lambda = 775$ nm. 500 µJ of the laser output was used for the transient absorption setup and 400 µJ for fluorescence up-conversion. The pump pulses for both experiments were generated in home-built non-collinear optical parametric amplifiers (NOPA) with subsequent frequency doubling and focused into the respective sample flow cells.

In the up-conversion experiment, the fluorescence was collected with a pair of two off-axis parabolic mirrors and focused into a BBO crystal for non-collinear type I sum frequency generation (SFG). Residual pump light after the sample cell was blocked with a beam stop and a WG320 or WG295 (Schott) filter, depending on the detection wavelength. The required time-delayed gate pulses were delivered by the Ti:Sa laser fundamental. The resulting SFG signal was detected with a computer-controlled single-photon counting unit at selected fluorescence wavelengths of 290 nm $\leqslant \lambda_{fluo} \leqslant$ 560 nm.

The broadband probe pulses for the transient absorption experiment were generated via supercontinuum generation in CaF_2, yielding a spectrum from 330 nm $\leqslant \lambda_{probe} \leqslant$ 700 nm. Additional single color probe pulses in the UV range were generated in a second NOPA and frequency doubling stage. Probe and reference pulses for the broadband and single color detection were obtained by using the front- and back reflection from a planar glass plate. Pump, probe and reference were focused into the sample cell, where the pump pulses were spatially and temporally overlapped with both probe pulses, and the reference pulses passed the unexcited sample next to the pump pulses. After passing the sample cell, the broadband probe and reference pulses were detected with a set of full frame transfer

(FFT) back-thinned CCD cameras (S7030-0906, Hamamatsu and Entwicklungsbüro Stresing, Berlin) after dispersion in a prism spectrograph. The UV single color pulses were recorded with two matched slow photodiodes (S1227-66BQ, Hamamatsu and Entwicklungsbüro Stresing, Berlin). Both cameras and photodiodes were read out simultaneously after each laser shot using LABVIEW software.[25]

To avoid the accumulation of photoproducts and thermally excited molecules, all time-resolved measurements were performed in flow cells, where the sample volume was exchanged between two consecutive laser shots. The pump pulse energies were reduced to $\leqslant$ 200 µJ and $\leqslant$ 120 µJ for the absorption and fluorescence measurements, respectively. The optical pathlength in the time-resolved absorption measurements was $d = 0.1$ mm to keep unwanted signals from the solvent, such as cross-phase modulation (XPM) and the long-lived absorption of solvated electrons (SEA) generated by multi-photon absorption, as low as possible.[26] To allow for an accurate correction for those artifacts, the pure solvent was measured directly after each sample measurement. The pathlength in the fluorescence up-conversion measurements was $d = 1$ mm. To ensure the reproducibility and reliability of the measurements, each fluorescence measurement was repeated at least twice and each transient absorption scan three times. The observed decay time profiles were analyzed using a nonlinear least-squares fitting routine based on the Levenberg-Marquardt algorithm implemented in the MATHEMATICA software.[27] Each profile was described by a sum of up to four exponentials convoluted with the instrument response function. Global fitting routines were used where possible (details will be given in the results section). The experimental time resolutions were on the order of $\Delta\tau = 50$ fs and $\Delta\tau = 150$ fs for the absorption and fluorescence up-conversion data, respectively.

3.3 RESULTS

STATIC ABSORPTION AND FLUORESCENCE SPECTRA

The static absorption and fluorescence spectra of XMP and XMP^- are depicted in Fig. 3.2. As it has been discussed by Cavalieri et al.[3] and Lichtenberg et al.,[4] both species exhibit two strong absorption bands in the UV, which can be attributed to two close-lying $\pi\pi^*$ transitions as in other purine bases. The spectral characteristics of both bands are summarized in Table 3.1. Compared to the unprotonated XMP at acidic conditions, both $\pi\pi^*$ transitions in the deprotonated XMP^- are red shifted by $\approx 9-15$ nm and the second $\pi\pi^*$ transition gains intensity on the expense of the first. The fluorescence spectra of both species feature a broad and unstructured band with a maximum at 390 nm (XMP) and at 350 nm (XMP^-). Interestingly, the emission maximum for XMP is red-shifted compared to XMP^-, which is in contrast to the shifts of the absorption maxima. This indicates a considerably larger energy difference from the initially populated Franck-

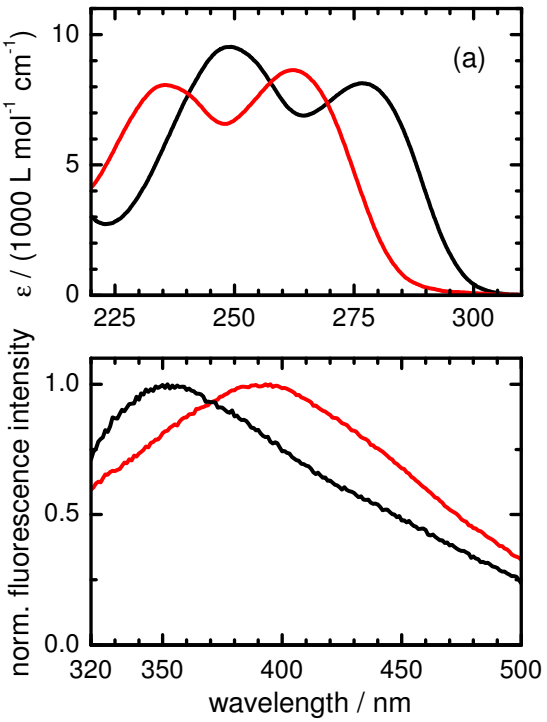

Figure 3.2: Static (a) absorption and (b) fluorescence spectra after excitation with 260 nm of XMP (red) and XMP^- (black).

Table 3.1: Absorption maxima and extinction coefficients for XMP and XMP^-.

	XMP	XMP^-
λ_{max1} (nm)	263	277
ϵ_{max1} (L mol^{-1} cm^{-1})	8620	8140
λ_{max2} (nm)	235	249
ϵ_{max2} (L mol^{-1} cm^{-1})	8070	9530

Condon region towards the minimum of the S_1 state as will be discussed below in the context of the time-resolved results.

TIME-RESOLVED EXPERIMENTS

XMP

For the time-resolved experiments of XMP, two pump wavelengths were used, $\lambda_{pump} = 260$ nm (fluorescence and absorption) and $\lambda_{pump} = 243$ nm (absorption). Inspecting the static absorption spectra (Fig. 3.2), the S_1 and S_2 states are populated with fractions of 83% and 17% ($\lambda_{pump} = 260$ nm) and 10% and 90% ($\lambda_{pump} = 243$ nm), respectively.

Fluorescence lifetimes after excitation at $\lambda_{pump} = 260$ nm were measured at six fluorescence wavelengths from 290 nm $\leqslant \lambda_{fluo} \leqslant$ 560 nm to gain insight into the dynamics of the optically bright state(s). The fluorescence time traces are shown in Fig. 3.3. A global data analysis yielded two dom-

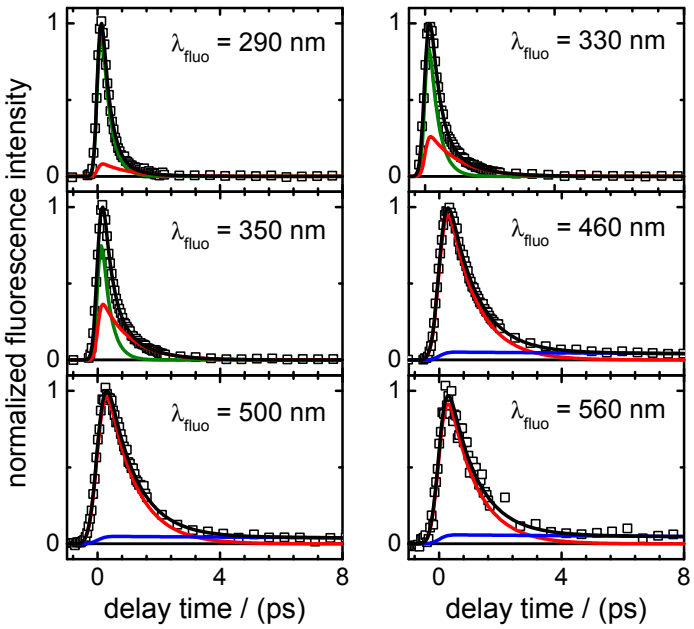

Figure 3.3: Fluorescence time profiles of XMP after excitation at $\lambda_{pump} = 260$ nm measured at six fluorescence wavelengths from 290 nm $\leqslant \lambda_{fluo} \leqslant$ 560 nm. Open squares represent the data points and black lines the overall fit function. The single contributions are shown in green ($\tau_{1,fluo}$), red ($\tau_{2,fluo}$), and blue ($\tau_{3,fluo}$).

inating time constants with

$$\tau_{1,fluo} = 0.28 \pm 0.01 \text{ ps},$$
$$\tau_{2,fluo} = 0.91 \pm 0.01 \text{ ps}.$$

At $\lambda_{fluo} \leqslant 460$ nm, a minor contribution decaying with $\tau_{3,fluo} = 36 \pm 8$ ps with very small amplitudes was found. The results of the data analysis are summarized in Table 3.2. The fast decaying contribution with $\tau_{1,fluo}$ was

Table 3.2: Decay times τ_i and relative amplitudes A_i from the data analysis of fluorescence up-conversion measurements after excitation of XMP at 260 nm (2σ error limits of last digits in parentheses).

λ_{fluo}/nm	$\tau_{1,fluo}$/ps	$A_{1,fluo}$	$\tau_{2,fluo}$/ps	$A_{2,fluo}$	$\tau_{3,fluo}$/ps	$A_{3,fluo}$
290	0.28(1)	0.94(6)	0.91(1)	0.06(3)	–	–
330	0.28(1)	0.82(2)	0.91(1)	0.18(1)	–	–
350	0.28(1)	0.74(2)	0.91(1)	0.26(1)	–	–
460	–	–	0.91(1)	0.96(1)	36(8)	0.035(4)
500	–	–	0.91(1)	0.97(1)	36(8)	0.033(5)
560	–	–	0.91(1)	0.96(8)	36(8)	0.04(3)

found only at $\lambda_{fluo} \leqslant 350$ nm and resembles the spectral range and decay time of the stimulated emission contribution to the transient absorption results (see below). The component decaying with $\tau_{2,fluo}$ was found to be dominating at all fluorescence wavelengths $\geqslant 460$ nm. The long-lived component contributed with amplitudes of $\leqslant 5\%$ little to the overall signal at $\lambda_{fluo} \geqslant 350$ nm. It was not observed at $\lambda_{fluo} < 350$ nm.

The results of the broadband transient absorption experiments of XMP for pump wavelengths $\lambda_{pump} = 260$ nm and $\lambda_{pump} = 243$ nm are shown in Figure 3.4. Both two-dimensional maps are similar and feature three

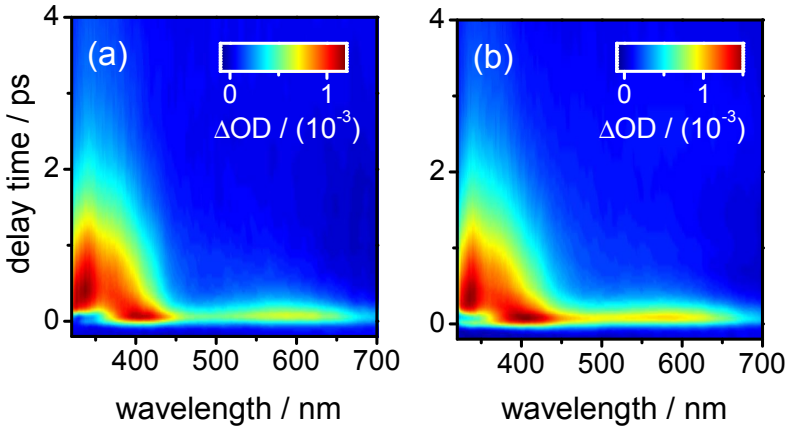

Figure 3.4: Two-dimensional maps of the observed transient absorption changes after excitation of XMP at (a) 260 nm and (b) 243 nm.

overlapping positive bands with maxima at $\lambda_{probe} \approx 340$ nm, 420 nm, and 600 nm. In the UV probe wavelength range, a negative contribution leads to a delayed rise of the positive band. Furthermore, the band at 420 nm seems to feature a slight blue-shift of the maximum within the first 500 fs. This is most likely a result of the fast-decaying negative contribution at UV wavelengths. The positive contributions are attributed to excited state absorption (ESA). The negative contribution in the UV probe wavelength

range is assigned to stimulated emission (SE), consistent with the fluorescence up-conversion measurements above.

For data analysis, $3-4$ time profiles were chosen out of every spectral range for both excitation wavelengths. Two exemplary time profiles together with the results of the data evaluation for each λ_{pump} are depicted in Figure 3.5 (top and middle row). The decay times and amplitudes of the

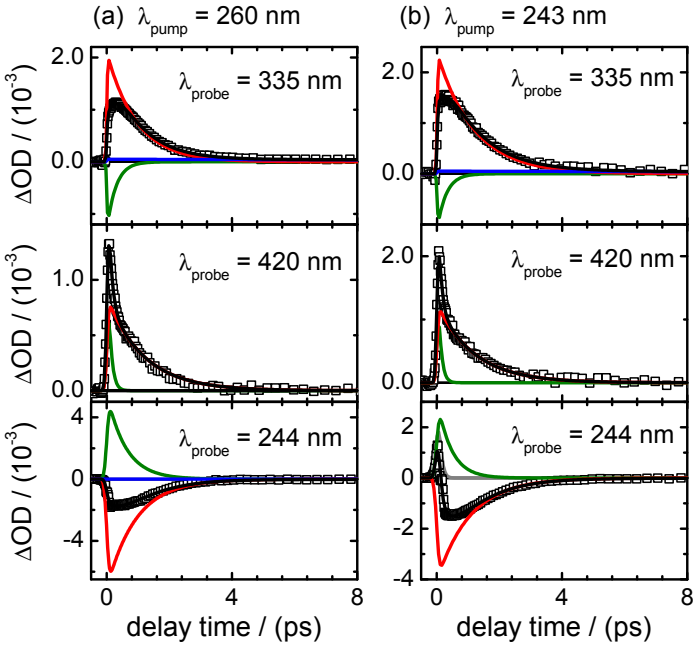

Figure 3.5: Time profiles of transient absorption changes after excitation of XMP with (a) 260 nm and (b) 243 nm. Open squares represent the data points and black lines the overall fit functions. The single contributions are shown in green (τ_1), red (τ_2), and blue (τ_3). The gray component decays with $\tau_1' \leqslant 0.07$ ps.)

data analysis are summarized in Tables 3.3 and 3.4 for $\lambda_{pump} = 260$ nm and $\lambda_{pump} = 243$ nm, respectively. Two dominating decay times were necessary for a satisfactory description of the transient absorption changes:

$$\tau_1 \approx 0.2 \text{ ps},$$
$$\tau_2 \approx 1 \text{ ps}$$

The respective contributions were found over the whole detection range for both pump wavelengths. The sub-picosecond decay time described the initial fast decay of the positive signals at $\lambda_{probe} \geqslant 400$ nm with amplitudes of $\approx 3-80\%$. The amplitude of this component increased with increasing probe wavelengths on the expense of τ_2. It was also found as the decay time of the SE contribution at UV probe wavelengths and is consistent with the fast-decaying component $\tau_{1,fluo}$. The SE contribution is more pronounced for XMP than for all other purine bases in water, which is most likely the result of the strong emission intensity within the first picosecond (cf. Fig. 3.3). A long-lived contribution decaying with $\tau_3 = 36$ ps plays only

Table 3.3: Decay times τ_i and amplitudes A_i from the data analysis of transient absorption changes of broadband and single color detection at λ_{probe} = 244 nm after excitation of XMP at 260 nm (2σ error limits of last digits in parentheses). The value of τ_3 was fixed to the decay time found in the fluorescence measurements.

λ_{probe}/nm	τ_1/ps	$A_1/10^{-3}$	τ_2/ps	$A_2/10^{-3}$	τ_3/ps	$A_3/10^{-3}$
244	0.6(4)	7(7)	0.9(4)	−8(8)	–	–
325	0.3(2)	−0.75(75)	0.9(4)	1.7(9)	36(–)	0.02(2)
330	0.3(2)	−1.0(10)	0.9(4)	2.0(1)	36(–)	0.04(4)
335	0.3(2)	−1.3(12)	0.9(4)	2.1(12)	36(–)	0.05(5)
400	0.10(4)	0.2(2)	1.2(2)	1.1(2)	–	–
420	0.10(4)	1.3(6)	1.2(2)	0.8(2)	–	–
425	0.10(4)	1.4(6)	1.2(2)	0.7(2)	–	–
460	0.10(4)	0.9(6)	1.2(2)	0.2(2)	–	–
560	0.18(4)	0.9(5)	1.2(2)	0.04(2)	–	–
600	0.18(4)	1.0(5)	–	–	–	–
640	0.18(4)	1.6(4)	–	–	–	–

Table 3.4: Decay times τ_i and amplitudes A_i from the data analysis of transient absorption changes of broadband and single color detection at λ_{probe} = 244 nm after excitation of XMP at 243 nm (2σ error limits of last digits in parentheses). The value of τ_3 was fixed to the decay time found in the fluorescence measurements.

λ_{probe}/nm	τ_1/ps	$A_1/10^{-3}$	τ_2/ps	$A_2/10^{-3}$	τ_3/ps	$A_3/10^{-3}$
244	0.4(3)	3(2)	1.1(2)	−1.8(4)	–	–
325	0.3(2)	−0.6(6)	1.2(2)	1.8(4)	36(–)	0.01(1)
330	0.3(2)	−0.8(6)	1.2(2)	2.1(5)	36(–)	0.03(3)
335	0.3(2)	−1.1(6)	1.2(2)	2.4(6)	36(–)	0.05(5)
400	0.10(4)	1.0(6)	1.2(2)	1.4(2)	–	–
420	0.10(4)	1.8(6)	1.2(2)	1.3(2)	–	–
425	0.10(4)	2.0(6)	1.2(2)	1.1(2)	–	–
460	0.10(4)	1.8(6)	1.2(2)	0.5(2)	–	–
560	0.18(4)	1.3(5)	1.2(2)	0.2(2)	–	–
600	0.18(4)	2.3(5)	1.2(2)	0.1(1)	–	–
640	0.18(4)	1.9(4)	–	–	–	–

a very minor role with low amplitudes in the range of $\ll 5\%$. The value of τ_3 was therefore fixed to the decay time found for the fluorescence decay, where it could be determined with better precision.

The single color detection at $\lambda_{probe} = 244$ nm yielded time profiles that are shown in Figure 3.5 (bottom row), the results of the data analysis are summarized in Tables 3.3 and 3.4 for $\lambda_{pump} = 260$ nm and $\lambda_{pump} = 243$ nm, respectively. The time profiles could not be analyzed unequivocally. This originates from the overlapping of a negative contribution due to the ground state recovery and at least one positive contribution. All of these contributions decay on quite similar time scales, which is reflected in the large margins of error. The decay time of the negative contribution, however, is with ≈ 1 ps consistent with the results of the broadband detection. A longer-lived contribution as was found in the up-conversion results was not necessary for a satisfactory description of the transient absorption time profiles. This might be a result of the very low amplitude of this component. It can therefore safely be concluded that the electronic ground state is almost completely recovered within ≈ 1 ps.

XMP⁻

The electronic dynamics of XMP⁻ were studied after excitation at three pump wavelengths, $\lambda_{pump} = 278$ nm (absorption), $\lambda_{pump} = 260$ nm (fluorescence and absorption) and $\lambda_{pump} = 243$ nm (absorption). Inspecting the static absorption spectra (Fig. 3.2), the S_1 and S_2 states are populated with fractions of 86% and 14% ($\lambda_{pump} = 278$ nm), 9% and 81% ($\lambda_{pump} = 260$ nm) and 0% and 100% ($\lambda_{pump} = 243$ nm), respectively.

The fluorescence lifetime of XMP⁻ in phosphate buffer at pH 7 was measured after excitation at $\lambda_{pump} = 260$ nm at four fluorescence wavelengths from 330 nm $\leqslant \lambda_{fluo} \leqslant$ 480 nm, the respective data sets are shown in Fig. 3.6. The decay times and relative amplitudes found in a data ana-

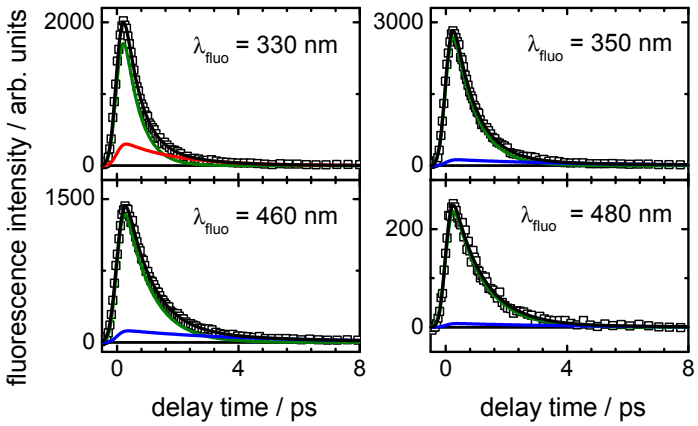

Figure 3.6: Fluorescence time profiles of XMP⁻ after excitation at $\lambda_{pump} = 260$ nm measured at four fluorescence wavelengths from 330 nm $\leqslant \lambda_{fluo} \leqslant$ 480 nm. Open squares represent the data points and black lines the overall fit functions. The single contributions are shown in green ($\tau_{1,fluo}$), red ($\tau_{2,fluo}$), and blue ($\tau_{3,fluo}$).

lysis are summarized in Table 3.5. The lifetime of the major contribution

Table 3.5: Decay times τ_i and relative amplitudes A_i from the data analysis of fluorescence up-conversion measurements after excitation of XMP^- at 260 nm (2σ error limits of last digits in parentheses).

λ_{fluo}/nm	$\tau_{1,fluo}$/ps	$A_{1,fluo}$	$\tau_{2,fluo}$/ps	$A_{2,fluo}$	$\tau_{3,fluo}$/ps	$A_{3,fluo}$
330	0.51(1)	0.82(2)	1.7(5)	0.11(6)	–	–
350	0.73(2)	0.74(2)	–	–	4(1)	0.03(1)
460	0.86(4)	–	–	–	4(1)	0.06(3)
480	1.0(2)	–	–	–	4(1)	0.03(3)

could not be modeled using a fixed value and increased gradually from $\tau_{1,fluo} = 0.51 \pm 0.01$ ps at $\lambda_{fluo} = 330$ nm to 1.0 ± 0.2 ps at $\lambda_{fluo} = 480$ nm. At $\lambda_{fluo} = 330$ nm, an additional contribution decaying with $\tau_{2,fluo} = 1.7 \pm 0.5$ ps was necessary for a satisfactory description of the data. A longer-lived component with a minor amplitude of $\leqslant 6\%$ was observed for all fluorescence time traces at $\lambda_{fluo} \geqslant 350$ nm. The large margin of errors are due to the low amplitudes of this component.

The transient absorption of XMP^- was measured after excitation with three pump wavelengths. The results of the broadband transient absorption experiments of XMP^- are shown in Fig. 3.7. They are similar, though

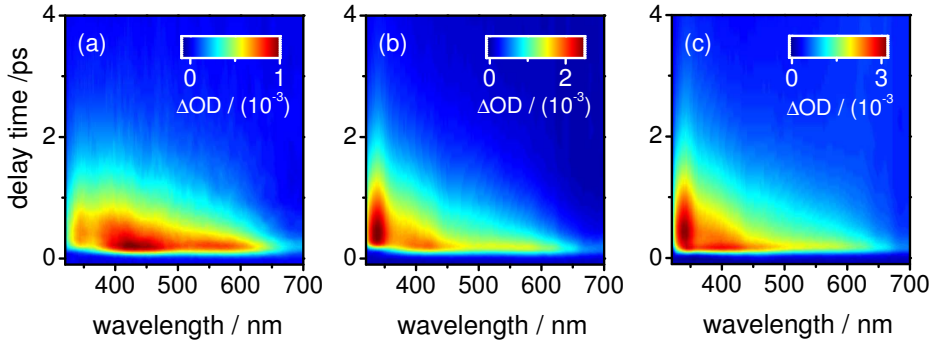

Figure 3.7: Two-dimensional maps of transient absorption changes of XMP^- after excitation with (a) 278 nm, (b) 260 nm, and (c) 243 nm.

not exactly equal, to the results for XMP. For all three pump wavelengths, the two-dimensional maps of transient absorption changes feature three overlapping ESA regions. After excitation mainly to the first $\pi\pi^*$ state at $\lambda_{pump} = 278$ nm, the maxima are at $\lambda_{probe} \approx 340$nm, 440 nm, and 600 nm (Fig. 3.7(a)). After excitation to the second $\pi\pi^*$ state at $\lambda_{pump} = 260$ nm and 243 nm, the maximum of the second ESA band shifts to the blue by ≈ 20 nm to 420 nm (Fig. 3.7(b) and (c)). The two other bands are virtually at the same positions for all three pump wavelengths. The band in the UV range is more pronounced after 260 nm and 243 nm excitation, whereas the relative intensities of the bands in the visible remain virtually unchanged for all three pump wavelengths. All positive bands are attributed to ESA. A

negative contribution, assigned to stimulated emission, leads to a delayed rise of the positive absorption in the UV range. As for XMP, this contribution is more pronounced than in other purine bases.

A global data analysis over the whole broadband detection range for all three pump wavelength was performed and the resulting decay times and amplitudes can be found in Tables 3.6 ($\lambda_{pump} = 278$ nm), 3.7 ($\lambda_{pump} = 260$ nm), and 3.8 ($\lambda_{pump} = 243$ nm). Additionally, the results of the single color detection in the deep UV are given in these Tables. Exemplary time profiles

Table 3.6: Decay times τ_i and amplitudes A_i from the data analysis of transient absorption changes after excitation of XMP^- at 278 nm (2σ error limits of last digits in parentheses). The value of τ_3 was fixed to the decay time found in the fluorescence measurements.

λ_{probe}/nm	τ_1/ps	$A_1/10^{-3}$	τ_2/ps	$A_2/10^{-3}$
242	0.8(2)	1.7(17)	1.3(3)	−2.5(11)
325	0.28(3)	−0.4(4)	0.97(5)	0.8(2)
330	0.28(3)	−0.5(4)	0.97(5)	1.0(2)
335	0.28(3)	−0.6(4)	0.97(5)	1.1(2)
400	0.28(3)	−0.4(4)	0.97(5)	1.3(2)
420	–	–	0.97(5)	1.4(1)
425	–	–	0.97(5)	1.4(1)
460	0.28(3)	0.1(1)	0.97(5)	1.0(2)
560	0.28(3)	0.5(3)	0.97(5)	0.6(2)
600	0.28(3)	0.6(3)	0.97(5)	0.4(2)
640	0.28(3)	0.9(3)	0.97(5)	0.2(2)

for each pump wavelength are depicted in Fig. 3.8. Two decay times were found to be dominating over the whole broadband detection range for all three pump wavelength:

$$\tau_1 = 0.28 \pm 0.03 \text{ ps},$$
$$\tau_2 = 0.97 \pm 0.05 \text{ ps},$$

The sub-picosecond component τ_1 describes the decay of the SE contribution at 325 nm $\leqslant \lambda_{probe} \leqslant$ 400 nm and the fast-decaying positive component at $\lambda_{probe} \geqslant 460$ nm. The contribution with τ_2 was found at all probe wavelengths with positive amplitudes, which decreased with increasing probe wavelength. The component decaying with τ_3 was necessary to model the signals at $\lambda_{pump} = 260$ nm and 243 nm at $\lambda_{probe} \leqslant 460$ nm with amplitudes of $\approx 3 - 10\%$. The value of this decay time was fixed to $\tau_{3,fluo}$, where it could be determined with better precision.

The single-color detection at $\lambda_{probe} = 242$ nm or $\lambda_{probe} = 244$ nm resulted in the time profiles shown in Figure 3.8(bottom row). As was discussed for the results of XMP, the decay behavior was governed by several positive

Table 3.7: Decay times τ_i and amplitudes A_i from the data analysis of transient absorption changes after excitation of XMP^- at 260 nm (2σ error limits of last digits in parentheses). The value of τ_3 was fixed to the decay time found in the fluorescence measurements.

λ_{probe}/nm	τ_1/ps	$A_1/10^{-3}$	τ_2/ps	$A_2/10^{-3}$	τ_3/ps	$A_3/10^{-3}$
244	0.8(2)	6.2(62)	1.3(3)	−8.3(70)	4(−)	−0.4(2)
325	0.28(3)	−1.8(5)	0.97(5)	3.2(4)	4(−)	0.3(2)
330	0.28(3)	−2.0(5)	0.97(5)	3.8(4)	4(−)	0.3(2)
335	0.28(3)	−2.0(5)	0.97(5)	4.0(4)	4(−)	0.4(2)
400	0.28(3)	−0.6(5)	0.97(5)	2.4(4)	4(−)	0.2(2)
420	−	−	0.97(5)	2.4(2)	4(−)	0.2(1)
425	−	−	0.97(5)	2.3(2)	4(−)	0.2(1)
460	0.28(3)	0.1(1)	0.97(5)	1.7(2)	−	−
560	0.28(3)	0.8(4)	0.97(5)	1.0(2)	−	−
600	0.28(3)	1.4(4)	0.97(5)	0.5(2)	−	−
640	0.28(3)	2.0(2)	−	−	−	−

Table 3.8: Decay times τ_i and amplitudes A_i from the data analysis of transient absorption changes after excitation of XMP^- at 243 nm (2σ error limits of last digits in parentheses). The value of τ_3 was fixed to the decay time found in the fluorescence measurements.

λ_{probe}/nm	τ_1/ps	$A_1/10^{-3}$	τ_2/ps	$A_2/10^{-3}$	τ_3/ps	$A_3/10^{-3}$
244	0.8(2)	2.2(22)	1.3(3)	−2.8(24)	4(−)	−0.3(1)
325	0.28(3)	−2.4(6)	0.97(5)	3.4(4)	4(−)	0.4(2)
330	0.28(3)	−3.2(6)	0.97(5)	4.4(5)	4(−)	0.5(2)
335	0.28(3)	−3.5(6)	0.97(5)	5.0(5)	4(−)	0.6(2)
400	0.28(3)	−0.7(6)	0.97(5)	2.8(4)	4(−)	0.4(2)
420	−	−	0.97(5)	2.7(2)	4(−)	0.4(1)
425	−	−	0.97(5)	2.6(2)	4(−)	0.4(1)
460	−	−	0.97(5)	2.0(2)	4(−)	0.2(1)
560	0.28(3)	1.0(4)	0.97(5)	1.2(2)	−	−
600	0.28(3)	2.1(4)	0.97(5)	1.0(2)	−	−
640	0.28(3)	2.3(4)	0.97(5)	0.3(2)	−	−

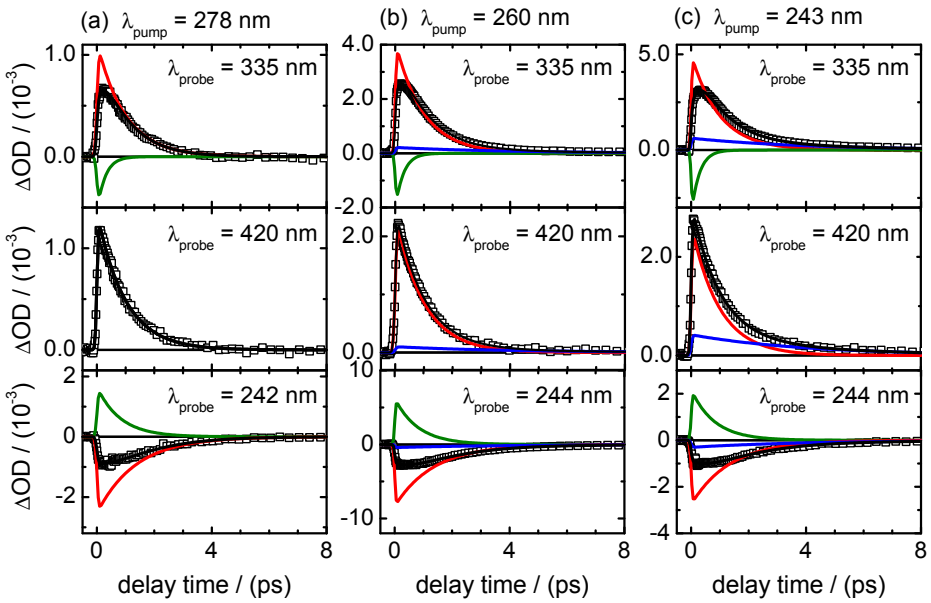

Figure 3.8: Time profiles of transient absorption changes after excitation at (a) $\lambda_{pump} = 278$ nm, (b) 260 nm, and (c) 243 nm. Open squares represent the data points and black lines the overall fit function. The single contributions are shown in green (τ_1), red (τ_2), and blue (τ_3).

and negative components with similar lifetimes around $\tau_2 \approx 1$ ps. However, the time constants of the negative contributions, which describe the ground state recovery, have been determined to $\tau_{2,GSR} = 1.3 \pm 0.4$ ps and $\tau_3 = 4$ ps. The latter contribution accounted for $\approx 5\%$ at $\lambda_{pump} = 260$ nm and $\approx 9\%$ at $\lambda_{pump} = 243$ nm of the negative signal. The values for the relative amplitudes, however, have to be taken with caution regarding the strong correlation and therefore large errors of the respective results from the data analysis.

3.4 DISCUSSION

DISCUSSION OF XMP

The time-resolved experiments of neutral XMP at acidic conditions showed a relaxation to the electronic ground state that can be characterized with two dominating time scales of $\tau_1 \approx 0.2$ ps and $\tau_2 \approx 1$ ps. The virtual absence of significant differences after selective excitation mostly to either the first or second $\pi\pi^*$ state hints at an ultrafast conversion from S_2 to S_1 population that is below the experimental time resolution. However, the sub-picosecond component can be attributed to depopulation of the Franck-Condon region, supposedly of the energetically lower $\pi\pi^*$ state, since it was found to be the dominating decay time of fluorescence close to the excitation wavelengths and the stimulated emission contribution in the transient absorption experiments. The single color detection at 244 nm confirmed that the initially excited state population decays to the electronic ground state within ≈ 1 ps. This short lifetime can be explained by

a rapid and barrierless relaxation in the direction of a conical intersection connecting the excited $\pi\pi^*$ and the electronic ground state. The longer-lived component decaying with $\tau_3 = 36 \pm 8$ ps found in the fluorescence up-conversion results was not necessary for the description of the ground state recovery in the deep UV. This might be due to the fact that the fraction of respective molecules is below the single color detection limit, i.e., $\ll 1\%$. Possible origins of this component will be discussed below in context of the results for XMP^-.

Yamazaki et al. proposed the relaxation coordinate that connects $\pi\pi^*$ and electronic ground state to be the out-of-plane deformation of the five-membered ring.[14] However, the expected substantial energy barrier for this deactivation pathway can be ruled out by the ≈ 1 ps timescale. This might be a result of the replacement of the H atom at the N(9) position by a ribosyl phosphate group. Although this does not seem to have a large impact on the photodynamics of other purine bases, it may be of great importance when the five-membered ring is involved in the relaxation. A comparative study of the free nucleic acid base and the nucleoside would help to shed light on this question, but is difficult regarding the low solubilities of both components in aqueous solution. Gas phase experiments could be an alternative at this point.

The results obtained for the deactivation of XMP in aqueous solution are in quite good agreement with those obtained for the deactivation of methylated xanthine derivatives, where time scales of several 100 fs, ≈ 1 ps and a longer-lived component decaying with $3.5 - 6.3$ ps was found in water and acetonitrile.[28] These were also attributed to a main relaxation via the five-membered ring. The involvement of long-lived optically dark states such as $n\pi^*$ states (a question that was also raised by Chen et al.[28] regarding the deactivation of methylated xanthine derivatives) can be excluded on the basis of the ground state recovery measurements.

DISCUSSION OF XMP^-

The excited-state relaxation of XMP^- present in phosphate buffered H_2O at pH 7 can be described with two dominating time scales of $\tau_1 \approx 0.3$ ps and ≈ 1 ps, which are comparable to the ones found for XMP, and one minor longer-lived contribution decaying with $\tau_3 = 4 \pm 1$ ps. As for neutral XMP, the selective excitation in either of the two $\pi\pi^*$ states seems to have no significant impact on the ensuing dynamics, suggesting a rapid conversion from upper to lower $\pi\pi^*$ state on a timescale that is below the experimental time resolution. However, the gradual increase of fluorescence lifetimes with increasing emission wavelengths after excitation mainly to the second $\pi\pi^*$ state hints at a sizable energy gradient in the emissive state. Additional fluorescence measurements at $\lambda_{pump} \approx 280$ nm would be necessary to gain deeper insight into the excited-state topography of the involved states.

Since the results of the time-resolved experiments for XMP^- are quite similar to those of XMP, the relaxation to the electronic ground state is

expected to occur via similar mechanisms. The components decaying with τ_1 and τ_2 are most likely due to the evolution in the direction of a conical intersection via the out-of-plane deformation of the five-membered ring. The similarity to XMP regarding the decay behavior is not unlikely since the deprotonation takes place at the N(3) position in the six-membered ring. Additionally, the deprotonation might not have a large impact on the electronic structure of the xanthine moiety,[8,12] as it was discussed in the introduction. Interestingly, a different behavior upon deprotonation was observed for the electronic deactivation of hypoxanthine and its nucleoside inosine.[29] Here, deprotonation at the 6-membered ring leads to no significant differences of the excited-state dynamics, although the deactivation pathway occurs via deformation of this ring.[28–30] Deprotonation at the 5-membered ring, on the other hand, leads to drastic increase of fluorescence lifetimes, which was explained by the drastic differences of electronic structures of neutral and both anionic forms.[29]

Besides these effects arising from deprotonation, the protonation of 6-oxopurines is known to have a large impact on the electronic deactivation dynamics of, e.g., monoprotonated hypoxanthine and guanosine. For these species, an increase of lifetimes was found for some part of the excited-state population. This was attributed to the change of the potential energy topography compared to the respective neutral molecule.[29,31]

The longer-lived τ_3 component is possibly due to a fraction of molecules that follow the deactivation pathway via an out-of-plane deformation of the six-membered ring. This is expected to play a dominating role in other purine bases, especially 6-oxopurines,[17–20,22,28,29,31–34] but was not found to be energetically favored in case of xanthine.[14] The decay time of 4 ps and the increase of amplitudes with increasing excitation energy (cf. Tables 3.6, 3.7 and 3.8, and Fig. 3.8) indicate the existence of a small energy barrier that has to be overcome during deactivation. The existence of this contribution is not unreasonable for the anionic species XMP^-, since deprotonation at the N(3) position leads to a slight weakening of force constants for all ring vibrations, as it was shown by Gogia et al. with ultraviolet resonance Raman spectroscopy and DFT calculations.[8]

As for neutral XMP, any significant population of long-lived states can be ruled out on the basis of the ground state recovery measurement in the deep UV.

3.5 CONCLUSIONS

In this work, we investigated the photophysics of xanthosine monophosphate at different protonation states of the xanthine moiety and dependent on the excitation wavelength by means of femtosecond time-resolved transient-absorption and fluorescence up-conversion spectroscopy. Neutral XMP and the deprotonated XMP^- exhibit similar results after excitation to the first $\pi\pi^*$ states. Both species showed relaxation with two dominating time scales in the range of some 100 fs and $\approx$ 1 ps. These have been attributed to a depopulation of the initially populated Franck-

Condon region in the direction of a conical intersection with the electronic state via the out-of-plane deformation of the five-membered ring in the 6-oxopurine moiety. The mechanism was theoretically predicted to be possible for the N(9)H tautomer of xanthine by Yamazaki et al.[14] A minor contribution decaying with several picoseconds was tentatively ascribed to a less favored relaxation pathway exhibiting energy barriers, possibly via the out-of-plane deformation of the six-membered ring, which is energetically not favored in case of xanthine.[14]

BIBLIOGRAPHY

[1] Berg, J. M.; Tymoczko, J. L.; Stryer, L. *Biochemistry*; Freeman: New York, 2010.

[2] Ashihara, H.; Suzuki, T. *Front Biosci.* **2004**, *9*, 1864–1876.

[3] Cavalieri, L. F.; Fox, J. J.; Stone, A.; Chang, N. *J. Am. Chem. Soc.* **1954**, *76*, 1119–1122.

[4] Lichtenberg, D.; Bergmann, F.; Neiman, Z. *J. Chem. Soc. C* **1971**, 1676–1682.

[5] Shukla, M.; Mishra, P. *J. Mol. Struct.* **1994**, *324*, 241–249.

[6] Kulikowska, E.; Kierdaszuk, B.; Shugar, D. *Acta Biochim. Pol.* **2004**, *51(2)*, 493–531.

[7] Callahan, M. P.; Crews, B.; Abo-Riziq, A.; Grace, L.; de Vries, M. S.; Gengeliczki, Z.; Holmes, T. M.; Hill, G. A. *Phys. Chem. Chem. Phys.* **2007**, *9*, 4587–4591.

[8] Gogia, S.; Jain, A.; Puranik, M. *J. Phys. Chem. B* **2009**, *113*, 15101–15118.

[9] Ajò, D.; Fragala, I.; Granozzi, G.; Tondello, E. *Spectrochim. Acta, Part A* **1978**, *34*, 1235–1238.

[10] Dougherty, D.; Younathan, E.; Voll, R.; Abdulnur, S.; McGlynn, S. *J. Electron Spectrosc. Relat. Phenom.* **1978**, *13*, 379–393.

[11] Feyer, V.; Plekan, O.; Richter, R.; Coreno, M.; Prince, K. C. *Chem. Phys.* **2009**, *358*, 33–38.

[12] Plekan, O.; Feyer, V.; Richter, R.; Moise, A.; Coreno, M.; Prince, K. C.; Zaytseva, I. L.; Moskovskaya, T. E.; Soshnikov, D. Y.; Trofimov, A. B. *J. Phys. Chem. A* **2012**, *116*, 5653–5664.

[13] Farrokhpour, H.; Fathi, F. *J. Comput. Chem.* **2011**, *32(11)*, 2479–2491.

[14] Yamazaki, S.; Sobolewski, A. L.; Domcke, W. *Phys. Chem. Chem. Phys.* **2009**, *11*, 10165–10174.

[15] Chen, H.; Lu, S. *J. Chem. Phys.* **2006**, *124*, 154315.

[16] Marian, C. M. *J. Phys. Chem. A* **2007**, *111*, 1545–1553.

[17] Serrano-Andrés, L.; Merchán, M.; Borin, A. C. *J. Am. Chem. Soc.* **2008**, *130*, 2473–2484.

[18] Yamazaki, S.; Domcke, W. *J. Phys. Chem. A* **2008**, *112*, 7090–7098.

[19] Yamazaki, S.; Domcke, W.; Sobolewski, A. L. *J. Phys. Chem. A* **2008**, *112*, 11965–11968.

[20] Lan, Z.; Fabiano, E.; Thiel, W. *Chem. Phys. Chem.* **2009**, *10*, 1225–1229.

[21] Massoud, S. S.; Corfù, N. A.; Griesser, R.; Sigel, H. *Chem.-Eur. J.* **2004**, *10*, 5129–5137.

[22] Röttger, K.; Siewertsen, R.; Temps, F. *Chem. Phys. Lett.* **2012**, *536*, 140–146.

[23] Pancur, T.; Schwalb, N. K.; Renth, F.; Temps, F. *Chem. Phys.* **2005**, *313*, 199–212.

[24] Schwalb, N. K.; Temps, F. *J. Phys. Chem. A* **2009**, *113*, 13113–13123.

[25] LabVIEW 8.6. National Instruments, 2008.

[26] Lorenc, M.; Ziolek, M.; Naskrecki, R.; Karolczak, J.; Kubicki, J.; Maciejewski, A. *Appl. Phys. B: Lasers Opt.* **2002**, *74*, 19–27.

[27] *Mathematica Version 8.0*; Wolfram Research, Inc., 2011.

[28] Chen, J.; Kohler, B. *Phys. Chem. Chem. Phys.* **2012**, *14*, 10677–10682.

[29] Villabona-Monsalve, J. P.; Noria, R.; Matsika, S.; Peón, J. *J. Am. Chem. Soc.* **2012**, *134*, 7820–7829.

[30] Röttger, K.; Siewertsen, R.; Temps, F. *Chem. Phys. Lett.* **2012**, *536*, 140–146.

[31] Karunakaran, V.; Kleinermanns, K.; Improta, R.; Kovalenko, S. A. *J. Am. Chem. Soc.* **2009**, *131*, 5839–5850.

[32] Serrano-Andrés, L.; Merchán, M. *J. Photochem. Photobiol. C* **2009**, *10*, 21–32.

[33] Barbatti, M.; Szymczak, J. J.; Aquino, A. J. A.; Nachtigallová, D.; Lischka, H. *J. Chem. Phys.* **2011**, *134*, 014304.

[34] Heggen, B.; Lan, Z.; Thiel, W. *Phys. Chem. Chem. Phys. 14*, 8137–8146.

4

ULTRAFAST ELECTRONIC DEACTIVATION DYNAMICS OF THE RARE NATURAL NUCLEOBASE HYPOXANTHINE

Katharina Röttger, Ron Siewertsen, Friedrich Temps*

Institut für Physikalische Chemie, Christian-Albrechts-Universität zu Kiel, Olshausenstr. 40, 24098 Kiel, Germany

Reprinted from
Chem. Phys. Lett., *536*, Katharina Röttger, Ron Siewertsen, Friedrich Temps, Ultrafast Electronic Deactivation Dynamics of Hypoxanthine, 140-146, Copyright 2012, with permission from Elsevier.

OWN CONTRIBUTIONS TO THIS MANUSCRIPT:

- Setup of the femtosecond time-resolved transient absorption experiment
- Femtosecond time-resolved transient absorption spectroscopy
- Static spectroscopy
- Analysis of all presented data
- Writing of manuscript

* To whom correspondence should be addressed. E-mail: temps@phc.uni-kiel.de

ABSTRACT

The electronic deactivation of the 6-oxopurine derivative hypoxanthine, its nucleoside inosine and the nucleotide inosine monophosphate have been studied by femtosecond time-resolved spectroscopy after $\pi\pi^*$ photoexcitation at $\lambda = 260$ nm. The development of a highly sensitive parallel broadband (near-UV/VIS) and single-color (deep-UV) transient absorption setup enabled us to monitor the excited-state decay and the ground-state recovery dynamics in one and the same experiment. The measurements revealed similar relaxation behavior, with time constants of $\tau_1 \lesssim 0.1$ ps, $\tau_2 \approx 0.21 \pm 0.08$ ps and $\tau_3 \approx 1.8 \pm 0.4$ ps, for all three investigated molecules. The observed dynamics are assumed to take place through a conical intersection involving an out-of-plane puckering mode of the six-membered ring similar to guanine.

4.1 INTRODUCTION

The four natural DNA bases which form the alphabet of the genomic code of life on Earth stand out for ultrashort excited electronic state lifetimes owing to highly efficient relaxation mechanisms, by which the energy supplied by a UV photon is rapidly dissipated before chemical reactions in the photoexcited state can cause serious molecular damage. The specific deactivation pathways that are responsible for the ensuing high photostability of the molecules have been elucidated in the past years in some detail in a number of laboratories experimentally by means of femtosecond time-resolved spectroscopy[1,2] and theoretically by quantum chemical calculations[3,4]. The subtle differences in the dynamics among the natural DNA bases and their many tautomers and other chemical derivatives (see, e.g.,[3,5–8]) do, however, continue to pose challenging questions.

To gain deeper insight into the correlation between the structural and photochemical properties of the bases, it may be useful to study related molecules like the rare RNA bases. One such rare RNA base for which the electronic deactivation has not yet been reported in the literature to our knowledge is the 6-oxopurine hypoxanthine (Hyp) with its nucleoside inosine (Ino) and nucleotide inosine monophosphate (IMP; Scheme 1).

Scheme 1.

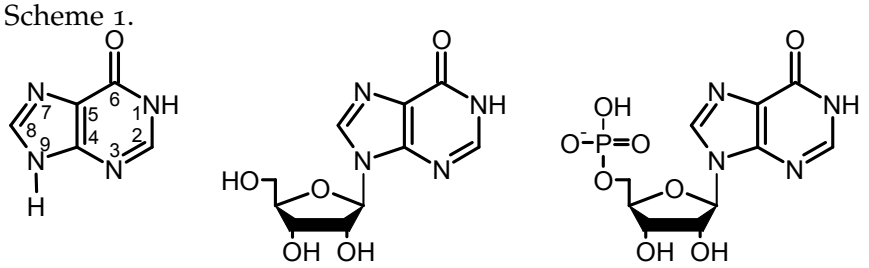

Hyp Ino IMP

Hypoxanthine is an intermediate in the purine metabolism and plays a role as 5′-base of the anticodon in some transfer-RNAs[9]. It is similar to guanine (Gua), but lacks the exocyclic amino group at the C(2) position.

Like other nucleobases, it can exist in a variety of tautomeric forms[10–12]. Under normal conditions at room temperature, only the N(1)H-N(9)H and N(1)H-N(7)H keto tautomers need to be taken into consideration (see Scheme 1 for the numbering scheme), the respective N(3)H and other possible tautomeric structures are significantly higher in energy[11,12]. The N(9)H structure is adopted in the crystal[13], but the N(7)H form appears to predominate in the gas phase[11,14]. In aqueous solution at room temperature and physiological pH, both tautomers coexist in equilibrium[10,11]. Since this tautomerism is blocked by the sugar moiety in Ino and IMP, a comparison of the three molecules should reveal any differences in the photophysical properties between the two Hyp tautomers.

The static UV spectra of Hyp and Ino are given in Figure 4.1. The

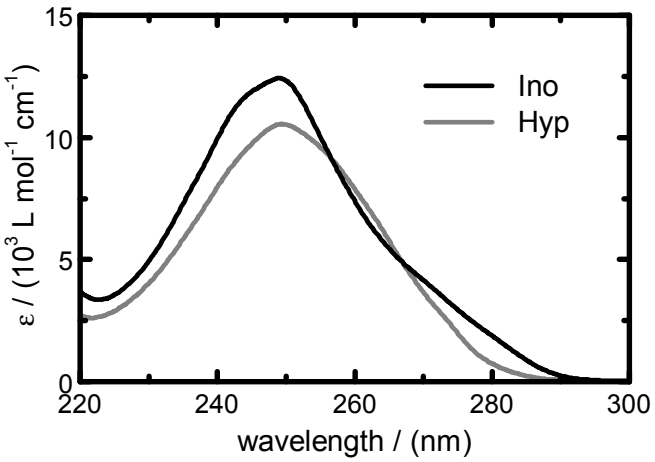

Figure 4.1: Static UV absorption spectra of inosine (Ino) and hypoxanthine (Hyp).

molecules feature a strong absorption maximum at $\lambda \approx 249 - 250$ nm ($\epsilon_{\mathrm{Ino,max}} = 12\,400$ L mol^{-1} cm^{-1}, $\epsilon_{\mathrm{Hyp,max}} = 10\,500$ L mol^{-1} cm^{-1}) with some variations mainly in the wings to the red. The lower peak absorption of Hyp and the differences in the wings are attributed to the fact that its spectrum arises from a superposition of the N(9)H and N(7)H tautomers, whereas Ino consists of a single tautomer. The N(7)H form of Hyp is supposed to have a slightly red-shifted absorption maximum at $\lambda \approx 255$ nm[10], where the absorption by the N(9)H tautomer drops off sharply (see Figure 4.1). However, the precise N(9)H/N(7)H ratio for Hyp in water is not known. The spectrum of IMP in the wavelength range of interest is practically identical to that of Ino. As common for the purines, the observed first UV absorption bands can be assigned to two closely-spaced $\pi\pi^*$ transitions.

The structural similarity of Hyp to Gua suggests that both those purines may follow similar electronic deactivation pathways. To test this hypothesis, we investigated the dynamics of Hyp, Ino and IMP in aqueous solution at pH 7 after photoexcitation at $\lambda = 260$ nm by means of femtosecond time-resolved spectroscopy. Judicious measurements of excited-state fluo-

rescence (ESF) from the prepared optically bright state, transient excited-state absorptions (ESA) and the ground-state recovery (GSR) allowed us the develop a comprehensive picture of the ensuing dynamics. The results reveal deactivation in only $\approx$ 0.2 ps, ranking the observed radiationless electronic transformation among the fastest in the sequence of the natural nucleobases.

4.2 EXPERIMENTAL SECTION

MATERIALS

Hypoxanthine, inosine (both $>$ 99 % purity) and inosine monophosphate ($>$ 98 % purity) were purchased from Sigma-Aldrich and used as supplied. The samples were dissolved in aqueous phosphate buffer at pH 7 in concentrations of $\approx 1.2 - 1.5$ mM, corresponding to an optical density for $\lambda = 260$ nm at 1 mm pathlength of OD ≈ 1.

All time-resolved measurements were performed in stainless steel flow cells ($l = 1$ mm) equipped with 0.2 mm quartz windows and connected by a peristaltic pump to a 250 mL liquid sample reservoir.

FLUORESCENCE UP-CONVERSION MEASUREMENTS

Time-resolved fluorescence measurements were carried out using the up-conversion technique by type I sum frequency generation (SFG) in BBO with the 775 nm gate pulses from the Ti:Sa laser[7]. Very weak fluorescence signals (by comparison with all other nucleobases we have measured so far) were detected in experiments on Ino at $\lambda_{fl} = 320 - 360$ nm. With an experimental time resolution of $\approx$ 140 fs, the measurements allowed us to determine an upper limit for the fluorescence lifetime.

TRANSIENT ABSORPTION MEASUREMENTS

A scheme of the re-designed femtosecond transient absorption spectrometer in our laboratory, which allows for simultaneous broadband ($310 - 700$ nm) and single-color (deep-UV to near-IR) measurements at 1 kHz repetition rate with detection sensitivities of $\Delta OD \leqslant 2 \times 10^{-5}$ (broadband) and $\leqslant 5 \times 10^{-6}$ (single-color, deep-UV), is given in Figure 4.2. The setup was developed in collaboration with Entwicklungsbüro G. Stresing (Berlin).

LASER SOURCE The primary laser source is a regeneratively amplified Ti:Sa laser (CPA 2001, Clark-MXR) delivering $\approx$ 950 mW of average power in pulses of $\approx$ 150 fs duration (fwhm) at $\lambda = 775$ nm and 1 kHz repetition rate. About 500 mW of the laser output are reflected off a beam splitter for the transient absorption experiment, $\approx$ 350 mW of the remaining beam are used for the fluorescence up-conversion spectrometer, $\approx$ 100 mW are left for beam diagnostics and other purposes.

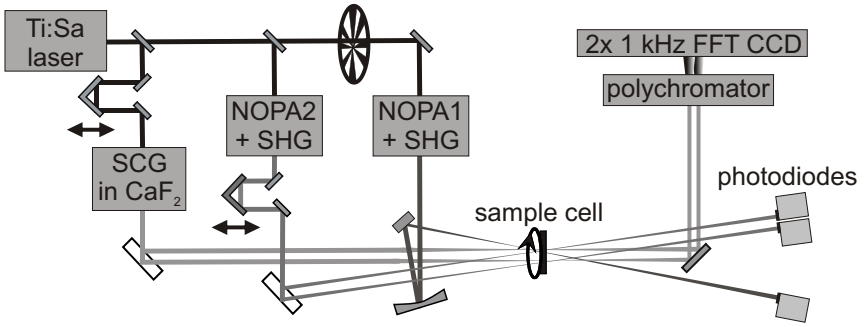

Figure 4.2: Schematic diagram of the femtosecond transient absorption setup for simultaneous UV/VIS broadband and deep-UV single-color measurements.

EXCITATION One half of the Ti:Sa light supplied for the absorption experiment is split off to generate the excitation (pump) pulses in a home-built non-collinear optical parametric amplifier (NOPA #1) equipped with a prism compressor and an 0.2 mm BBO frequency doubling crystal. Every second pump pulse is chopped off to allow for recording background spectra of the probe pulses. The excitation pulses are then focused into the sample cell to a diameter of ≈ 250 μm. Pulse-to-pulse energy fluctuations are monitored by a photodiode (S1227-66BQ, Hamamatsu).

The excitation wavelength in the present experiments was set to $\lambda = 260$ nm. The measured bandwidth was $\Delta\lambda \approx 3$ nm (fwhm), corresponding to ≈ 1.5 times the transform-limit for the $\Delta t \approx 50$ fs pulses (assuming Gaussian shapes). The excitation energies were reduced to < 0.35 μJ/pulse to keep interfering coherent signals resulting from the cell windows and solvent (water) and transient background signals due to multiphoton absorption and ionization of the solvent under control. Under the experimental conditions (e.g., $c_0 = 1.5$ mM, $l = 1$ mm, $\epsilon_{260\,\mathrm{nm}} = 7400$ L mol^{-1} cm^{-1}), the calculated fraction of photoexcited molecules by each pump laser pulse in the irradiated sample volume (≈ 0.05 μL) in the flow cell is about 1.0 %/pulse.

Accumulation of photoproducts was ruled out by exchanging the sample volume in the flow cell between every laser shot. At the 500 Hz effective duty cycle (because every second pump pulse is blocked), the total fraction of laser-excited molecules in the 250 mL solution in the sample reservoir during a 3 h experimental run remained < 1 %.

BROADBAND DETECTION Broadband detection pulses are obtained by supercontinuum generation in CaF_2, for which ≈ 10 % of the Ti:Sa light were reserved. The white-light pulses are split into probe and reference by using the front and back reflections from a thin glass plate and focused to a diameter of ≈ 150 μm into the sample cell, where the probe is overlapped with the pump, while the reference is sent through an unexcited spot. The transmitted probe and reference beams are recollimated, realigned from horizontal to vertical to each other by a 90° periscope, dispersed in a prism spectrograph, and focused onto two full frame transfer

(FFT) back-thinned CCD cameras (S7030-0906, Hamamatsu) with 512×64 pixels (12.3×1.4 mm^2 area). Both camera chips are read out synchronized with the Ti:Sa laser pulses at 1 kHz in FFT mode using a custom-designed controller board (Entwicklungsbüro G. Stresing) connected to a desktop computer (PC) for data acquisition and storage. The 2×512 CCD camera output bins occupy 1024 data channels of the 1200 available channels of the acquisition board. The 176 remaining channels are partly used for trigger and synchronization signals and for the single-color absorption experiment.

SINGLE-COLOR DETECTION The remaining $\approx$ 175 mW of Ti:Sa light generate the wavelength-tunable single-color probe pulses for detection in the deep-UV in a second NOPA (#2) similar to the first one. After attenuation and splitting into probe and reference by taking the reflections from a thin glass plate, both pulses are focused into the sample cell to $\approx$ 150 µm diameter. As before, only the probe spatially overlaps with the pump. The transmitted probe and reference energies are monitored by two matched slow photodiodes (S1227-66BQ, Hamamatsu), which are read out using differential signaling by two preamplifiers to reduce noise due to electromagnetic interference. The photodiode background and peak signals are then transferred to the PC, together with the signals from the photodiode monitoring the excitation pulses, by feeding them by the controller board into the reserved free channels in the data stream.

DATA ACQUISITION AND BACKGROUND SUBTRACTION The experimental data acquisition is controlled by the PC using LabView software. The delay times of the supercontinuum and single-color detection pulses are set using computer-controlled translation stages (M-531.DG and M-511.DG, Physik Instrumente). A shot-by-shot pulse discrimination routine implemented in the LabView software is applied for noise reduction, and pulse-to-pulse fluctuations of the excitation energy are corrected for if desired by signal normalization.

At each delay step in the present experiments, the data were averaged over 15 000 single-pulse measurements (30 s). Coherent artifacts resulting from the sample cell windows and the solvent like cross-phase modulation (XPM,[15–17]), stimulated Raman scattering (SRS), as well as background from multiphoton ionization (MPI) of water and solvated electron absorption (SEA) were taken into account by recording a background transient absorption map for the pure solvent before each sample measurement and subtracting the background from the sample data[15,18]. An appropriate scaling factor for the background allowing for the decrease of multiphoton excitation caused by the sample absorption was determined from the SEA contribution at long times ($10 - 100$ ps), where all interesting transient molecular absorptions had decayed to zero[18].

Absorption-time profiles at selected wavelengths were extracted from the recorded two-dimensional spectro-temporal broadband transient absorption maps for further analysis by non-linear least squares fitting using

MATHEMATICA software[19]. The experimental curves were spectrally averaged over $\Delta\lambda \approx 5$ nm. The width of the instrument response function (IRF) determined by deconvolution was between 90 and 150 fs (Gaussian fwhm, broadband detection), corresponding to an optimal experimental time resolution of $\Delta t \approx 40 - 50$ fs.

Considering the single-color measurements in the deep-UV, the IRF width of ≈ 200 fs should allow for a time resolution of $\Delta t \approx 80 - 100$ fs. However, a rather large coherent peak arising from the quartz windows of the sample cell obscured the initial molecular signal. Although the coherent artifact can be subtracted from the experimental data, the molecular absorption contributions in the first $100 - 200$ fs are effectively lost. The temporal evolution thereafter is not affected.

4.3 RESULTS

TIME-RESOLVED FLUORESCENCE MEASUREMENTS

Time-resolved fluorescence (ESF) measurements carried out on inosine in dilute solution in water provide information on the fate of the optically bright excited states of the molecules. A typical experimental trace is shown in Figure 4.3. Temporal profiles at other fluorescence wavelengths between 320 and 360 nm looked similar. As can be seen, the fluorescence of

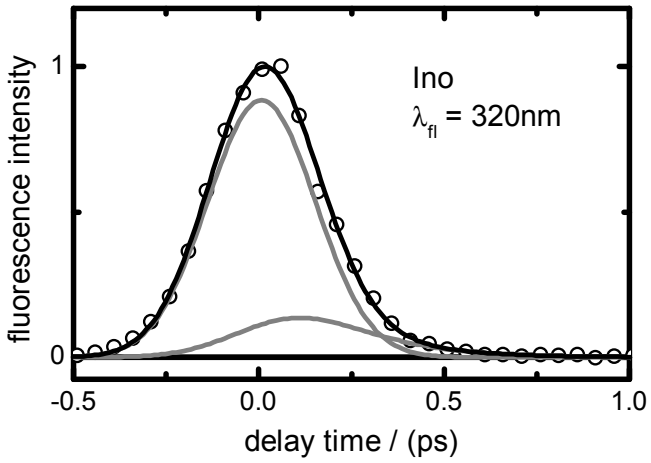

Figure 4.3: Fluorescence-time profiles of Ino at $\lambda_{fl} = 320$ nm after excitation at $\lambda = 260$ nm. Open circles: experimental data, solid black line: best fit to the data curve, gray lines: individual fluorescence decay components.

Ino decays faster than the time resolution of the up-conversion setup. Measurements for Hyp or IMP were therefore omitted. Fits to the data using a sum of two exponentials convoluted with the IRF could determine only an upper limit for the fluorescence lifetime ($\tau_{fl_1} \leqslant 0.1$ ps). The short lifetime hints at an ultrafast departure of the optically prepared wavepacket from the Franck-Condon (FC) region of the $\pi\pi^*$ excited electronic state faster than the experimental time resolution. The added minor ($\approx 10\,\%$) second fluorescence decay component with $\tau_{fl_2} = 0.18 \pm 0.06$ ps improved

the quality of the fit only marginally (cf. Figure 4.3). The value of τ_{fl_2} is comparable with the excited-state lifetime determined by the transient absorption measurements below.

TRANSIENT EXCITED-STATE ABSORPTION MEASUREMENTS

The recorded spectro-temporal absorption maps arising by UV photoexcitation of Hyp, Ino and IMP were found to be virtually identical within experimental errors. The measurements are illustrated in Figure 4.4 by transient spectra for Ino taken at different delay times. The detected very broad

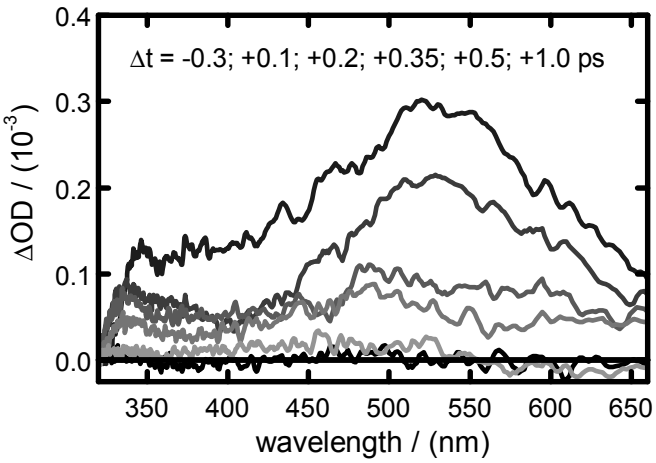

Figure 4.4: Measured transient spectra for Ino after excitation at $\lambda = 260$ nm at different delay times from $\Delta t = -0.3$ ps (black) to +1.0 ps (gray).

ESA can be seen to extend over the entire spectral range from $\lambda \approx 320 - 660$ nm and decay very rapidly in only some few hundred femtoseconds. As for other purines, one may distinguish two overlapping bands, one ranging from $\lambda \approx 320 - 400$ nm and one from $\lambda \approx 400 - 660$ nm, but this distinction is less clear than usually, as the transient features appear to blend within $\Delta t \approx 200 - 300$ fs.

The ensuing dynamics were quantitatively evaluated by least-squares fit analyses of the experimental absorption-time profiles. Two representative data curves for inosine, at $\lambda = 500$ nm and at $\lambda = 340$ nm for the two main ESA regions, together with the respective best-fit curves convoluted with the IRF are displayed in Figure 4.5. The ESA time profile at the first wavelength (Figure 4.5a) is nicely described by a single exponential with lifetime $\tau_2 = 0.23 \pm 0.03$ ps (the fit parameters τ_i are numbered in increasing order) convoluted with the IRF. The data at the second wavelength (Figure 4.5b) require two components for satisfactory fitting. The unresolved fast initial peak (with formal $\tau \lesssim 0.05$ ps) is in part likely an ESA counterpart of the ultrafast ($\tau_{fl_1} \leqslant 0.1$ ps) main fluorescence decay component, but it cannot be ruled out that it may also be an artifact from incomplete subtraction of the XPM and water MPI signal. The slower component (described by a decay constant $\tau_2' = 0.34 \pm 0.08$ ps in this case) is well determined.

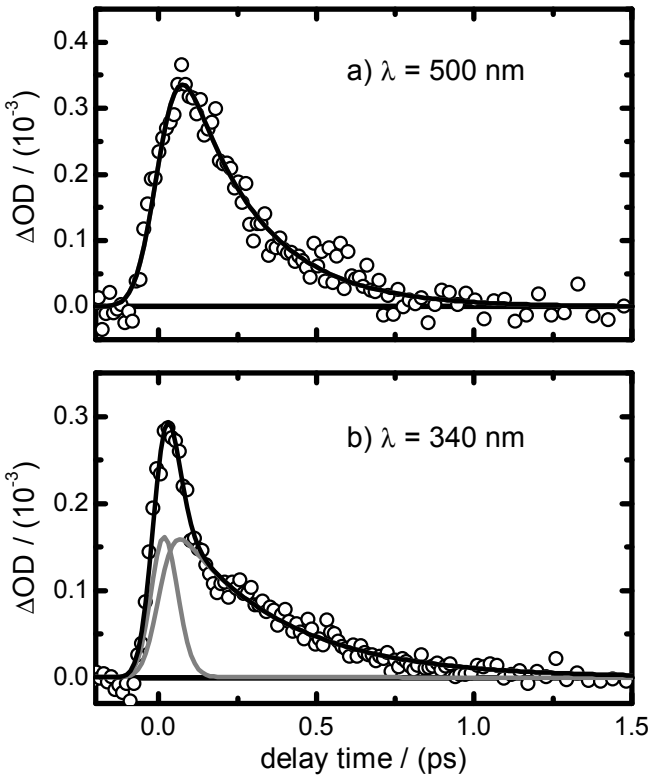

Figure 4.5: Typical absorption-time profiles for Ino ($c_0 = 1.5$ mM) after photoexcitation at $\lambda = 260$ nm at two selected probe wavelengths. Open circles: data points, solid black lines: fitted overall ESA decay curves, gray lines: individual decay components. The small kink at $\Delta t \approx 0.2$ ps in the lower panel is an artifact due to incomplete subtraction of the coherent XPM and water MPI signals.

The results of the subsequent analyses of the ESA time profiles for Hyp, Ino and IMP at 13 probe wavelengths in the experimental range are displayed in Figure 4.6. Taking the average for the three molecules at wave-

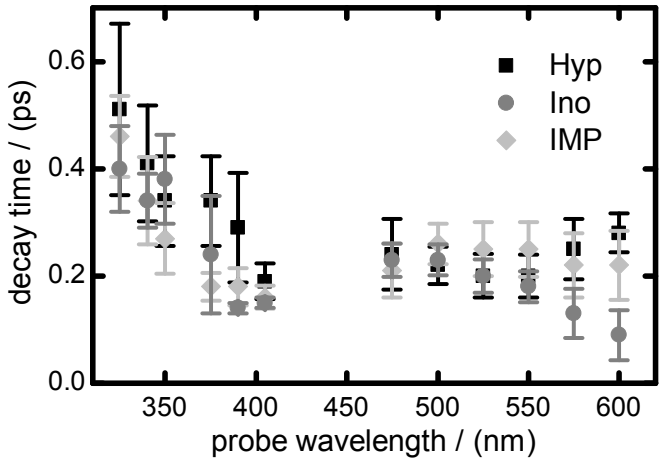

Figure 4.6: Plot of the fitted ESA decay times for Hyp, Ino and IMP vs. probe wavelength.

lengths $\geqslant$ 370 nm yields a mean excited-state lifetime (with 2σ error limits) of

$$\tau_2 = 0.21 \pm 0.08 \text{ ps}.$$

Towards the UV, the fitted transient absorption decay times increase slowly to $\tau_2' \approx 0.46 \pm 0.10$ ps ($\lambda = 325$ nm). At those wavelengths, weak longer-lived contributions due to hot ground state absorption (HGSA, see below) may start to interfere.

GROUND-STATE RECOVERY MEASUREMENTS

The recovery of the population in the electronic ground state by the radiationless relaxation of the excited state was monitored by single-color absorption measurements at selected discrete probe wavelengths in the deep UV. Two representative time profiles for Ino which were taken at $\lambda = 275$ and 242 nm are given in Figure 4.7. At those probe wavelengths, the measurements show a superposition of the transient absorption by the initially vibrationally "hot" (highly internally excited) molecules in the electronic ground state (HGSA) after the ultrafast internal conversion (IC) step and the refilling of the ground-state bleach (GSB) signal by the subsequent vibrational cooling (i.e., the ground-state recovery, GSR) in addition to possible ESA contributions. As noted in Section 4.2, fast initial coherent artifacts arising from the cell windows were subtracted from the data, weak molecular transients in the first $100-200$ fs are therefore lost in these GSR measurements.

At $\lambda = 275$ nm (Figure 4.7a), the molecules are probed at longer wavelength (lower energy) than the applied excitation wavelength (260 nm). The absorption from the S_0 state at this probe wavelength is in the red

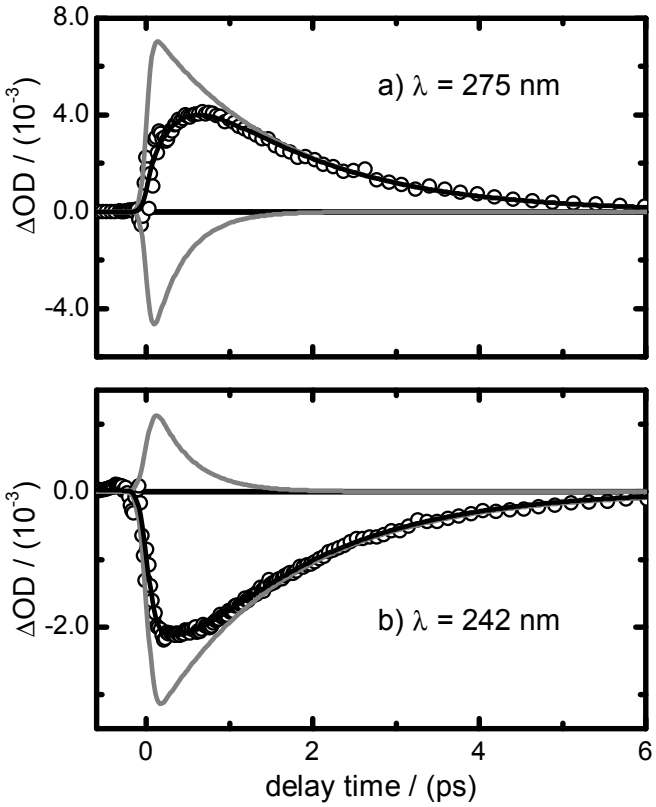

Figure 4.7: Typical absorption-time profiles for Ino at concentrations of $c_0 = 1.0$ mM after photoexcitation at $\lambda = 260$ nm at two discrete UV probe wavelengths together with the respective best-fit curves. The fast initial coherent artifacts from the cell windows have been subtracted from the displayed curves. The absolute absorptions in the two panels cannot be compared due to different focussing conditions and spatial overlaps between the probe and pump beams.

wing of the main band (cf. Figure 4.1), the expected GSB signal (negative ΔOD) is therefore relatively weak. The observed absorption-time profile shows positive ΔOD and is much longer-lived than the ESA in the VIS spectral range. As can be seen, the time profile exhibits an initial rise, which reflects the expected increase of HGSA (and depletion of GSB) and can be modeled using an exponential with rise time $\tau_2' = 0.4 \pm 0.2$ ps with relatively large error margins, and a subsequent slower decay with a well determined time constant of $\tau_3 = 1.6 \pm 0.4$ ps. The rise time is somewhat longer, but comparable in magnitude to the excited-state lifetime τ_2 found above. The observed amplitude of the negative component corresponds well with the estimated GSB amplitude (ΔOD ≈ -0.004) for the calculated fraction of photoexcited molecules ($\approx 0.9\,\%$ for the experiment in Figure 4.7a).

At shorter probe wavelengths relative to the excitation wavelength (e.g., $\lambda = 242$ nm, Figure 4.7b), the measured transients show distinctive ground state bleach (GSB) signals, which are subsequently refilled by slower relaxation processes. The data in Figure 4.7b could be nicely modeled using two exponentials with time constants of $\tau_2' = 0.4 \pm 0.2$ ps and $\tau_3 \approx 1.6 \pm 0.4$ ps, which are identical within experimental errors with those obtained at $\lambda = 275$ nm above. The observed smaller-than-estimated GSB amplitude (ΔOD ≈ -0.003 vs. -0.014) based on the calculated photoexcitation yield is explained by practical experimental difficulties and uncertainties pertaining to the precise beam focus diameters and positions and the effective spatial pump-probe overlap. The faster component (τ_2') is positive and mirrors the excited-state decay via IC, by which the photoexcited molecules return to the ground state. The slower time constant (τ_3) is quite fast for a vibrational cooling process (see Section 4.4). However, analogous measurements for Hyp and IMP gave very similar results. Taking again an average gave a time constant describing the GSR of

$$\tau_3 = 1.8 \pm 0.4 \text{ ps}.$$

4.4 DISCUSSION

The experimental results described in the preceding section provide rather detailed insight into the radiationless electronic relaxation dynamics of the RNA base hypoxanthine and its nucleoside and nucleotide in the $\pi\pi^*$ photoexcited state in solution under near-physiological conditions. Alltogether, the measurements revealed dynamics described by three time constants:

$$\begin{aligned} \tau_1 &\leqslant 0.10 \text{ ps}, \\ \tau_2 &= 0.21 \pm 0.08 \text{ ps}, \\ \tau_3 &= 1.80 \pm 0.40 \text{ ps}. \end{aligned}$$

Little differences were found between the investigated molecules Hyp, Ino and IMP. Thus, it is reasonable to assume that the observed dynamics

are associated with the hypoxanthine chromophore and governed by its distinctive properties, the ribose and phosphate groups do not seem to play large roles in this context. Further, since the free base Hyp itself is present in water in a mixture of the N(9)H and N(7)H tautomeric forms in equilibrium, while Ino and IMP exist in single forms, the results imply that the electronic deactivation dynamics of the two tautomers of Hyp must be similar. The picture for Hyp thus appears to differ from that for adenine (Ade), where the N(9)H tautomer has an excited state lifetime of $\approx$ 0.3 ps, whereas the N(7)H form existing in equilibrium has a lifetime of $\approx$ 8 ps[20].

Judged from the experimental upper limit for the fluorescence lifetime for Ino, the obtained time constant τ_1 refers to the lifetime of the optically bright state of the molecules in the FC region of the excited state. This lifetime is significantly shorter ($\leqslant$ 0.10 ps) than for other nucleobases which we have studied in the past (e.g.,[20,21]). This finding hints at an extraordinarily fast departure of the wavepacket from the FC range, most likely due to a steep potential energy gradient, faster than the time resolution of the up-conversion experiment. The fast initial contribution (with $\tau \lesssim 0.05$ ps) in the transient absorption profiles at $\lambda < 400$ nm (cf. Figure 4.5b) appears to reflect the fluorescence result. Unfortunately, however, the interfering coherent contributions around $\Delta t \approx 0$ do not allow us to elucidate the sub-100 fs dynamics from the transient absorption measurements with more certainty.

Time constant τ_2 is clearly assigned to the lifetime of the excited electronic state with respect to the internal conversion to the S_0 ground state. The fast radiationless electronic deactivation of the excited state described by τ_2 is evident by the decay of the transient excited-state absorption (ESA) signals in the broadband UV/VIS detection range ($\lambda = 320 - 660$ nm) and assumed to proceed through a conical intersection (CI) on a direct and barrierless pathway. The quoted τ_2 value refers to the average for probe wavelengths $\lambda \geqslant 370$ nm (cf. Figure 4.6). At shorter wavelengths, the experimental absorption decay times were found to increase slowly to $\approx$ 0.46 ps ($\lambda = 325$ nm). This is most likely the result of a contributing near-UV absorption by the vibrationally highly excited molecules in the S_0 state after the IC step (i.e., HGSA), with which the ESA in the near-UV would overlap. A slower decay of the ESA bands at shorter probe wavelengths could also arise as consequence of the downhill sliding motion of the wavepacket on the excited-state potential energy surface (PES) en route to the CI. In that case, the "true" excited electronic state lifetime of the molecules would be closer to $\approx 0.4 - 0.5$ ps rather than 0.21 ps. The downhill wavepacket motion should be accompanied by a temporal blue-shift of the ESA. Inspecting the transient spectra shown in Figure 4.4, one can indeed see some evidence for a shift of the broad main absorption maximum in $\Delta t \approx 0.5$ ps from $\lambda \approx 525$ to ≈ 475 nm, but the decreasing signal-to-noise ratio with increasing time delay barely suffices for this conclusion. The fluorescence-time profiles for Ino exhibit a weak component with a lifetime of $\approx$ 0.18 ps, which is consistent with the above ESA decay time of $\tau_2 = 0.21$ ps within

the error limits. After $\Delta t \approx 0.4$ ps, on the other hand, the time profiles at $\lambda = 275$ nm (cf. Figure 4.7a), which are further discussed below, quite clearly demonstrate that the wavepacket has landed on the S_0 PES. Summarizing the experimental observations within the first $\approx 0.2 - 0.4$ ps, the different results thus reflect different stages of the radiationless electronic transition en route from the optically excited state in the FC region via the CI region to the S_0 state.

Last but not least, time constant τ_3 describes the recovery of the initial population in the electronic ground state (GSR) after the molecules have passed the photochemical funnel created by the CI. The dynamics are revealed by the appearance und decay of the HGSA signal measured at $\lambda = 275$ nm and by the recovery of the ground state bleach (GSB) signal measured at $\lambda = 242$ nm (Figure 4.7). Possible ESA contributions to the time profiles at those wavelengths must be small, and should rapidly decay due to the short excited-state lifetime (τ_2). As demonstrated by the data, the molecular absorption levels before the excitation pulse are fully recovered. Thus, since τ_3 describes the final step according to experimental evidence, it defines an overall relaxation time for the excited molecules. Compared with previously investigated other nucleobases, this relaxation time ($\tau_3 = 1.8$ ps) is very short indeed. Considering the underlying physical mechanisms, the radiationless electronic transformation of the photoexcited molecules goes along with the conversion of the entire electronic energy ($\approx 38\,500$ cm^{-1}) to vibrational energy of the molecules in the S_0 state in just ≈ 0.21 ps (τ_2). This huge amount of vibrational energy then has to be dissipated through efficient vibrational relaxation by the surrounding solvent (water). Vibrational relaxation rates in liquids usually depend on the spectral density of the low frequency modes of the solvent and on the coupling between the low frequency modes of the chromophore and the solvent[22,23]. For some photochromic dyes in organic solvents, we have previously found typical vibrational cooling times of $5 - 10$ ps[24,25]. Considering nucleobases in water, however, the strong hydrogen bonding networks promote much faster vibrational relaxation, and even subpicosecond dynamics have been observed[26]. The networks may facilitate transfer of larger quanta of energy. Hence, the value τ_3 is on the fast side, but not unreasonable. Obviously, the absorption measurements in the UV can offer only a glimpse at the vibrational relaxation in the S_0 state. They detect vibrational relaxation only indirectly through the effect on UV band shape and intensity, depend on unknown FC factors among other details and cannot say anything about the involved vibrational modes.

The structural similarity of hypoxanthine to guanine (Gua) suggests that both purine bases follow similar electronic deactivation pathways. A tentative relaxation scheme for Hyp guided by the information for Gua but slightly modified to account for the present experimental results is found in Figure 4.8.

The dynamics of guanosine monophosphate (GMP) in aqueous solution have recently been investigated in some detail[27,28]. The experimental data revealed a barrierless or almost barrierless relaxation pathway connecting

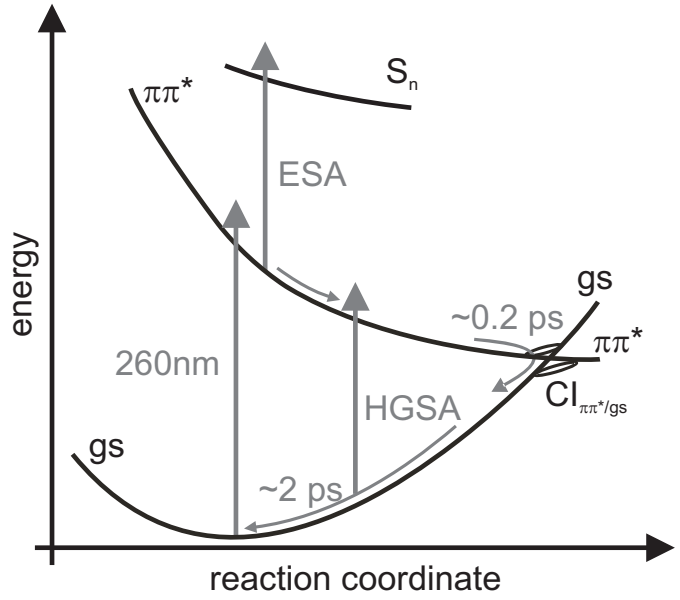

Figure 4.8: Proposed relaxation scheme for Hyp, Ino and IMP in the first excited $\pi\pi^*$ state.

the excited $\pi\pi^*$ (L_a) state via a CI with the electronic ground state. The transient absorption data of Karunakaran et al. are governed by two time constants, $\tau_1 = 0.22$ ps and $\tau_2 = 0.9$ ps[27], which indicates some slower dynamics than in our case. The values were ascribed to a fast relaxation to a shallow minimum or planar region on the PES and to the subsequent internal conversion to the electronic ground state, respectively. The reported vibrational cooling time for GMP is $\tau_3 = 2.5$ ps. The fluorescence measurements of Miannay et al. gave similar results, but required three time constants (0.16, 0.67 and 2.0 ps) for satisfactory fitting[28]. Quantum chemical predictions for Gua[29–35] hint at a relaxation coordinate involving a similar out-of-plane deformation of the six-membered ring as has been found for adenine[36–41], but with a shallow minimum or planar region on the excited PES that slows the wavepacket down before it reaches the CI region.

For Hyp, Ino and IMP, we have observed a significantly faster internal conversion than reported for GMP. This indicates that the PES of Hyp in the excited state does not have a similar minimum or planar region as Gua. Figure 4.8 therefore shows a monotonically decreasing relaxation pathway. It appears that the absence of a larger substituent at the C(2) position of the six-membered ring allows for a faster electronic deactivation, presumably due to a lack of a plateau-like region or negligible energy barrier on the PES en route to the CI region, whereas a substituent like the amino group of Gua hinders the direct motion of the wavepacket towards the CI.

4.5 CONCLUSION

In conclusion, we have presented a study of the photodynamics of the 6-oxopurine hypoxanthine, its nucleoside inosine and its nucleotide inosine monophosphate by means of femtosecond-time resolved absorption and fluorescence spectroscopy. To monitor the excited-state dynamics and the ground-state recovery dynamics, a transient absorption setup has been developed that allows for simultaneous broadband (UV/VIS) and single-color (deep-UV) detections. Applying a shot-by-shot analysis to the recorded signals, the apparatus reaches detection sensitivities of $\Delta OD \leqslant 2 \times 10^{-5}$ (broadband) and $\leqslant 5 \times 10^{-6}$ (single color). The transient absorption measurements revealed similar electronic relaxation behavior for all three investigated molecules, which indicates that the deactivation pathways are specific to the hypoxanthine chromophore. From the observed excited-state absorption decay profiles, the excited $\pi\pi^*$ electronic state has a lifetime of $\tau = 0.21$ ps. Subsequent relaxation of the vibrationally hot S_0 molecules resulting from the radiationless internal conversion leads to a recovery of the ground state with $\tau = 1.8$ ps. The deactivation mechanisms are expected to resemble those of Gua and Ade.

ACKNOWLEDGMENTS

This work has been financially supported by the Deutsche Forschungsgemeinschaft in part under contract Te161/9-1 and in part through SFB 677 "Function by Switching" (subproject A1). We cordially thank Rongrong Zhang for her assistance with the time-resolved absorption measurements.

BIBLIOGRAPHY

[1] Crespo-Hernández, C. E.; Cohen, B.; Hare, P. M.; Kohler, B. *Chem. Rev.* **2004**, *104*, 1977–2019.

[2] Middleton, C. T.; de La Harpe, K.; Su, C.; Law, Y. K.; Crespo-Hernández, C. E.; Kohler, B. *Annu. Rev. Phys. Chem.* **2009**, *60*, 217–239.

[3] Serrano-Andrés, L.; Merchán, M. *J. Photochem. Photobiol. C* **2009**, *10*, 21–32.

[4] Barbatti, M.; Aquino, A. J. A.; Szymczak, J. J.; Nachtigallová, D.; Hobza, P.; Lischka, H. *Proc. Natl. Acad. Sci. U.S.A.* **2010**, *107*, 21453–21458.

[5] Malone, R. J.; Miller, A. M.; Kohler, B. *Photochem. Photobiol.* **2003**, *77*, 158.

[6] Hare, P. M.; Crespo-Hernández, C. E.; Kohler, B. *Proc. Natl. Acad. Sci. U.S.A.* **2007**, *104*, 435–440.

[7] Schwalb, N. K.; Temps, F. *J. Phys. Chem. A* **2009**, *113*, 13113–13123.

[8] Kistler, K. A.; Matsika, S. *J. Phys. Chem. A* **2007**, *111*, 8708–8716.

[9] Berg, J. M.; Tymoczko, J. L.; Stryer, L. *Biochemistry*; Freeman: New York, 2010.

[10] Lichtenberg, D.; Bergmann, F.; Neiman, Z. *Isr. J. Chem.* **1972**, *10*, 805–17.

[11] Fernández-Quejo, M.; de la Fuente, M.; Navarro, R. *J. Mol. Struct.* **2005**, *744-747*, 749–757.

[12] Gogia, S.; Jain, A.; Puranik, M. *J. Phys. Chem. B* **2009**, *113*, 15101–15118.

[13] Schmalle, H. W.; Hänggi, G.; Dubler, E. *Acta Cristallogr. C* **1988**, *44*, 732.

[14] Lin, J.; Yu, C.; Peng, S.; Akiyama, I.; Li, K.; Lee, L. K.; LeBreton, P. R. *J. Phys. Chem.* **1988**, *84*, 1006–1012.

[15] Lorenc, M.; Ziolek, M.; Naskrecki, R.; Karolczak, J.; Kubicki, J.; Maciejewski, A. *Appl. Phys. B: Lasers Opt.* **2002**, *74*, 19–27.

[16] Dobryakov, A. L.; Kovalenko, S. A.; Ernsting, N. P. *J. Chem. Phys.* **2003**, *119*, 988–1002.

[17] Dobryakov, A. L.; Kovalenko, S. A.; Ernsting, N. P. *J. Chem. Phys.* **2005**, *123*, 044502.

[18] Cohen, B.; Hare, P. M.; Kohler, B. *J. Am. Chem. Soc.* **2003**, *125*, 13594.

[19] *Mathematica Version 8.0*; Wolfram Research, Inc., 2011.

[20] Pancur, T.; Schwalb, N. K.; Renth, F.; Temps, F. *Chem. Phys.* **2005**, *313*, 199–212.

[21] Schwalb, N. K.; Temps, F. *J. Phys. Chem. B* **2009**, *113*, 16365–16376.

[22] Elsaesser, T.; Kaiser, W. *Annu. Rev. Phys. Chem.* **1991**, *42*, 83–107.

[23] Owrutsky, J. C.; Raftery, R.; Hochstrasser, R. M. *Annu. Rev. Phys. Chem.* **1994**, *45*, 519–555.

[24] Siewertsen, R.; Schönborn, J. B.; Hartke, B.; Renth, F.; Temps, F. *Phys. Chem. Chem. Phys.* **2011**, *13*, 1054–1063.

[25] Siewertsen, R.; Strübe, F.; Mattay, J.; Renth, F.; Temps, F. *Phys. Chem. Chem. Phys.* **2011**, *13*, 3800–3808.

[26] Yang, M.; Szyc, L.; Röttger, K.; Fidder, H.; Nibbering, E. T. J.; Elsaesser, T.; Temps, F. *J. Phys. Chem. B* **2011**, *115*, 5484–5492.

[27] Karunakaran, V.; Kleinermanns, K.; Improta, R.; Kovalenko, S. A. *J. Am. Chem. Soc.* **2009**, *131*, 5839–5850.

[28] Miannay, F.-A.; Gustavsson, T.; Banyasz, A.; Markovitsi, D. *J. Phys. Chem. A* **2010**, *114*, 3256–3263.

[29] Chen, H.; Lu, S. *J. Chem. Phys.* **2006**, *124*, 154315.

[30] Marian, C. M. *J. Phys. Chem. A* **2007**, *111*, 1545.

[31] Yamazaki, S.; Domcke, W. *J. Phys. Chem. A* **2008**, *112*, 7090–7098.

[32] Yamazaki, S.; Domcke, W.; Sobolewski, A. L. *J. Phys. Chem. A* **2008**, *112*, 11965–11968.

[33] Serrano-Andrés, L.; Merchán, M.; Borin, A. C. *J. Am. Chem. Soc.* **2008**, *130*, 2473–2484.

[34] Lan, Z.; Fabiano, E.; Thiel, W. *ChemPhysChem* **2009**, *10*, 1225–1229.

[35] Barbatti, M.; Szymczak, J. J.; Aquino, A. J. A.; Nachtigallová, D.; Lischka, H. *J. Chem. Phys.* **2011**, *134*, 014304.

[36] Perun, S.; Sobolewski, A. L.; Domcke, W. *Chem. Phys.* **2005**, *313*, 107–112.

[37] Perun, S.; Sobolewski, A. L.; Domcke, W. *J. Am. Chem. Soc.* **2005**, *127*, 6257–6265.

[38] Marian, C. M. *J. Chem. Phys.* **2005**, *122*, 104314.

[39] Serrano-Andrés, L.; Merchán, M.; Borin, A. C. *Chem. Eur. J.* **2006**, *12*, 6559–6571.

[40] Barbatti, M.; Lischka, H. *J. Am. Chem. Soc.* **2008**, *130*, 6831.

[41] Hassan, W. M. I.; Chung, W. C.; Shimakura, N.; Koseki, S.; Kono, H.; Fujimura, Y. *Phys. Chem. Chem. Phys.* **2010**, *12*, 5317–5328.

5

ULTRAFAST ELECTRONIC DEACTIVATION DYNAMICS OF THE INOSINE DIMER - A MODEL CASE FOR H-BONDED PURINE BASES

Katharina Röttger,[a] Frank D. Sönnichsen,[b] Friedrich Temps[a]*

[a] Institut für Physikalische Chemie, Christian-Albrechts-Universität zu Kiel, Olshausenstr. 40, 24098 Kiel, Germany.

[b] Otto Diels-Institut für Organische Chemie, Christian-Albrechts-Universität zu Kiel, Otto-Hahn-Platz 4, 24118 Kiel, Germany.

K. Röttger, F. D. Sönnichsen, F. Temps, *Photochem. Photobiol. Sci.*, **2013**, DOI: 10.1039/c3pp50093d.

OWN CONTRIBUTIONS TO THIS MANUSCRIPT:

- Femtosecond time-resolved transient absorption spectroscopy
- Static IR and UV/vis spectroscopy
- Analysis of all presented data
- Writing of manuscript

* To whom correspondence should be addressed. E-mail: temps@phc.uni-kiel.de

ABSTRACT

The structural properties and ultrafast electronic deactivation dynamics of the inosine dimer in $CHCl_3$ have been investigated by two-dimensional ^1H NMR and static FTIR spectroscopy and by femtosecond time-resolved transient absorption spectroscopy, respectively. The ^1H NMR and IR spectra show the formation of a well-defined, symmetric dimer with an association equilibrium constant of $K_{I.I} = 690 \pm 100\ M^{-1}$. The excited-state dynamics after photoexcitation at $\lambda_{pump} = 260$ nm monitored by ultrafast absorption spectroscopy show great similarity with those of the monomer inosine in aqueous solution and are governed by a decay time of $\tau = 90 \pm 10$ fs, which is one of the shortest electronic lifetime of all nucleobases and nucleobase dimers studied so far. On the basis of these observations, the inosine dimer is expected to follow a similar relaxation pathway as the monomer, involving an out-of-plane deformation of the six-membered ring. The importance of the C(2) position for the electronic deactivation of hypoxanthine and guanine is discussed. The straightforward results obtained for the inosine dimer qualifies it as an excellent test case for more complicated systems such as the G·C and the A·T base pairs.

5.1 INTRODUCTION

The structure and excited electronic state dynamics of the dimer of the rare nucleoside hypoxanthine (Hyp) is of special interest for two reasons: First, the conversion of adenine to hypoxanthine in DNA may lead to a mutation of an A·T to a G·C base pair[1,2] since Hyp strongly favours base pairing with cytidine (C) compared to thymine (T), adenine (A) or guanine (G) and consequently pairs with C during DNA replication process.[1,3–9] The conversion of A to Hyp can occur via spontaneous hydrolytic deamination[10] or under oxidative stress, for example induced by cigarette smoke.[11,12] Recently, a defective purine nucleotide metabolism was found to be another reason for the incorporation of Hyp into DNA.[13] Related repair mechanisms regarding these mutations have been reviewed by Kow[7] and Ohtsuka.[14] Furthermore, the duplex stability may be reduced upon incorporation of Hyp.[4,15–17] Deeper insight into the dynamics of H-bonded base pairs containing hypoxanthine might help shed light on the relevant mechanisms at a molecular level.

A second reason for interest in the dynamics of the hypoxanthine dimer lies in the close structural similarity of hypoxanthine and guanine. The investigation of the excited-state dynamics of Hyp has recently been used to explore the influence of the exocyclic amino group on the electronic deactivation of G.[18–20] The results showed a strong acceleration of the excited-state dynamics in Hyp compared to G, which was attributed to an unrestrained, direct decay to the S_0 ground state via the out-of-plane deformation of the six-membered ring involving the C(2) atom in the absence of the amino group.

In this study, the focus is on the influence of hydrogen bonding on the electronic deactivation of purine nucleobases. The hypoxanthine dimer is a useful tool in a systematic investigation of this question because it forms a stable, well-defined dimer in aprotic solvents as is shown in Fig. 5.1. This dimer is accessible for static and time-resolved measurements in a

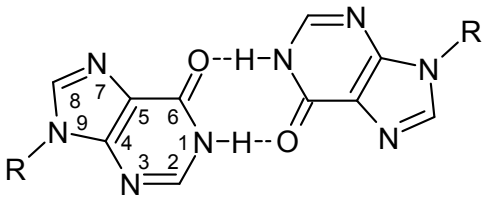

Figure 5.1: Structure of the inosine dimer in $CHCl_3$. R is a 2′,3′,5′-TBDMS protected ribosyl residue.

solution of the 2′,3′,5′-TBDMS-protected nucleoside inosine (referred to in the following as $I(TBDMS)_3$, or simply as inosine or I where obvious from the context) in aprotic solvents such as chloroform, where the formation of H-bonded species is favoured. The relative simplicity of the I·I dimer thus qualifies it as excellent reference for comparison with the electronic deactivation mechanism in the G·C dimer, which is still controversially discussed.[21–29]

In the following, the structure of the I·I dimer is determined by NMR and FTIR spectroscopy. The association equilibrium constant $K_{I\cdot I}$ is derived by an analysis of the concentration dependence of the IR bands. The electronic deactivation dynamics are investigated using femtosecond time-resolved transient absorption spectroscopy. The results are discussed in context of the dynamics of the monomer and other H-bonded complexes.

5.2 EXPERIMENTAL SECTION

MATERIALS AND STATIC SPECTRA

2′,3′,5′-O-(*tert*-Butyldimethylsilyl)-inosine was synthesized by following the protocols of Ogilvie[30] and Hupp et al.[31] Anhydrous $CHCl_3$ stabilized with amylene was purchased from Sigma-Aldrich and dried over molecular sieves to remove residual water. All solutions were prepared in a box purged with dry air to avoid exposure to atmospheric water vapour as well as possible. The solvent and sample purity were checked with NMR, FTIR and UV/VIS absorption spectroscopy. Two-dimensional (2D) NMR spectra of the $I(TBDMS)_3$ solutions were taken in $CDCl_3$ on a Bruker AV-600 spectrometer, and temperature-dependent one-dimensional (1D) ^{1}H NMR spectra were recorded on a Bruker AV-200 spectrometer.

The association equilibrium of I in $CHCl_3$ was investigated as described previously.[25,27] FTIR spectra were taken in the concentration range 2 mM $\leqslant c_0 \leqslant$ 40 mM (with c_0 being the initial inosine concentration) on a Bruker IFS 66v spectrometer purged with N_2 using dry $CHCl_3$ as the background.

UV/VIS absorption spectra were taken on a Shimadzu UV-2401 desktop spectrometer at room temperature.

TRANSIENT ABSORPTION MEASUREMENTS

Femtosecond time-resolved measurements were performed with a transient absorption spectrometer for simultaneous single-colour and broadband detection.[18] The samples were excited by laser pulses at $\lambda_{pump} = 260$ nm generated in a home-built non-collinear optical parametric amplifier (NOPA). Single-colour detection was performed with pulses at $\lambda_{probe} = 244$ nm from a second NOPA, which were split into probe and reference pulses and detected with a pair of matched photodiodes. Broadband probe pulses were generated via supercontinuum generation in CaF_2, separated again into probe and reference and detected with two FFT-CCD cameras.

The sample solutions were pumped through a flow cell for all transient absorption measurements to avoid accumulation of photoproducts. The background signal induced by cross-phase modulation and multi-photon absorption of $CHCl_3$ was kept as low as possible by working at an optical pathlength of 0.1 mm. The initial inosine concentrations were adjusted to values of $c_0 = 2.8$ mM and $c_0 = 14$ mM, corresponding to optical densities at $\lambda = 260$ nm of OD = 0.2 and 1.0, respectively, as approximate upper and lower limits for the experiments. All measurements were repeated three times. The time resolutions were of the order of $\Delta t \approx 40$ fs (broadband measurements at $\lambda_{probe} = 320 - 700$ nm) and $\Delta t \approx 80$ fs (single-colour measurements at $\lambda_{probe} = 244$ nm).

RESULTS

STRUCTURAL CHARACTERISATION

The structural characterisation of the $I(TBDMS)_3$ aggregates in $CHCl_3$ was carried out via NMR spectroscopy. 2D NOESY and COSY spectra measured at room temperature were used to check the geometry and connectivity of the inosine dimer. 1D ^1H NMR spectra were recorded in the temperature range $210\ K \leqslant T \leqslant 300\ K$ at an initial concentration of $c_0 = 10$ mM. The results agree with those obtained by Hupp et al.[31] for inosine in a $CDClF_2/CDF_3$ mixture at 123 K and confirm the symmetric dimer structure given in Fig. 5.1.

The association equilibrium was investigated by FTIR spectroscopy. A typical IR spectrum of $I(TBDMS)_3$ at $c_0 = 10$ mM in $CHCl_3$ is shown in Fig. 5.2. Based on the observed concentration dependence, the slightly asymmetric band at 3385 cm^{-1} is immediately attributed to the N–H stretching mode of the imino group in the monomer. On the other hand, the broad feature at $\omega \leqslant 3400\ cm^{-1}$ originates from the N–H$\cdots$O stretching mode of the dimer, overlaid with Fermi resonances and couplings with lower-frequency modes, as has been discussed earlier for other H-bonded nucleobase dimers.[27,32,33] The intensities of the observed IR bands are roughly

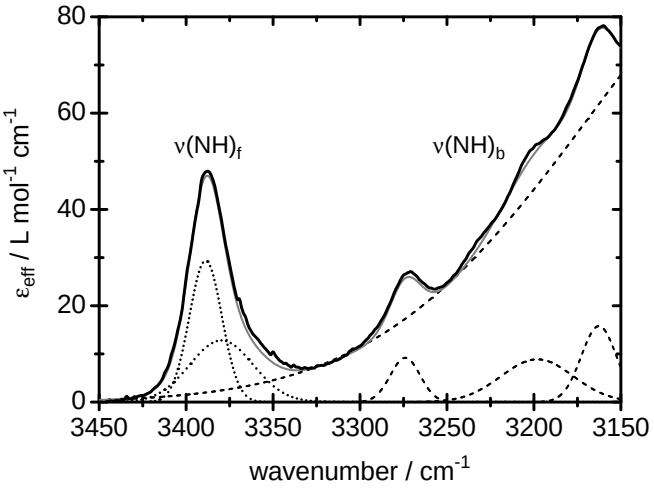

Figure 5.2: FTIR spectrum of $I(TBDMS)_3$ in $CHCl_3$ measured at an initial concentration of $c_0 = 10$ mM. Dotted curves indicate the contributions of the monomeric inosine molecules, and dashed curves indicate dimer bands. The thin solid grey line represents the overall fit that was used for the determination of the degree of association β.

three times lower compared to other aggregates such as G·C in $CHCl_3$, since inosine possesses no NH_2 group. This and the limited solubility of $I(TBDMS)_3$ reduced the concentration range for reliable IR measurements to $2\ \text{mM} \leqslant c_0 \leqslant 40\ \text{mM}$.

For a global data analysis, the sums of Gaussian shaped bands (cf. Fig. 5.2) were used for the description of the monomer and dimer contributions to the spectra $\epsilon_M(\omega)$ and $\epsilon_D(\omega)$, respectively.[27] These two spectral functions were globally fitted to all spectra using the overall model function

$$\epsilon_{\text{eff}}(\omega) = (1-\beta)\epsilon_M(\omega) + (\beta/2)\epsilon_D(\omega)$$

with the degree of association

$$\beta = \frac{c_0 - c_M}{c_0} = \frac{2\,c_D}{c_0},$$

where c_M and c_D, respectively, denote the actual monomer and dimer concentrations ($c_M + 2c_D = c_0$). All fit parameters describing the contributing IR bands were free-floating. The plot of β versus $\log c_0$ is shown in Fig. 5.3. The association equilibrium constant $K_{I\cdot I}$ at $T = 298$ K was then derived via the relation

$$K_{I\cdot I} = \frac{c_D}{(c_M)^2} = \frac{\beta}{2c_0(1-\beta)^2},$$

which gave a value of

$$K_{I\cdot I} = 690 \pm 100\ \text{M}^{-1}.$$

The static UV/VIS absorption spectra of inosine in $CHCl_3$ and in buffered aqueous solution at pH 7 are given in Fig. 5.4. They consist of two strongly

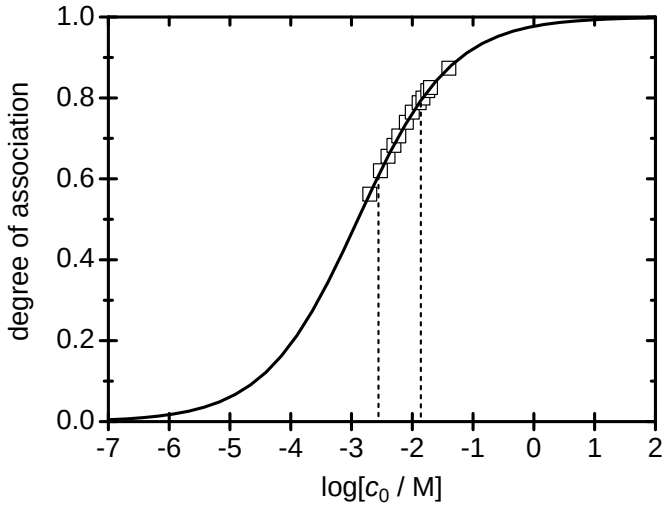

Figure 5.3: Degrees of association β vs. $\log(c_0)$ for the inosine dimer in $CHCl_3$ from the global fitting of the FTIR spectra in the concentration range 2 mM $\leqslant c_0 \leqslant$ 40 mM. The dashed vertical lines indicate the two concentrations used in the time-resolved transient absorption measurements.

overlapping absorption bands attributed to the two energetically nearly degenerate $\pi\pi^*$ transitions that are known to be existent in the purine bases and have been calculated for hypoxanthine and inosine.[20] Compared to the spectrum in water at pH 7, the energetically higher $\pi\pi^*$ band around $\lambda = 250$ nm exhibits a slightly more pronounced structure near the maximum in $CHCl_3$, while the band around $\lambda = 275$ nm is slightly red-shifted.

TRANSIENT ABSORPTION MEASUREMENTS

The results of the broadband transient absorption measurements after photoexcitation at $\lambda_{pump} = 260$ nm are depicted in Fig. 5.5 as two-dimensional maps of the transient absorption changes (ΔOD) as function of wavelength and time delay. The data were taken at inosine concentrations of $c_0 = 2.8$ and 14 mM, corresponding to $\beta \approx 0.60$ and 0.80, respectively. Both maps show essentially the same spectro-temporal behaviour: the broad excited-state absorption (ESA) in the visible spectrum features no obvious maximum, is strongly overlapping with the band in the UV, and decays within < 200 fs. The more intense absorption in the UV exhibits a maximum at $\lambda \approx 370$ nm and decays within the first picosecond, during which a slight blue-shift of the maximum is visible. This can also be seen in Fig. 5.6, which displays transient spectra for both concentrations at two delay times.

The temporal dynamics given in the 2D absorption maps were evaluated by a non-linear least squares fitting analysis of the absorption-time profiles at both experimental concentrations. Exemplary data curves at two selected probe wavelengths, $\lambda_{probe} = 500$ nm and 370 nm, together with the respective best-fit curves are given in Fig. 5.7. As illustrated exemplarily for $\lambda_{probe} = 500$ nm, all time profiles in the wavelength range 700 nm $\leqslant \lambda_{probe} \leqslant$ 430 nm could be nicely modeled using a single exponen-

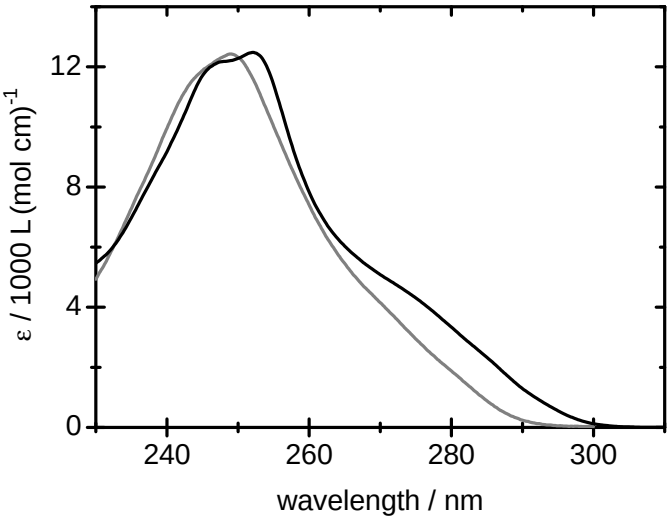

Figure 5.4: Static UV/VIS absorption spectra of I(TBDMS)$_3$ in $CHCl_3$ (black) and I in water at pH 7 (grey).

tial decay function. Towards shorter wavelengths (e.g. $\lambda_{probe} = 370$ nm), a minor additional second component with a slower decay time had to be taken into account. Taking the experimental data at ten selected wavelengths distributed over the probe spectrum, a global evaluation subsequently yielded an ultrashort lifetime of

$$\tau_1 = 90 \pm 10 \text{ fs}$$

determining the ESA decay dynamics across the entire probe wavelength spectrum. The minor second decay component at near-UV probe wavelengths was accounted for by time constant values from $\tau_2 = 0.20 \pm 0.09$ ps at $\lambda_{probe} = 420$ nm increasing to $\tau_2 = 0.58 \pm 0.04$ ps at $\lambda_{probe} = 340$ nm. Importantly, the results showed that there is no significant difference between the dynamics at the two experimental concentrations. The observed behaviour will be discussed below.

The single-colour measurement at $\lambda_{probe} = 244$ nm yielded time profiles, shown in Fig. 5.7, which reflect the time scale for vibrational cooling of the 'hot' S_0 molecules returned to the electronic ground state. The obtained ground-state recovery time found for both concentrations is identical and with $\tau_3 = 9.4 \pm 1.0$ ps much slower than the above excited-state depopulation time.

5.3 DISCUSSION

The combined experimental results concerning the structural characterisation and the time-resolved transient absorption measurements described in the preceding section provide a firm basis for the discussion of the excited-state dynamics of the H-bonded inosine dimer in $CHCl_3$.

First, the combination of ^{1}H NMR spectroscopy on the basis of the investigation of Hupp et al.[31] and IR absorption spectroscopy revealed a simple and symmetric structure for the investigated dimer (cf. Fig. 5.1).

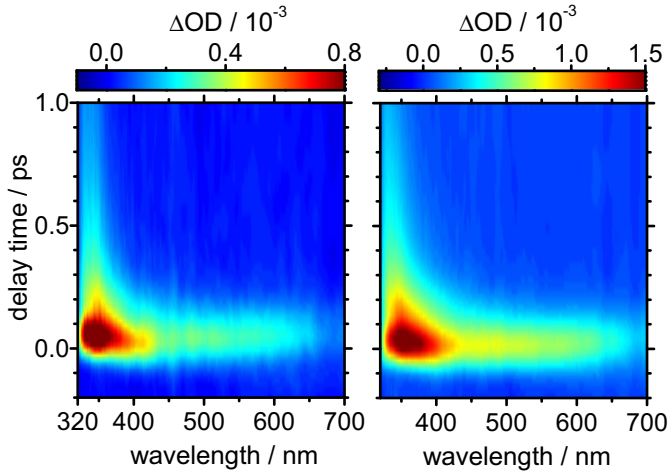

Figure 5.5: Two-dimensional maps of the transient absorption changes ΔOD after excitation of $I(TBDMS)_3$ in $CHCl_3$ at concentrations of $c_0 = 2.8$ mM (left) and $c_0 = 14$ mM (right), corresponding to β values of 0.60 and 0.80, respectively.

The recorded NMR data for I in $CHCl_3$ as a solvent were in full agreement with the reported ones[31] in CD_2Cl_2. It is emphasized that the observed well-determined structure distinguishes the inosine dimer from other H-bonded nucleoside dimers such as G·G or A·A, which may coexist in a variety of intensely debated isomeric forms and may also easily form even larger aggregates.[27,32–36] The association constant of $K_{I\cdot I} = 690 \pm 100\ M^{-1}$ in $CHCl_3$ from the present FTIR spectra is of comparable magnitude to the estimated value of 400 M^{-1} of Kyogoku et al. for 2,3-benzylidine-5′-trityl-inosine in $CHCl_3$.[3] The association constant of $200 \pm 10\ M^{-1}$ in CD_2Cl_2[31] is also in reasonable agreement, since the latter solvent is more polar with a dipole moment of 1.6 D compared to 1.01 D for $CHCl_3$.[37] A similar behaviour has already been observed for the increasing self-aggregation of cytidine with decreasing solvent polarity in $CHCl_3$, CCl_4 and *n*-hexane.[38]

Second, the femtosecond time-resolved broadband absorption maps feature two spectral characteristics, a broad and unstructured band in the visible range and a distinct band in the UV. In a previous study,[18] we investigated the molecular dynamics of hypoxanthine and inosine monomers in buffered aqueous solution after excitation at $\lambda_{pump} = 260$ nm. The transient spectra in $CHCl_3$ are quite similar to those found for inosine in H_2O. A difference is the enhancement of the transient absorption band in the UV. A similar behaviour, though not as pronounced as for inosine, was found for other H-bonded purine base aggregates in solvents like $CHCl_3$ and *n*-hexane.[28,36,39]

The analysis of the transient absorption data yielded an ESA decay time of

$$\tau_1 = 90 \pm 10 \text{ fs}$$

at all probe wavelengths. In the VIS region, in fact, the absorption-time profiles showed single-exponential behaviour with τ_1 as sole relevant de-

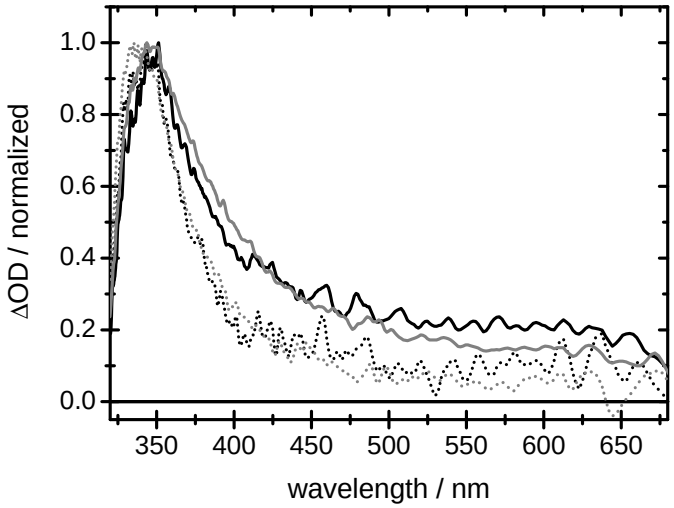

Figure 5.6: Normalized transient ESA spectra at two selected delay times for $c_0 = 2.8$ mM (black) and $c_0 = 14$ mM (grey). The spectra were taken at $\Delta t = 0.25$ ps (solid lines) and $\Delta t = 0.42$ ps (dashed lines) after excitation.

cay parameter. The lifetime of $\tau_1 = 90$ fs is therefore directly assignable to the ultrafast deactivation of the optically bright $\pi\pi^*$ excited electronic state(s). Given the efficient association ($\beta = 0.60 - 0.80$), it refers predominantly to the H-bonded inosine dimer with some corresponding monomer contribution.

The minor second component (τ_2) required to describe the absorption-time profiles at near-UV probe wavelengths, which was found to increase in value from ≈ 0.20 ps at $\lambda_{probe} = 420$ nm to ≈ 0.58 ps at 340 nm, is attributed to electronic absorption by highly vibrationally excited S_0 molecules, as is known from measurements of other purine bases in aqueous solution.[39,40] The ensuing vibrational cooling of the molecules in a non-equilibrium distribution in the S_0 state cannot be expected to be described by a single fixed time constant. The apparent increase of τ_2 with decreasing probe wavelength and the slight blue-shift of the absorption maximum in the UV (cf. Fig. 5.6) support the above assignment. A more detailed understanding of the underlying dynamics would require a very careful analysis of the hot ground state absorption-time profiles in the probe wavelength range 260 nm $\leqslant \lambda_{probe} \leqslant$ 320 nm. This task has been outside the scope of the present study of the excited electronic state dynamics, but may form a subject of future work.

Third in this context, the time constant $\tau_3 = 9.4 \pm 1.0$ ps found at $\lambda_{probe} = 244$ nm reflects the eventual recovery of the S_0 ground state. The observed vibrational cooling process is much slower in $CHCl_3$ compared to the corresponding dynamics in, e.g., water.[41–45] Therefore, since the vibrational relaxation in S_0 is much slower than the excited-state depopulation, monitoring the ground-state recovery alone is not sufficient for investigating the excited electronic state dynamics, but does demonstrate the absence of any long-lived photoproducts.

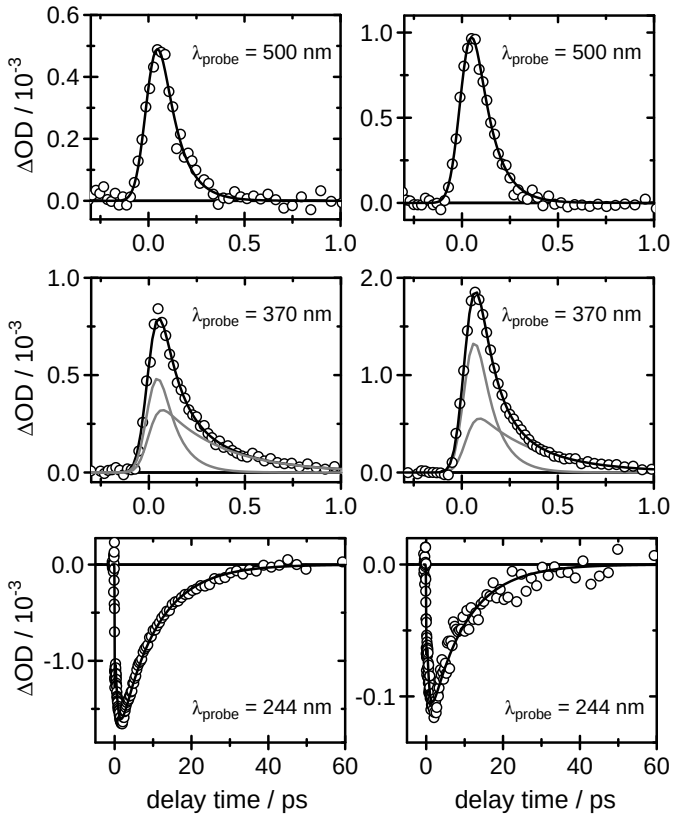

Figure 5.7: Time profiles of inosine in $CHCl_3$ at $c_0 = 2.8$ mM (left) and $c_0 = 14$ mM (right) at selected probe wavelengths. Open circles represent data points, solid black lines the fitted overall profiles, and grey lines indicate the single contributions.

The results summarized to this point may be compared to those of a number of reported previous studies. In particular, very similar ultrafast excited electronic state dynamics to those observed in the present study have been found before for the monomers hypoxanthine and inosine in aqueous solution.[18–20] Both exhibit excited-state lifetimes between $\tau = 0.21 \pm 0.08$ ps[18] and $\tau = 0.13 \pm 0.2$ ps.[19] Those values appear to be a bit longer than the present data for I and I·I in $CHCl_3$, but lifetime differences of several tens of femtoseconds should be considered with some caution. As in the present study, the effective experimental decay times in water were found to increase slightly (to ≈ 0.46 ps) at near-UV probe wavelengths due to contributions to the transient absorption profiles by vibrationally highly excited S_0 molecules. In any case, the observed electronic lifetimes of hypoxanthine or inosine in a monomeric form and the inosine dimer are among the shortest of all nucleobases and nucleobase dimers studied so far.

The relaxation coordinate of hypoxanthine in aqueous solution has been discussed to be the out-of-plane deformation of the six-membered ring through puckering motion at the C(2) position or out-of-plane displacement of the C(2)=N(3) bond. The considerably faster excited-state decay compared to guanine is likely due to less motional resistance along the

puckering coordinate by the light hydrogen atom in the hypoxanthine chromophore as opposed to the considerably larger exocyclic amino group present in guanine. In guanine, the comparably heavier and larger amino substituent at C(2) may hamper the large-amplitude out-of-plane movement of the C(2)–NH_2 moiety by increased inertia and solvent friction. A second factor coming into play in protic solvents like water may be intermolecular hydrogen-bonding between the amino group and surrounding solvent molecules. For guanine in aqueous solution, three governing time scales of ≈ 0.2 ps, $0.67 - 0.9$ ps and 2.0 ps were found in recent transient absorption and time-resolved fluorescence measurements.[39,46] These were attributed to the direct relaxation by internal conversion from the $\pi\pi^*$ state to the electronic ground state via the above mentioned ring distortion, as proposed in a number of theoretical studies.[39,47–53] A shallow minimum or plateau that was predicted for guanine was suggested to result in the experimentally observed rather complex decay behaviour. The initially prepared wavepacket most likely may spread out in the extended flat region of the potential energy hypersurface, leading to a slow-down of the wavepacket motion along the deactivation coordinate. A recently published experimental study of guanosine deactivation dynamics also proposed an involvement of a $\pi\sigma^*$ state located at the amino N–H bond to be responsible for the complex behaviour.[54] In any case, the rather simple and straightforward, but clearly faster dynamics of hypoxanthine compared to guanine shows the influence and importance of the exocyclic amino group on the electronic deactivation in guanine vs. hypoxanthine, may it be by geometrical restraints or by electronic effects.

Regarding the similarity of hypoxanthine monomer and dimer deactivation dynamics, a similar relaxation coordinate is quite likely. Here, it strikes that the hydrogen bonds in the dimer structure restrict neither the C(2) nor the N(3) position (cf. Fig. 5.1), thus explaining the evidently small influence of dimerisation on the deactivation dynamics. If there is any effect (see discussion above), electronic relaxation in the dimer appears to occur slighly faster than in the monomer. In view of the already cited theoretical work on G·C,[21,22] an ultrafast charge-transfer transition comes into mind, but the small difference between Hyp or I in water and I·I in $CHCl_3$ may also simply result from a solvent shift of the involved electronic states. In the absence of theoretical work on the dimer, this question has to remain open. On the other hand, a restraint, e.g. by a substituent causing solvent friction and/or an intramolecular H-bond, at one of the C(2) or N(3) positions seems to lead to a considerable increase of electronic lifetimes. This has recently been shown for large aggregates of guanine in *n*-hexane, where the exocyclic amino group is involved in H-bonding, evidently resulting in a considerable increase of excited-state lifetimes compared to the monomer.[36,55] In another study, Zelený et al. found by QM/MM simulation that the incorporation of guanine into DNA leads to an increase of excited-state lifetime from $\tau = 0.22$ ps for the free base to $\geqslant 0.5$ ps. In line with the experimental observations mentioned above, this was explained by the geometrical constraints induced by hydrogen bonds to the amino

group.[56] The results in the present study thus emphasize the outstanding importance of the C(2) position for the electronic deactivation of guanine, as noted above.

5.4 CONCLUSION

In this study, the structural properties and electronic deactivation dynamics of the inosine dimer in $CHCl_3$ have been investigated using ^1H NMR, FTIR and femtosecond time-resolved transient absorption spectroscopy. A symmetric, well-definded dimer structure was found with an association equilibrium constant $K_{I\cdot I} = 690 \pm 100\ M^{-1}$. The excited-state absorption after electronic excitation at $\lambda_{pump} = 260$ nm was observed to decay with a lifetime of $\tau = 90 \pm 10$ fs. This lifetime and the observed spectral characteristics have been discussed in comparison with the deactivation dynamics of inosine in water. The main electronic relaxation pathway in the monomer and the dimer seems to involve an out-of-plane deformation of the six-membered ring. The comparison of recent results for the electronic deactivations of guanine and hypoxanthine emphasises the likely importance of the substituents at the C(2) atom for the dynamics. The formation of long-lived photoproducts such as radicals or triplet species was ruled out by detection of the ground-state recovery.

Eventually, the experimental results support a rather straightforward picture for the electronic deactivation in the inosine dimer. Since the data show only a small if any influence of H-bonding on the electronic relaxation, the dynamics in this purine base homodimer does not appear to be ruled by effects arising from dimerisation. The experimental results are understandable because the I·I dimer lacks pronounced electronic effects by, e.g., large differences of oxidation potentials as are encountered in the A·T and especially in the G·C base pairs. The ultrafast, barrierless, direct excited-state relaxation channel does not allow for competing processes such as internal conversion to longed-lived $n\pi^*$ states, intermolecular hydrogen atom transfer, or triplet formation as have been proposed for, e.g., H-bonded aggregates of guanine.[36,55] Last but not least, the unambiguously determined, well-defined symmetric structure of the inosine dimer has to be emphasized, in contrast to the complex multi-isomeric structures of other purine base homodimers. The C(2) atom in the six-membered ring known to be important for the deactivation dynamics is not connected to hydrogen-bonding. These points and the straightforward ultrafast dynamics therefore qualify the I·I homodimer as an excellent reference system for the discussion of the much more complicated G·G, G·C or A·T base pairs, where additional, dimer-specific relaxation pathways are supposed to play key roles.[21–29]

ACKNOWLEDGMENTS

The financial support of this work by the Deutsche Forschungsgemeinschaft is gratefully acknowledged.

BIBLIOGRAPHY

[1] Hill-Perkins, M.; Jones, M. D.; Karran, P. *Mutat. Res.* **1986**, *162*, 153 – 163.

[2] Schouten, K. A.; Weiss, B. *Mutat. Res.* **1999**, *435*, 245–254.

[3] Kyogoku, Y.; Lord, R. C.; Rich, A. *Biochim. Biophys. Acta* **1969**, *179*, 10–17.

[4] Martin, F. H.; Castro, M. M.; Aboul-ela, F.; Tinoco, I. *Nucleic Acids Res.* **1985**, *13*, 8927–8938.

[5] Ohtsuka, E.; Matsuki, S.; Ikehara, M.; Takahashi, Y.; Matsubara, K. *J. Biol. Chem.* **1985**, *260*, 2605–2608.

[6] Valentine, M. R.; Termini, J. *Nucleic Acids Res.* **2001**, *29*, 1191–1199.

[7] Kow, Y. W. *Free Radical Biol. Med.* **2002**, *33*, 886 – 893.

[8] Paragi, G.; Pálinkó, I.; Van Alsenoy, C.; Gyémánt, I. K.; Penke, B.; Timár, Z. *New J. Chem.* **2002**, *26*, 1503–1506.

[9] Watkins, N. E.; SantaLucia, J. *Nucleic Acids Res.* **2005**, *33*, 6258–6267.

[10] Karran, P.; Lindahl, T. *Biochemistry* **1980**, *19*, 6005–6011.

[11] Nguyen, T.; Brunson, D.; Crespi, C. L.; Penman, B. W.; Wishnok, J. S.; Tannenbaum, S. R. *Proc. Natl. Acad. Sci. U.S.A.* **1992**, *89*, 3030–3034.

[12] Spencer, J. P. E.; Jenner, A.; Chimel, K.; Aruoma, O. I.; Cross, C. E.; Wu, R.; Halliwell, B. *FEBS Lett.* **1995**, *375*, 179–182.

[13] Pang, B.; McFaline, J. L.; Burgis, N. E.; Dong, M.; Taghizadeh, K.; Sullivan, M. R.; Elmquist, C. E.; Cunningham, R. P.; Dedon, P. C. *Proc. Natl. Acad. Sci. U.S.A.* **2012**, *109*, 2319–2324.

[14] Ohtsuka, E. *Proc. Jpn. Acad., Ser. B* **2005**, *81*, 393–402.

[15] Siegfried, N. A.; Metzger, S. L.; Bevilacqua, P. C. *Biochemistry* **2007**, *46*, 172–181, PMID: 17198387.

[16] Sun, X.; Lee, J. K. *J. Org. Chem.* **2010**, *75*, 1848–1854.

[17] Krepl, M.; Otyepka, M.; Banáš, P.; Šponer, J. *J. Phys. Chem. B* **2013**, *117*, 1872–1879.

[18] Röttger, K.; Siewertsen, R.; Temps, F. *Chem. Phys. Lett.* **2012**, *536*, 140 – 146.

[19] Chen, J.; Kohler, B. *Phys. Chem. Chem. Phys.* **2012**, *14*, 10677–10682.

[20] Villabona-Monsalve, J. P.; Noria, R.; Matsika, S.; Peón, J. *J. Am. Chem. Soc.* **2012**, *134*, 7820–7829.

[21] Sobolewski, A. L.; Domcke, W. *Phys. Chem. Chem. Phys.* **2004**, *6*, 2763–2771.

[22] Sobolewski, A. L.; Domcke, W.; Hättig, C. *Proc. Natl. Acad. Sci. U.S.A.* **2005**, *102*, 17903–17906.

[23] Abo-Riziq, A.; Grace, L.; Nir, E.; Kabelac, M.; Hobza, P.; de Vries, M. S. *Proc. Natl. Acad. Sci. U.S.A.* **2005**, *102*, 20–23.

[24] Sobolewski, A. L.; Domcke, W. *ChemPhysChem.* **2006**, *7*, 561–564.

[25] Schwalb, N. K.; Temps, F. *J. Am. Chem. Soc.* **2007**, *129*, 9272–9273.

[26] Groenhof, G.; Schäfer, L. V.; Boggio-Pasqua, M.; Goette, M.; Grubmüller, H.; Robb, M. A. *J. Am. Chem. Soc.* **2007**, *129*, 6812–6819.

[27] Schwalb, N. K.; Michalak, T.; Temps, F. *J. Phys. Chem. B* **2009**, *113*, 16365–16376.

[28] Biemann, L.; Kovalenko, S. A.; Kleinermanns, K.; Mahrwald, R.; Markert, M.; Improta, R. *J. Am. Chem. Soc.* **2011**, *133*, 19664–19667.

[29] Yamazaki, S.; Taketsugu, T. *Phys. Chem. Chem. Phys.* **2012**, *14*, 8866–8877.

[30] Ogilvie, K. K. *Can. J. Chem.* **1973**, *51*, 3799–3807.

[31] Hupp, T.; Sturm, C.; Basílio Janke, E. M.; Pérez Cabre, M.; Weisz, K.; Engels, B. *J. Phys. Chem. A* **2005**, *109*, 1703–1712.

[32] Yang, M.; Szyc, Ł.; Röttger, K.; Fidder, H.; Nibbering, E. T. J.; Elsaesser, T.; Temps, F. *J. Phys. Chem. B* **2011**, *115*, 5484–5492.

[33] Fidder, H.; Yang, M.; Nibbering, E. T. J.; Elsaesser, T.; Röttger, K.; Temps, F. *J. Phys. Chem. A* **2013**, *117*, 845–854.

[34] Biemann, L.; Häber, T.; Maydt, D.; Schaper, K.; Kleinermanns, K. *J. Chem. Phys.* **2008**, *128*, 195103.

[35] Greve, C.; Preketes, N. K.; Fidder, H.; Costard, R.; Koeppe, B.; Heisler, I. A.; Mukamel, S.; Temps, F.; Nibbering, E. T. J.; Elsaesser, T. *J. Phys. Chem. A* **2012**, *117*, 594–606.

[36] Röttger, K.; Schwalb, N. K.; Temps, F. *J. Phys. Chem. A* **2013**, *117*, 2469–2478.

[37] Weast, R. C., Ed. *CRC Handbook of Chemsitry and Physics*, 67th ed.; CRC Press, 1986-1987; pp E58–E59.

[38] Schwalb, N. K.; Temps, F. *J. Photochem. Photobiol., A* **2009**, *208*, 164 – 170.

[39] Karunakaran, V.; Kleinermanns, K.; Improta, R.; Kovalenko, S. A. *J. Am. Chem. Soc.* **2009**, *131*, 5839–5850.

[40] Pecourt, J.-M. L.; Peon, J.; Kohler, B. *J. Am. Chem. Soc.* **2001**, *123*, 10370–10378.

[41] Rothschild, W. G.; Rosasco, G. J.; Livingston, R. C. *J. Chem. Phys.* **1975**, *62*, 1253–1268.

[42] Graener, H.; Seifert, G. *J. Chem. Phys.* **1993**, *98*, 36–45.

[43] Graener, H.; Zürl, R.; Hofmann, M. *J. Phys. Chem. B* **1997**, *101*, 1745–1749.

[44] Sibert, E. L.; Rey, R. *J. Chem. Phys.* **2002**, *116*, 237–257.

[45] Graener, H.; Zürl, R.; Bartel, M.; Seifert, G. *J. Mol. Liq.* **2000**, *84*, 161–168.

[46] Miannay, F.-A.; Gustavsson, T.; Banyasz, A.; Markovitsi, D. *J. Phys. Chem. A* **2010**, *114*, 3256–3263.

[47] Serrano-Andrés, L.; Merchán, M.; Borin, A. C. *J. Am. Chem. Soc.* **2008**, *130*, 2473–2484.

[48] Yamazaki, S.; Domcke, W. *J. Phys. Chem. A* **2008**, *112*, 7090–7097.

[49] Yamazaki, S.; Domcke, W.; Sobolewski, A. L. *J. Phys. Chem. A* **2008**, *112*, 11965–11968.

[50] Serrano-Andrés, L.; Merchán, M. *J. Photochem. Photobiol., C* **2009**, *10*, 21–32.

[51] Lan, Z.; Fabiano, E.; Thiel, W. *ChemPhysChem.* **2009**, *10*, 1225–1229.

[52] Barbatti, M.; Szymczak, J. J.; Aquino, A. J. A.; Nachtigallová, D.; Lischka, H. *J. Chem. Phys.* **2011**, *134*, 014304.

[53] Heggen, B.; Lan, Z.; Thiel, W. *Phys. Chem. Chem. Phys.* **2012**, *14*, 8137–8146.

[54] Cheng, C. C.-W.; Ma, C.; Chan, C. T.-L.; Ho, K. Y.-F.; Kwok, W.-M. *Photochem. Photobiol. Sci.* **2013**, DOI: 10.1039/C3PP25450J.

[55] Hunger, K.; Buschhaus, L.; Biemann, L.; Braun, M.; Kovalenko, S.; Improta, R.; Kleinermanns, K. *Chem. Eur. J.* **2013**, *19*, 5425–5431.

[56] Zelený, T.; Ruckenbauer, M.; Aquino, A. J. A.; Müller, T.; Lankaš, F.; Dršata, T.; Hase, W. L.; Nachtigallova, D.; Lischka, H. *J. Am. Chem. Soc.* **2012**, *134*, 13662–13669.

6

ELECTRONIC DEACTIVATION OF GUANOSINE IN EXTENDED HYDROGEN-BONDED SELF-ASSEMBLIES

Katharina Röttger,[a] Nina K. Schwalb,[b] Friedrich Temps[a]*

[a] Institut für Physikalische Chemie, Christian-Albrechts-Universität zu Kiel, Olshausenstr. 40, 24098 Kiel, Germany

[b] Present Adress: Bayer Technology Services GmbH, 51368 Leverkusen, Germany.

Reprinted with permission from
J. Phys Chem. A, **2013**, *117*, 2469-2478.

OWN CONTRIBUTIONS TO THIS MANUSCRIPT:

- Femtosecond time-resolved transient absorption spectroscopy
- Analysis of femtosecond time-resolved data

* To whom correspondence should be addressed. E-mail: temps@phc.uni-kiel.de

ABSTRACT

Guanosine (G) derivatives in nonpolar aprotic solvents self-assemble to intricate hydrogen-bonded supramolecular architectures, including dimers, ribbons, and cyclic quartets. Considerable interest exists in the nature of the excited electronic states, their lifetimes and the radiationless deactivation mechanisms of the molecules in those environments. Here, we report on the electronic relaxation of G in the extended H-bridged networks in solution in *n*-hexane. The resulting architectures were sampled by FTIR, UV and CD spectroscopies. The dynamics after 260 nm photoexcitation were investigated by femtosecond fluorescence up-conversion, broadband UV-vis absorption, and single-color deep-UV measurements. The observed temporal profiles reveal a hierarchy of relaxation processes, with lifetimes $\tau_1 = 0.63 \pm 0.03$ ps, $\tau_2 = 5.9 \pm 0.3$ ps, and $\tau_3 = 62 \pm 7$ ps. Moreover, about 10 % of the photoexcited molecules transform to much longer-lived product states with lifetime $\tau_4 \approx 3.6 \pm 1.0$ ns. These excited-state lifetimes are much longer than in the G monomer or the G·G dimers studied previously, hinting at sizable energy shifts among the excited $\pi\pi^*$ and $n\pi^*$ states and trapping of excited-state population in the supramolecular networks by potential energy barriers along the optimal electronic deactivation pathways of the molecules.

6.1 INTRODUCTION

Guanine (G) stands out among the four canonical DNA bases for its unique ability to form multiple hydrogen bonds with more than one partner molecule. G-rich DNA runs, for instance, may arrange to distinctive quadruplex structures instead of the standard double helix.[1–4] Base sequences compatible with such configurations are encountered especially in the eukaryotic centromeres and telomeres,[4–7] which are essential for the stability of the DNA in mitotic cell division. The successive shortening and eventual loss of the telomeric G runs during DNA replication in eukaryotes leads to cellular senescence, growth arrest, and apoptosis. For this reason, these sequences have attracted strong interest as promising anti-cancer drug targets.[8] Unique intramolecular G-quadruplex conformations also occur in some aptamers,[9] which selectively bind to proteins and form useful tools for biotechnological and therapeutic applications. Moreover, the strong tendency of G to self-assemble makes this base an outstandig template and building-block for supramolecular chemistry[3,10] and molecular electronics.[10,11] In nonpolar aprotic solvents, guanosine derivatives may not only form a myriad of dimeric structures,[12] but assemble to extended hydrogen-bonded networks including long ribbons,[10,11,13–15] cyclic quartets,[15] and even helical aggregates.[16] The intricate H-bridged backbones of those architectures are of substantial fundamental interest.[17–22] In addition, the promising potential of G nanowires for molecular electronics and optoelectronics applications stimulated studies of their excited electronic state structure and dynamics.[23–25]

The structures of several important H-bridged G assemblies are depicted in Fig. 6.1. Both dimers 1 and 2 have been identified in gas phase spectra

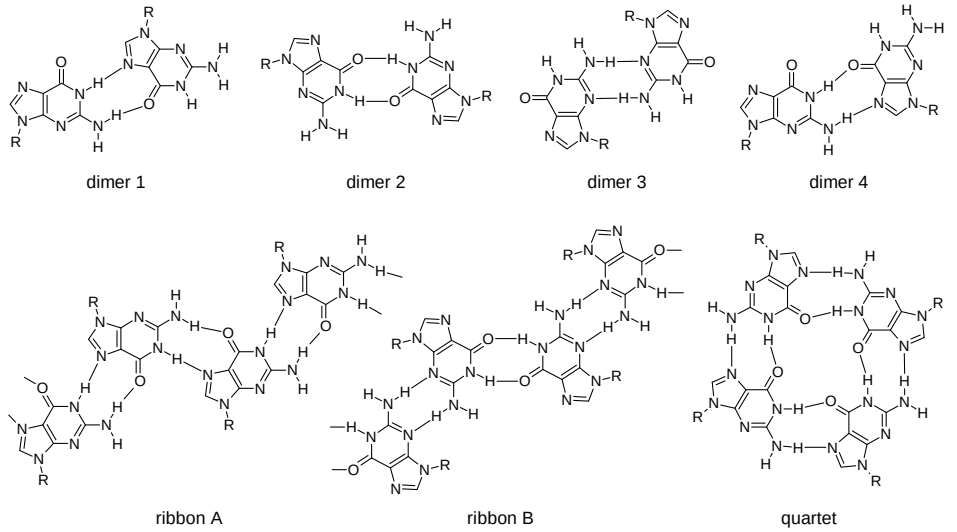

Figure 6.1: Structures of several H-bonded dimers, ribbons and the cyclic quartet of guanosine (G).

by Nir et al.,[12] but additional isomeric forms like dimers 3 and 4 may coexist in solution, e.g., in $CHCl_3$.[26–29] In apolar solvents like neat *n*-hexane (*n*-C_6H_{14}), we encounter even larger aggregation. As can be seen, the structure of ribbon A[11,14] replicates the H-binding scheme of dimer 1, whereas ribbon B[14,15] exhibits alternating dimer 2 and dimer 3 motifs. The cyclic quartet,[15] which assembles in the Hoogsteen structure and forms the G quadruplex motif when combined with a central metal ion,[20] shows the H-binding scheme of dimer 4. Stacked architectures have been found only at very high concentrations ($\gtrsim$ 1 M), especially in aqueous solution, where they form columnar liquid-crystalline phases.[13,30] NMR spectra of various G derivatives at millimolar concentrations in $CDCl_3$ show only H-bonding, but no signs for stacked aggregates.[13,15]

Much interest exists in the influence of the H-bonding networks on the electronic state structures, excited-state lifetimes and radiationless deactivation dynamics of the nucleosides. In the first place, the H-bonds are responsible for the formation of the complementary Watson-Crick (WC) base pairs in the DNA. The characters of the electronically excited states and the radiationless electronic deactivation mechanisms in the DNA have been found to differ dramatically from those of the free nucleobases, nucleosides, or nucleotides, which usually exhibit subpicosecond to few picosecond excited-state lifetimes.[31–35] Although the origin of the observed long-lived states in DNA can be rationalized, in principle, by exciton and excimer formation (although the exact mechanisms continue to be a matter of substantial controversy),[32,34,35] much less is known about the role of the hydrogen bonds in the base pairs in the electronic relaxation. Theoretical work[36–38] and gas phase spectroscopy[39,40] suggests a strong acceleration of the electronic deactivation in the isolated WC base pairs

by an electron-driven intermolecular proton transfer mechanism. For the guanosine-cytidine (G·C) WC pair and the G·G homodimer in solution in $CHCl_3$, we observed a significant shortening of the excited-state fluorescence lifetimes compared to the free nucleosides.[26,27] The H-bonding network may thus be of exceptional relevance for the photochemical stability of the DNA. Large H-bridged aggregates of C in *n*-C_6H_{14}, on the other hand, have shown relatively longer excited-state lifetimes.[41]

In the present paper, we report on a femtosecond time-resolved spectroscopic investigation of extended H-bonded guanosine aggregates in neat *n*-C_6H_{14} after electronic excitation of the sample molecules at $\lambda_{pump} = 260$ nm. The nucleoside was chemically modified by *tert*-butyldimethylsilyl (TBDMS) groups at the 2′,3′,5′-O atoms of the sugar moieties to enhance the solubility in *n*-C_6H_{14}, where the formation of multiple H-bridges among the bases is enforced. The resulting architectures were explored by static Fourier-transform infrared (FTIR), ultraviolet-visible (UV-vis) and circular dichroism (CD) spectroscopies, which hint at significant couplings between the chromophores in the aggregates. The ensuing excited electronic state dynamics were probed by femtosecond time-resolved fluorescence up-conversion, broadband UV-vis transient absorption, and single-color deep-UV transient absorption spectroscopy. The results reveal surprising orders-of-magnitude longer lifetime components of the molecules in the H-bridged networks compared to the monomeric nucleoside or nucleotide.

6.2 EXPERIMENTAL SECTION

MATERIALS

2′,3′,5′-O-TBDMS protected guanosine (denoted in the following as $G(TBDMS)_3$, or simply as G when obvious from the context) was synthesized using the method of Ogilvie[42] as described earlier.[26,27] The solvent *n*-C_6H_{14} (Uvasol purity, Merck) was dried using standard procedures. H-bonds between the bases and the solvent which would dominate in water or alcohols are ruled out in *n*-C_6H_{14}, while base stacking is avoided by working at sufficiently low concentrations ($c_0 \leqslant 5$ mM). It has been checked previously that the TBDMS groups do not affect the ultrafast photodynamics.[27]

STATIC SPECTRA

FTIR spectra of the H-bonded G aggregates were taken on a Bruker IFS 66v spectrometer using initial concentrations ranging from 0.1 mM $\leqslant c_0 \leqslant$ 10 mM in a variable pathlength cuvette equipped with CaF_2 windows. The spectra were recorded at room temperature. The exact pathlengths were determined from the interferograms of the empty cuvette. The sample compartment was flushed with dry N_2 to minimize atmospheric H_2O and

CO_2 absorptions. All spectra were corrected for the solvent measured as the background and for residual atmospheric contributions.

UV absorption spectra were recorded on a Shimadzu UV-2401 desktop spectrometer using a tightly plugged heatable cuvette. CD spectra were taken at room temperature on a JASCO J-715 spectrometer. Static fluorescence spectra were measured using a HORIBA Jobin Yvon FluoroMax-4 spectrometer. The excitation wavelength was $\lambda = 260$ nm. A Schott WG 295 filter was inserted to block the Raman peak caused by the solvent. Since the concentrations of G in n-C_6H_{14} were too high for the standard 90° detection geometry, the spectra were recorded in reflection to avoid inner filtering effects by placing the cuvette at $\approx 45°$. Measurements using guanosine monophosphate (GMP) at different concentrations in water at 90° and at 45° geometry verified that the fluorescence spectra were reproduced correctly.

FEMTOSECOND TIME-RESOLVED MEASUREMENTS

Time-resolved experiments were made using the femtosecond fluorescence up-conversion (FU)[43,44] and transient absorption (TA) techniques.[45] The sample solutions were measured in flow cells with 0.2 mm fused silica windows and optical pathlengths of 1 mm or 0.1 mm, depending on concentration. The applied pumping rates guaranteed that the irradiated volumes were exchanged between successive laser shots to avoid accumulation of photoproducts. Liquid reservoir volumes of $\geqslant 100 - 250$ mL ensured that no more than 1 % of the sample molecules were photoexcited during a set of measurements.

The excitation pulses for the FU and TA experiments were supplied by home-built non-collinear optical parametric amplifiers (NOPAs) pumped by a regeneratively amplified 1 kHz, 775 nm Ti:Sa laser system (Clark MXR CPA 2001). Both NOPAs had prism pulse compressors and BBO frequency doubling stages. The resulting UV pulses were steered into the sample cells by focusing mirrors ($f = 200$ mm). The pump energies for the FU measurements were reduced to $\leqslant 50$ nJ per pulse. Transmitted residual pump light was blocked by a beam stop and a Schott WG 320 filter. The laser-induced fluorescence was collected and refocused into a BBO crystal by two 90° off-axis parabolic mirrors ($f = 119$ mm) for type I sum frequency generation (SFG) with the time-delayed gate pulses from the Ti:Sa laser. The resulting SFG light was monitored at $\lambda_{SFG} = 241$ nm, corresponding to a fluorescence wavelength of $\lambda_{fl} = 350$ nm, using single-photon counting electronics. The reproducibility of the measurements was checked by recording up to four time scans per experimental run and one time scan with the neat solvent to rule out unwanted coherent effects, background signals or impurities.

Broadband UV-vis probe pulses for the TA experiment were obtained by supercontinuum generation in CaF_2. Additional single-color probe pulses in the deep-UV were provided by a third frequency-doubled NOPA to monitor the ground-state recovery (GSR) of the sample molecules after the

UV excitation. The applied pump energies were reduced to $\leqslant$ 200 nJ per pulse. The probe pulses were time-delayed with respect to the pump pulse using linear translation stages (PI GmbH), split into signal and reference beams by using the front- and back-reflections from a planar glass plate, and focused into the sample cell, where the signal pulses were spatially and temporally overlapped with the pump pulses. The transmitted broadband light pulses were dispersed in a prism spectrograph and detected by two full-frame transfer back-thinned CCD cameras (Hamamatsu S7030-0906). The single-color deep-UV pulses were monitored by two matched photodiodes (Hamamatsu S1227-66BQ). The CCD chips and photodiodes were read at 1 kHz repetition rate synchronized with the Ti:Sa laser via a custom-designed controller board (Entwicklungsbüro Stresing, Berlin) connected to a desktop computer (PC) for data acquisition and storage. The high readout rate in combination with good pulse-to-pulse stability and additional on-line pulse-to-pulse discrimination allowed for sensitivities of $\Delta OD \approx 2 \times 10^{-5}$ broadband and $\approx 5 \times 10^{-6}$ single-color. Each experimental run was repeated three times to ensure reproducibility. The neat solvent was measured before or afterwards under the same conditions to account for artifacts in the femtosecond transient absorption experiment arising from, e.g., cross-phase modulation (XPM) or UV multi-photon absorption (MPA) by the solvent.[46–48] XPM and MPA contribute to the probe signal in the first $\approx$ 50 fs (with the 0.1 mm flow cell) especially in the UV, where they accounted for almost $\approx$ 50 % of the measured signal with the sample. These artifacts were corrected for in the experiment with suitable scaling factors as have been described elsewhere,[46] but the data in the first $\approx 50-100$ fs time range should nevertheless be considered with some caution. The observed long-lived contributions to the absorption signals are not affected.

All experiments were controlled by LabView software.[49] Time profiles were analyzed using nonlinear least-squares fitting routines based on the Levenberg-Marquardt algorithm implemented in Mathematica.[50] The experimental time resolutions determined by the instrument response functions (IRF) were $\Delta t \approx 200$ fs in the FU and $\Delta t \approx 50$ fs in the TA measurements (1σ values of Gaussians describing the IRF).

6.3 RESULTS

STATIC FTIR AND UV/VIS SPECTRA

Static FTIR spectra of G(TBDMS)$_3$ in *n*-C_6H_{14} were recorded at a series of nucleoside concentrations between 0.1 mM $\leqslant c_0 \leqslant$ 10 mM to elucidate the structure of the ensuing H-bonded networks and their association equilibria. The analysis focused on the NH stretch vibrations in the 3200 – 3600 cm^{-1} region. The CO stretch/NH_2 bend region showed only broad and overlapping bands with little distinctive signature. The region around 3000 cm^{-1} was optically dark due to the solvent.

The FTIR spectra are displayed in Fig. 6.2 in comparison to a spectrum of G(TBDMS)$_3$ at similar concentration in $CHCl_3$ measured previously.[27] As can be seen, the spectra of G in *n*-C_6H_{14} are practically identical over

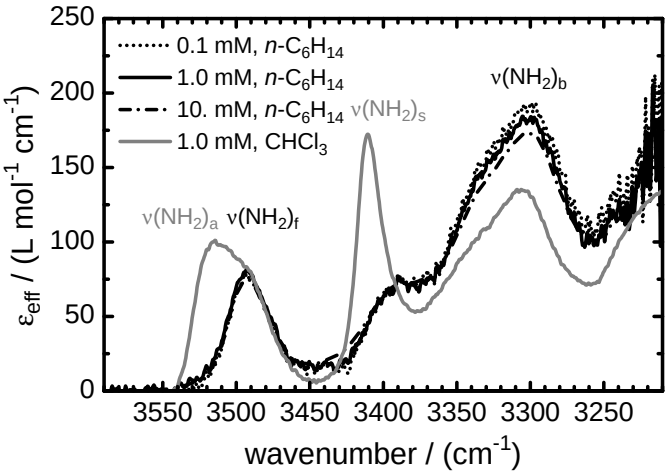

Figure 6.2: FTIR spectra of G(TBDMS)$_3$ in *n*-C_6H_{14} at different concentrations (black) in comparison to an FTIR spectrum of G(TBDMS)$_3$ in $CHCl_3$ (gray).

the entire concentration range studied. Moreover, there is virtually no sign in *n*-C_6H_{14} for the asymmetric and symmetric NH_2 stretch bands $\nu(NH_2)_a$ and $\nu(NH_2)_s$ of free NH_2 groups of G monomers that were seen in $CHCl_3$.[27] Judged from the spectra in $CHCl_3$, those bands should occur at $\omega \approx 3515$ and 3410 cm^{-1}, respectively. Instead, the FTIR spectrum in *n*-C_6H_{14} shows a rather broad, but symmetric, moderately intense absorption centered at $\omega = 3493$ cm^{-1}, roughly half-way between the expected $\nu(NH_2)_a$ and $\nu(NH_2)_s$ positions. A band at that frequency is the characteristic signature of the free N–H stretch vibration $\nu(NH_2)_f$ of an NH_2 group involved in one H-bond.[27] In $CHCl_3$, $\nu(NH_2)_f$ was observed at $\omega \approx 3491$ cm^{-1}. In addition, there is a moderately intense absorption in *n*-C_6H_{14} at $\omega \approx 3388$ cm^{-1} followed by very strong absorptions at ≈ 3335, 3300 and < 3250 cm^{-1}, which are typical for $\nu(N{-}H\cdots N)$ and/or $\nu(N{-}H\cdots OC)$ stretch vibrations in the H-bonding network.[27–29] Corresponding bands in $CHCl_3$ at ≈ 3340, 3305 and < 3250 cm^{-1} have been attributed to G dimers.[27] The increasing red-shift of the N–H stretching frequency and the concomitant increase in oscillator strength are known to correlate with a stronger hydrogen bond. The complex appearance of the spectrum at $\omega \leqslant 3400$ cm^{-1} likely originates from structural inhomogeneity, from Fermi resonances of the N–H stretching modes with overtones and combination of CO stretching and NH_2 bending modes, and anharmonic couplings to low-frequency modes. Similar behavior has been observed for the G·C Watson-Crick base pair in $CHCl_3$, where the analysis of the static FTIR spectra has been substantiated by two-dimensional IR spectroscopy and by femtosecond time-resolved dynamics measurements in the IR.[29]

As noted, the FTIR spectra of G in *n*-C_6H_{14} at concentrations from 0.1 – 10 mM look practically identical within experimental errors regarding both the distinct $\nu(NH_2)_f$ band and the strong, broad IR absorptions at < 3420 cm^{-1} from the $\nu(N{-}H\cdots N)$ and/or $\nu(N{-}H\cdots OC)$ vibrations in the H-bonding network. This indicates quite a strong association of the G building blocks to extended H-bonded networks. Unfortunately, the lack of clearly distinguishable, sharper features in the spectra in *n*-C_6H_{14} limits the amount of quantitative information on the G aggregates that can be extracted, but an attempt was made to estimate the residual contributions by free NH_2 vibrations ($\nu(NH_2)_a$ and $\nu(NH_2)_s$) based on the IR cross sections of related purine nucleosides, namely of adenosine and 2-aminopurine, in *n*-C_6H_{14} and $CHCl_3$, and guanosine in $CHCl_3$. Judged from this analysis, the fraction of molecules with free NH_2 groups not involved in H-bonds is < 5 % as an upper limit. Together with the presence of $\nu(NH_2)_f$ from NH_2 groups involved in one H-bond and the strong $\nu(N{-}H\cdots N)$ and $\nu(N{-}H\cdots OC)$ bands, the observed spectra are therefore assignable to either long ribbons (A or B, cf. Figure 6.1) or cyclic G quartets. Some further help arrives from the bond energies for the different dimers. Nir et al.[12] found dimer 2 as the most stable one (gas phase bond energy of about 8300 cm^{-1}), followed by dimer 1 ($\approx$ 5900 cm^{-1}). DFT calculations at the B3LYP+D/def2-TZVPP//B3LYP/6-31++g(d,p) level in our laboratory[51] confirmed this energetic ordering. These DFT bond energies were about 20 % higher for both dimers 2 and 1 than the values given by Nir et al., but the important point is that dimers 3 and 4 (which may not necessarily be planar) came out only about half as stable as dimer 2. The bond strengths may be slightly altered in solution, but their ordering is likely to remain intact considering the apolar nature of *n*-C_6H_{14}.

Taken together with the evidence from NMR and ESI-MS spectra in the literature,[14,15] the results thus suggest that ribbons A and B are likely types of structures of G in *n*-C_6H_{14} in equilibrium under the conditions of the present work. Both should be energetically close, because the average bond strength for alternating dimer 2 and 3 motifs in ribbon B appears similar to that of a dimer 1 unit in ribbon A. The above < 5 % limit for free NH_2 groups not involved in H-bonding based on the virtual absence of a distinguishable $\nu(NH_2)_a$ band hints at rather long aggregates, this also raises the chances for complicated mixed structures. Distinctive dimers with free NH_2 groups (the most stable being dimer 2 followed by dimer 1) are concluded to be present only in small concentrations in equilibrium in *n*-C_6H_{14}. The remaining free N–H side groups of the ribbons (cf. Figure 6.1) may in principle lend themselves to further networking, but such structures cannot be assessed on the basis of the present data and are judged less important considering the intensity of the $\nu(NH_2)_f$ band. High concentrations of cyclic quartets, on the other hand, appear less likely under the present conditions compared to linear ribbons considering the lower stability of the dimer 4 motif and the absence of templating Na^+ or K^+ cations that are usually required for the cyclic structure. Quartets without templating cations have been observed for G derivatives with large sub-

stituents at the C^8 position, however.[15] Summing up, therefore, the observed assemblies of G in *n*-C_6H_{14} are likely to be extended, complex and heterogeneous. Significant disorder is also supported by the very broad melting curve from the UV measurements in the following.

Figure 6.3 displays the electronic spectra of G(TBDMS)$_3$ in *n*-C_6H_{14} in the UV-VIS region. As can be seen (Figure 6.3a), the UV absorption maximum of G in *n*-C_6H_{14} at $\lambda = 258$ nm is red-shifted compared to guanosine in H_2O by ≈ 6 nm but practically coincident with the peak of the absorption of G in $CHCl_3$. The onset of the absorption at $\lambda \approx 300$ nm is not affected by the solvent. Most notably, the faint separation of the $\pi\pi^*(L_a)$ and $\pi\pi^*(L_b)$ bands contributing to the UV absorption of G has almost disappeared in the spectrum at room temperature in *n*-C_6H_{14}. This observation may be explained by the structural inhomogeneity of the observed assemblies as well as a more even distribution of the oscillator strengths of the two transitions due to excitonic coupling (see discussion). At $T = 75$ °C, however, the "normal" structure of the two bands of G in *n*-C_6H_{14} is recovered. As shown, the UV absorption of G in *n*-C_6H_{14} at 75 °C resembles that of G in $CHCl_3$ at room temperature, where the FTIR data showed the presence of a variety of G dimers. This suggests that the extended G networks in *n*-C_6H_{14} dissociate to smaller structures (e.g., dimers and monomers) at elevated temperatures. The broad melting curve shown in the inset of Figure 6.3a supports this interpretation. The dissociation to smaller aggregates seems to occur in a wide temperature range, as it would be expected for a heterogeneous mixture of different aggregates.

The CD spectrum of G(TBDMS)$_3$ in *n*-C_6H_{14} in Figure 6.3b is displayed in comparison to the spectra of G(TBDMS)$_3$ in $CHCl_3$ [26] and the d(G)$_{10}$ decamer in H_2O.[32] As shown, the CD of G in *n*-C_6H_{14} is clearly different from the CD in $CHCl_3$, where it is ascribed mainly to G·G dimer formation. The monomer (dGMP in water shown for reference) has little signature by comparison. The spectrum of d(G)$_{10}$, on the other hand, exhibits the typical G-stacking features of G-rich DNA molecules.[6,52,53] The distinctive CD of G in *n*-C_6H_{14} thus confirms the different H-bonding network structure in *n*-C_6H_{14} compared to that in $CHCl_3$ already deduced from the FTIR spectra.

Eventually, the fluorescence spectrum of G(TBDMS)$_3$ in *n*-C_6H_{14} (Figure 6.3c) is slightly red-shifted compared to the spectra of G(TBDMS)$_3$ in $CHCl_3$ or GMP in H_2O. This change suggests an energetic lowering of the emitting state(s) of G in *n*-C_6H_{14}.

FEMTOSECOND TIME-RESOLVED MEASUREMENTS

Femtosecond time-resolved measurements of the electronic relaxation of the sample molecules in the H-bridged networks in *n*-C_6H_{14} were carried out using the FU, broadband TA and single-color TA techniques. The excitation wavelength in all experiments was $\lambda_{pump} = 260$ nm, close to the maximum in the UV absorption spectrum of G. Typical time profiles mea-

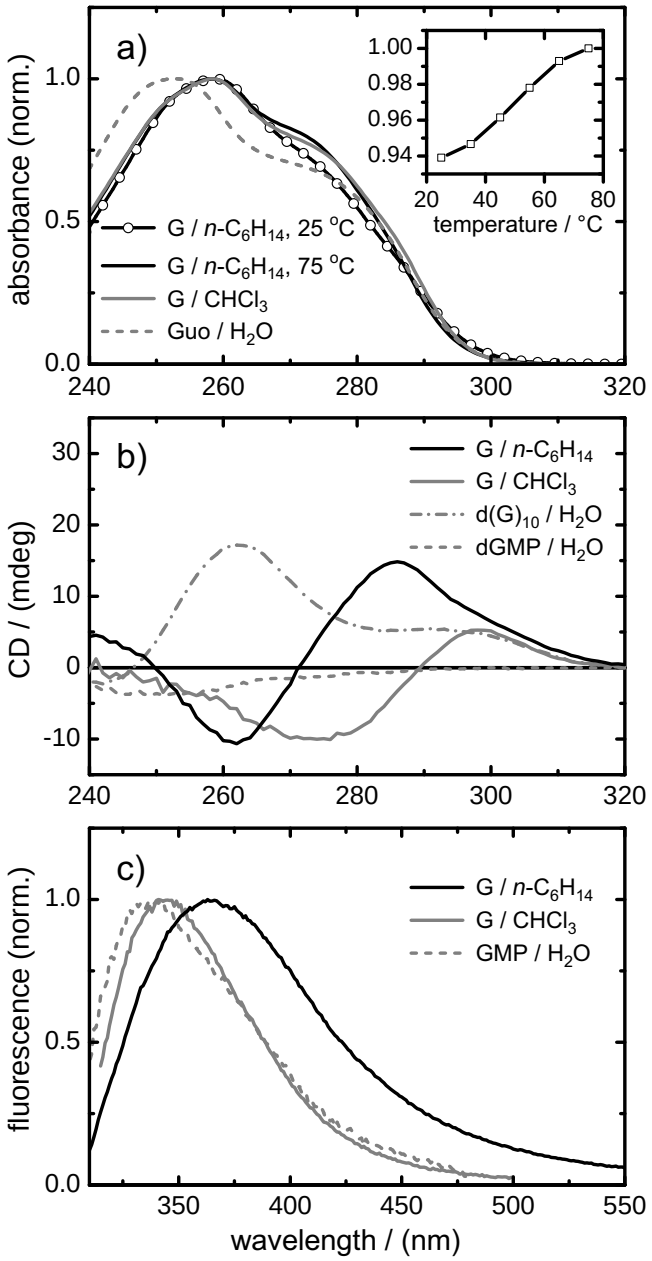

Figure 6.3: (a) UV absorption spectra of $G(TBDMS)_3$ in n-C_6H_{14} and $CHCl_3$ and unprotected guanosine (Guo) in H_2O. The inset shows the melting curve of $G(TBDMS)_3$ in n-C_6H_{14}. (b) CD spectra of $G(TBDMS)_3$ in n-C_6H_{14} and $CHCl_3$ compared to the CD spectra of the $d(G)_{10}$ decamer and the monophosphate dGMP in H_2O for reference. (c) Static fluorescence spectra of $G(TBDMS)_3$ in n-C_6H_{14} and $CHCl_3$ and the monophosphate GMP in H_2O. All spectra have been recorded at $c_0 = 0.10$ mM except for $d(G)_{10}$ ($c_0 = 0.02$ mM). The absorption and fluorescence spectra were normalized to their maxima for better comparison.

sured by the three complementary techniques are depicted in Figure 6.4.

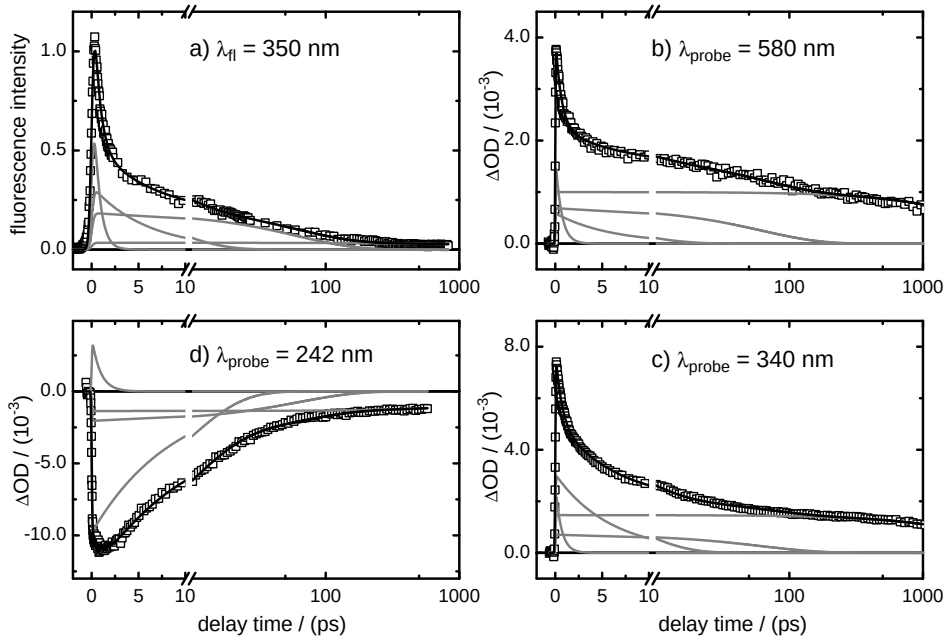

Figure 6.4: Measured transient fluorescence- and absorption-time profiles for G in *n*-C_6H_{14} after photoexcitation at $\lambda_{pump} = 260$ nm. Note the time scale, which is linear for the first 10 ps and logarithmic thereafter. a) Fluorescence at $\lambda_{fl} = 350$ nm ($c_0 = 1.0$ mM), b) absorption at $\lambda_{probe} = 580$ nm ($c_0 = 5.0$ mM), c) absorption at $\lambda_{probe} = 340$ nm ($c_0 = 5.0$ mM), d) absorption at $\lambda_{probe} = 242$ nm ($c_0 = 5.0$ mM). The best-fit curves to the data points (open symbols) are given by the black solid lines, the individual decay components are represented by gray lines.

The FU measurements were performed using sample concentrations of $c_0 = 0.1$ and 1.0 mM at $\lambda_{fl} = 350$ nm. The obtained time profiles at both concentrations were found to be practically identical within experimental error. However, the 0.1 mM measurement experienced higher scatter in the data due to the much lower photon count rates. Figure 6.4a thus shows the measured time profile at $c_0 = 1.0$ mM. As can be seen at first glance, the observed fluorescent excited states are far longer lived than for guanosine or GMP in H_2O or for G($TBDMS_3$) in $CHCl_3$, where sub-picosecond lifetimes have been established.[27] Fluorescence of G in *n*-C_6H_{14} was still detected at delay times of $\Delta t > 100$ ps. Moreover, the data reveal a sequence of dynamical processes occuring on several distinct time scales. As shown, the decay curves could be nicely modeled using a sum of three or (slightly better) four exponential decay functions convoluted with the IRF (see below). Additional measurements with excitation wavelengths nearer to the electronic origin (up to $\lambda_{pump} = 296$ nm) fully confirmed the picture, although some of the decay components at longer excitation wavelength turned out a bit slower.

The broadband UV-vis TA measurements were made with sample concentrations of $c_0 = 1.0$ and 5.0 mM at optical pathlengths of 1.0 mm and

0.1 mm, respectively. The probe wavelengths ranged from about 330 to 700 nm. The two-dimensional (2D) spectro-temporal absorption maps taken at both concentrations were very similar, except for stronger interference from XPM in the 1 mm cell ($c_0 = 1.0$ mM). For this reason, only the data at 5.0 mM will be discussed in the following. The respective 2D map and a set of transient spectra at selected delay times are displayed in Figures 6.5a and b. As can be seen, the spectra at early delay times show an in-

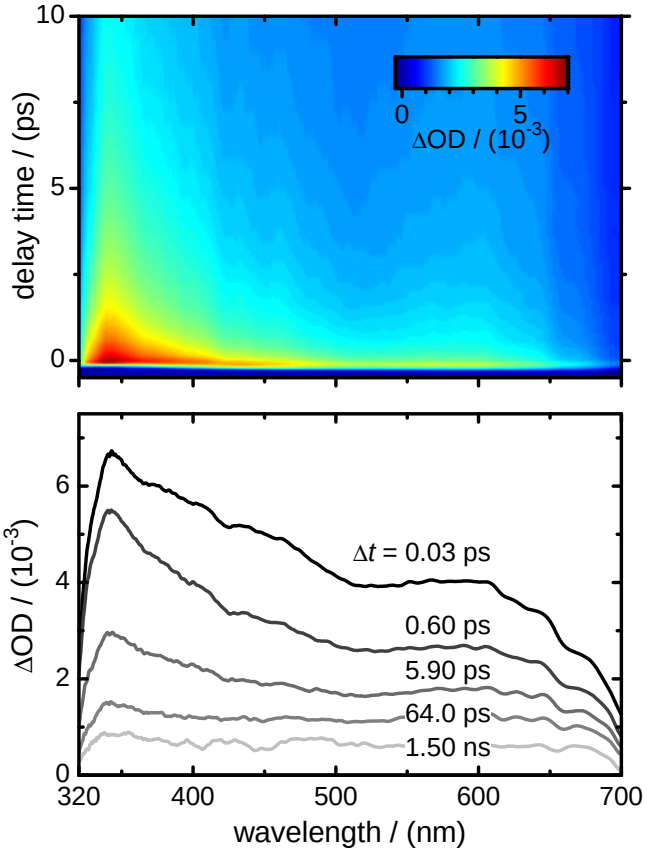

Figure 6.5: a) 2D spectro-temporal absorption map of G in *n*-C_6H_{14} at $c_0 = 5.0$ mM (0.1 mm optical pathlength) after photoexcitation at $\lambda_{pump} = 260$ nm. b) Transient absorption spectra extracted from the 2D map at selected delay times.

tense excited-state absorption (ESA) band with maximum at $\lambda \approx 340$ nm and a broad and unstructured ESA feature at longer wavelengths with maximum near ≈ 600 nm. From $\Delta t \approx 60$ ps on up to the longest delay time of $\Delta t = 1.5$ ns, the absorption extends fairly evenly over the entire wavelength range without distinctive features. The remaining absorption in this time range decayed too slowly for the accessible dynamic range of our experimental setup.

Representative ESA time profiles extracted from the spectro-temporal absorption map at two selected probe wavelengths, $\lambda_{probe} = 580$ and 340 nm, are given in Figures 6.4, panels b and c, respectively. As the fluorescence decay curves above, the data reflect electronic relaxation dynamics taking place on several distinctive time scales, which could be determined

by fitting of a sum of four exponentials convoluted with the IRF. Additional time profiles investigated at ten other probe wavelengths distributed across the experimental spectrum confirmed that the data at $\lambda_{probe} = 580$ and 340 nm in Figures 6.4, panels b and c, are representative.

Eventually, Fig. 6.4d shows the time profile provided by the deep-UV TA measurement at $\lambda_{probe} = 242$ nm. At this probe wavelength at higher energy than the pump ($\lambda_{pump} = 260$ nm), one may in principle encounter similar ESA behavior as at the longer wavelengths. However, in line with other experiments on the DNA bases,[34] the ESA is generally weaker than the absorption by the molecules in their electronic ground state, resulting in a strong negative signal at $\Delta t = 0$ due ground-state bleaching (GSB). The time profile at $\lambda_{probe} = 242$ nm thus differs from those at the longer wavelengths in that it probes the ground-state recovery (GSR) by the electronic deactivation of the photoexcited molecules. This process can be seen to take place for a large part on the time scale of several 10 to about 100 ps. However, a fraction of $\approx$ 11 % of the initial GSB amplitude remains even at $\Delta t \approx 1$ ns. This slowly decaying signal (slowly on the time scale of our experiment) hints at a population of long-lived ($\tau \approx 3.6$ ns, see below) excited states of much lower optical brightness regarding emission to the ground state (Fig. 6.4a), but good visibility in ESA (cf. Figures 6.4b–c).

The dynamics encoded in the FU and TA time profiles were analyzed by least-squares fitting. All parameters were free-floating unless noted otherwise. To begin with, each data curve was investigated separately. It turned out quickly, however, that within the present experimental errors all FU and TA time profiles describing excited-state populations from excitation at $\lambda_{pump} = 260$ nm could be described by a common set of time constants. The only exception were the data showing the GSR at $\lambda_{probe} = 242$ nm, which in part reflect different physical processes (below). The resulting excited-state lifetimes (with 2σ statistical uncertainties) provided by a subsequent global fit to the FU and TA data using a sum of four decaying exponentials convoluted with a Gaussian for the IRF are

$$\begin{aligned}
\tau_1 &= 0.63 \pm 0.03 \text{ ps}, \\
\tau_2 &= 5.90 \pm 0.30 \text{ ps}, \\
\tau_3 &= 62.0 \pm 7.0 \text{ ps}, \\
\tau_4 &= 3.6 \pm 1.0 \text{ ns}.
\end{aligned}$$

The relatively large error limit for τ_4 arises simply due to the limited dynamical time range that could be investigated with our setup.

A separate treatment was required for modeling the TA time profiles at $\lambda_{probe} = 242$ nm. As noted, the measured transients at this probe wavelength are negative, reflecting the bleach of the ground-state population upon photoexcitation of the sample molecules. In principle, the ground-state recovery (GSR) should show similar time constants as the excited-state decay (i.e., ESA) above. In the internal conversion (IC) of the excited electronic state, however, the ground-state molecules are born with a huge internal (vibrational) excitation. Full GSR therefore requires a dissipation

of the high internal excitation energy by vibrational energy transfer (VET) to the solvent. This process is expected on a timescale of roughly ≈ 10 ps. A fit to the 242 nm TA data therefore gave a slightly longer time constant compared to τ_2 of

$$\tau_2' = 8.7 \pm 0.3 \text{ ps},$$

while the values of $\tau_3 = 62.0$ ps and $\tau_4 = 3.6$ ns remained as above. The value of τ_1 obtained from the 242 nm TA data was of the same order as that given above, but less well determined due to a stronger XPM contribution. The underlying physical processes will be discussed in the following.

6.4 DISCUSSION

The electronic deactivation measurements on the H-bonded assemblies of G in *n*-C_6H_{14} after UV photoexcitation presented in the preceding section reveal an intricate hierarchy of dynamical processes proceeding on widely differing timescales, from $\tau_1 \approx 0.6$ ps to $\tau_4 \approx 3.6$ ns. This wide range of lifetimes which spans nearly four orders of magnitude obviously reflects different types of excited-state configurations that are reached in the course of the electronic relaxation of the molecules.

To set the stage for the following discussion, some general remarks on multi-exponential dynamics may be useful. In the first place, the femtosecond UV pump pulse projects a wavepacket from the ground state to the excited potential energy hypersurface (PEHS), where it subsequently evolves under the effect of the molecular Hamiltonian. Observable wavepacket dynamics are quite typically non-exponential when different regions on the PEHS are reached and accessed. For example, when excited-state structural relaxation leads to changes in emission, this could indicate departure from the Franck-Condon (FC) window, rapid intramolecular vibrational redistribution (IVR), and/or change in electronic character, e.g., by mixing of $\pi\pi^*$ and $n\pi^*$ states when the molecule becomes nonplanar. Transitions like departure from the FC region, approach of an extended flat region on the PEHS, and change in electronic character are well documented for the relaxation of DNA base monomers, where they are supported by electronic structure and quantum dynamics calculations.[34,54–56] IVR and vibrational cooling in the excited state, on the other hand, can be expected to be similar in guanine and adenine. However, because the measurements for both purines differ strongly,[34] those effects should not predominate here. In any case, however, one has to keep in mind that proposed intermediate "states" in the electronic relaxation may not necessarily correspond to local minima on a PEHS, but instead to dynamically distinct transient configurations. Further, given the complexity of the relaxation dynamics even in single base monomers and the size of the H-bonded G assemblies under investigation here, it is unreasonable at this time to expect definitive explanations for all experimental findings. Before this background, it is one of our tasks in the following to list possible mechanisms for further investigation. Comparison with the picture for the

monomer G nucleobase will allow us to pinpoint some critical issues. Eventually, we stress that the present measurements by three complementary experimental techniques converged nicely. In essence, the decay profiles of the optically bright UV-excited states seen in fluorescence, the development of the population in the excited electronic state(s) imaged by the transient excited-state absorption spectra, and the recovery of the population in the electronic ground state monitored in the deep-UV could be modeled by a common set of time constants. In this combination, the experiments projected an unusually well-substantiated and comprehensive picture of the electronic relaxation.

The involved (heterogeneous) structures of the G assemblies in *n*-C_6H_{14}, which likely prefer to develop extended H-bonded ribbons in complex equilibria, have already been discussed in some detail above. With the above premises, we therefore turn directly to the nature of the FC excited states prepared by the UV pump and notice first that the spectral positions of all transitions will be affected by the structural inhomogeneity of the assemblies. In the present case, there are two $\pi\pi^*$-type electronic transitions (L_a and L_b). Additionally, the possibility of excitonic coupling of the large number of chromophores has to be taken into consideration. Excitonic coupling has been successfully invoked to explain the different CD spectra of parallel- and antiparallel-stranded G quadruplexes.[22] Moreover, Markovitsi and co-workers modeled the optical properties of G quadruplexes and nanowires in the frame of exciton theory.[24,25] One notable outcome was that the oscillator strengths of the L_a and L_b transitions were distributed over a wider spectral range. This could contribute to the disappearance of the faint separation of those two bands in the UV spectra in the present case (cf. Fig. 6.3). A second interesting result was the prediction of the existence of long-lived weakly fluorescent excited states in the G nanowires with a ≈ 2 ns lifetime.[24] On the other hand, recent molecular beam studies showed that the actual excitonic splittings in H-bonded dimers of several nucleobase analogues are in fact quite small ($\approx 10-50$ cm^{-1}) owing to the effect of vibrational quenching.[57–60] These experimentally measured values came out more than an order of magnitude smaller than ab initio computed purely electronic Davydov exciton splittings of the S_1 and S_2 electronic states at the equilibrium geometries of the electronic ground states. The evidence for strong excitonic coupling in H-bonded nucleobase aggregates is therefore still inconclusive. The respective interactions in π-stacked systems seem to be much stronger.

As said, the results of the FU and TA measurements of the sample molecules after 260 nm photoexcitation converged nicely. According to the FU data (cf. Figure 6.4a), the subpicosecond component with lifetime $\tau_1 = 0.63$ ps accounts for about 65 % of the fluorescence amplitude of the photoexcited bright state, about 20 % of the fluorescence amplitude decays with a few-picosecond lifetime ($\tau_2 = 5.90$ ps). The combined contribution to the fluorescence amplitude by the long-lived states ($\tau_3 = 62$ ps, $\tau_4 = 3.6$ ns) is about 15 %. Since the τ_4 component is only just barely detectable in fluorescence, this emission must come from an excited state that has

lost most (but not all) of its optically bright character. The analysis of the broadband UV-vis and deep-UV TA time profiles provided the same lifetime values within experimental errors as the FU measurements. In the TA time profiles (cf. Figure 6.4, panels b and c), however, the long-lived states light-up with much more prominence, accounting for, respectively, $\approx$ 17 % ($\tau_3 = 62$ ps) and $\approx$ 25 % ($\tau_4 = 3.6$ ns) of the ESA signal at $\lambda_{probe} = 580$ nm and somewhat less at $\lambda_{probe} = 340$ nm. At $\lambda_{probe} = 242$ nm, hot ground state absorption (HGSA) is observed with a time constant of $\tau_2' = 8.7$ ps, which is typical for VET of highly excited large polyatomic molecules in nonpolar solvents.[61] While it is not possible to directly translate the ESA amplitudes into populations, the GSR time profile (cf. Figures 6.4d) shows that at least $\approx$ 25 % (15 % with $\tau_3 = 62$ ps, 10 % with $\tau_4 = 3.6$ ns) of the initial excited-state population develops into long-lived states with $>$ 10 ps lifetime. Those fractions are in fact lower limits, since possible positive ESA contributions at $\lambda_{probe} = 242$ nm may be hidden by the strong negative GSB and are unknown and neglected.

These results for G in *n*-C_6H_{14} stand in sharp contrast to previous measurements on the free G nucleobase or its nucleoside or mononucleotide. Accordingly, the embedding of the nucleobase in the large H-bridged networks that are formed in *n*-C_6H_{14} solution has major consequences for the ensuing electronic deactivation.

For free guanine in the gas phase, time-resolved pump-probe experiments established ultrafast electronic relaxation times of $\tau_1 = 0.15$ ps and $\tau_2 = 0.34$ ps.[62,63] For guanosine and GMP in aqueous solution at pH = 7, several FU and TA measurements observed multiphasic decays with time constants between $\tau_1 \approx 0.2$ - 1 ps and $\tau_2 \approx 2$ - 4 ps, depending on the method and on the probe wavelength.[64–67] The complex dynamics suggest that the laser-prepared wavepacket undergoes diffusive spreading on the excited PEHS before internal conversion through the conical intersection (CI) to the ground state.

Theoretical studies agree that the relaxation of the canonical 9H tautomer of guanine takes place via a direct non-adiabatic transition from the excited $\pi\pi^*(L_a)$ to the S_0 ground state involving strong out-of-plane distortions of the six-membered ring at the C^2 atom and the amino group.[56,68–73] The newest calculations identified two related CIs with differing degree of NH_2 deformation.[56,73] An extended flat region or shallow minimum on the excited PEHS with barrier height $\leqslant$ kT en route to the CI(s) is thought to be responsible for the "diffuseness" of the decay times of GMP in water.[66,67] The out-of-plane distortion of the six-membered ring and the amino group in the $\pi\pi^*$ minimum and planar region allows for a mixing of the $\pi\pi^*$ and $n\pi^*$ states such that the normally optically dark $n\pi^*$ state(s) may gain some oscillator strength and may become detectable by the FU experiment. Furthermore, the involvement of a $^1n\pi^*$ state in the dynamics is not as unlikely in the gas phase and in nonpolar solvents as in aqueous solution. Canuel et al.[63] suggested such a state in the context of their pump-probe experiments. Serrano-Andrés et al.[72] and Barbatti et at.[56] discussed its involvement based on theo-

retical calculations. In their picture, an ultrafast decay channel with subpicosecond lifetime is due to the rapid relaxation via the $\pi\pi^*(L_a)/S_0$ CI. A second, slightly longer-lived contribution is attributed to the population of an $n\pi^*$ state, possibly via a state switching from the upper $\pi\pi^*(L_b)$ to the $n\pi^*$ state. From the $n\pi^*$ state minimum, the electronic ground state can be repopulated via different relaxation coordinates, e.g., by distortion of the exocyclic amino group or torsion about the C^2N^3 bond.

By and large, the measured $\tau_1 = 0.63$ ps and $\tau_2 = 5.9$ ps components for the electronic relaxation of G in *n*-C_6H_{14} are compatible with the gas phase results and the reports for guanosine and GMP in water. Similar values have also been found for G in ethanol ($\tau_1 = 0.57$ ps, $\tau_2 = 4.6$ ps) and in $CHCl_3$ ($\tau_1 = 0.43$ ps, $\tau_2 = 4.2$ ps).[27] For G dimers, on the other hand, which are present with ≈ 75 % abundance in solution in $CHCl_3$ already at $c_0 \approx 1$ mM (see Fig. 6.2), a single-exponential decay with $\tau = 0.32$ ps has been determined.[27]

In the extended H-bridged G networks in *n*-C_6H_{14}, however, the out-of-plane distortion of the amino group at the C^2 position is disfavored since the purine moiety itself is restrained by H-bonds in at least two directions. The accessibility of the $\pi\pi^*(L_a)/S_0$ CI is consequently lower for larger aggregates than for the dimer structures. Regarding the energy at the CI, different solvent polarities may play roles as well. A potential energy minimum on the $\pi\pi^*$ PEHS with a barrier height well above kT might then easily lead to the observed long lifetime component of $\tau_3 = 62$ ps. Additionally, compared to the situation in a polar solvent like H_2O, the weakly polar $n\pi^*$ state should be energetically stabilized in the nonpolar *n*-C_6H_{14} relative to the more polar $\pi\pi^*$ state(s) to an extent that this effect allows for a trapping of population in the $n\pi^*$ state with lifetime up to nanoseconds (τ_4). In $CHCl_3$ with a dipole moment of ≈ 1 D, this stabilisation might be insufficient, thus explaining the absence of a component with long nanosecond lifetime for G dimers in $CHCl_3$. Moreover, an out-of-plane deformation of the free NH_2 group(s) as required along one of the major deactivation routes is still possible in dimers 1 and 2 in $CHCl_3$. Unfortunately, not enough is known about the structures of the important G dimers in $CHCl_3$. The role of exciton coupling[24] in the H-bonded networks deserves further attention in future work as well.

Eventually, the longest time constant ($\tau_4 = 3.6 \pm 1.0$ ns) could not be determined with very high accuracy due to the limited length of our pump-probe translation stage, but the least-squares fit suggests that the observed ESA signals return to zero within experimental precision on the several nanosecond timescale. No evidence was found for photoreaction products in UV spectra of the samples taken after prolonged UV exposure. Furthermore, the transient spectrum after $\Delta t = 1.5$ ns given in Figure 6.5b shows no resemblence to the spectra of the (G–H)$^\bullet$ H-abstraction product[74] or triplet species like the $^3G^\bullet$ radical[75] or ^{3}GMP.[76] The latter two are known to feature a pronounced absorption band at $\lambda \approx 380$ nm, for which Figure 6.5b gives no evidence. Instead, we observe little change in the shape of the transient spectra after the first few picoseconds. Never-

theless, the slow dynamics on the nanosecond time scale deserve further investigation.

6.5 CONCLUSIONS

Large hydrogen-bonded aggregates of guanosine (G) in solution in neat *n*-hexane have been investigated by static FTIR, UV-vis and CD spectroscopy and by femtosecond time-resolved fluorescence up-conversion and transient absorption spectroscopy following UV-photoexcitation at $\lambda = 260$ nm. At G concentrations of $c_0 = 0.1 - 10$ mM, the observed spectra demonstrate strong association of the molecules to extended H-bridged self-assemblies likely consisting mostly of long ribbons in equilibrium with smaller aggregates. The measured temporal profiles of the electronically excited molecules in the H-bonded networks reveal a hierarchy of electronic deactivation processes with time constants of $\tau_1 = 0.63 \pm 0.03$ ps, $\tau_2 = 5.9 \pm 0.3$ ps, $\tau_3 = 62 \pm 7$ ps, and $\tau_4 \approx 3.6 \pm 1.0$ ns. The subpicosecond and few-picosecond components are compatible with a direct relaxation of the $\pi\pi^*(L_a)$-excited molecules through a conical intersection to the S_0 ground state similar to the dynamics of monomeric guanosine or guanosine monophosphate at pH 7 in aqueous solution. The long-lived states with lifetimes τ_3 and τ_4, on the other hand, arise only in the H-bonded supramolecular G assemblies, they have no analogues in the G monomer or G dimers studied previously. Two effects are proposed: (1) The strong H-bridges in the extended aggregates are likely to result in a small potential energy barrier along the out-of-plane distortion coordinates of the C^2 atom and the NH_2 group en route to the $\pi\pi^*(L_a)/S_0$ intersection. (2) The lowest $n\pi^*$ state which lies close to the $\pi\pi^*(L_a)$ state is likely to be energetically stabilized in *n*-hexane relative to the $\pi\pi^*(L_a)$ state such that a fraction of the excited molecules may be trapped for a few nanoseconds. The issue of excitonic coupling in the H-bridged networks requires further investigation. The results showcase the very complex excited-state dynamics of guanosine in hydrogen-bonded supramolecular environments and may have relevance for the photobiophysical properties of G quadruplex DNA.

ACKNOWLEDGMENTS

The authors would like to thank Dr. Joachim Gripp for the syntheses of several batches of $G(TBDMS)_3$, Dr. Jan Boyke Schönborn for running DFT calculations on the G dimer structures, Prof. Dr. Joachim Grötzinger for access to his CD spectrometer, and the referees for helpful comments. The financial support of our work by the Deutsche Forschungsgemeinschaft is gratefully acknowledged.

BIBLIOGRAPHY

[1] Gellert, M.; Lipsett, M. N.; Davies, D. R. *Proc. Nat. Acad. Sci. USA* **1962**, *48*, 2013–2018.

[2] Guschlbauer, W.; Chantot, J.-F.; Thiele, D. *J. Biomol. Struct. Dyn.* **1990**, *8*, 491–511.

[3] Davis, J. T. *Angew. Chem. Int. Ed.* **2004**, *43*, 668–698.

[4] Mills, M.; Lacroix, L.; Arimondo, P. B.; Leroy, J.-L.; François, J.-C.; Klump, H.; Mergny, J. L. *Curr. Med. Chem. - Anti-Cancer Agents* **2002**, *2*, 627–644.

[5] Williamson, J. R. *Annu. Rev. Biophys. Biomol. Struct.* **1994**, *23*, 703–730.

[6] Bloomfield, V. A.; Crothers, D. M.; Tinoco, I. *Nucleic Acids: Structures, Properties and Functions*; University Science Books: Sausalito, 2000.

[7] Bianchi, A.; Shore, D. In *Encyclopedia of Biological Chemistry*; Lennarz, W. J., Lane, M. D., Eds.; Elsevier: Amsterdam, 2004; Vol. 4; pp 174–179.

[8] De Cian, A.; Lacroix, L.; Douarre, C.; Temime-Smaali, N.; Trentesaux, C.; Riou, J.-F.; Mergny, J.-L. *Biochimie* **2008**, *90*, 131–155.

[9] Worlinsky, J. L.; Basu, S. *J. Phys. Chem. B* **2009**, *113*, 865–868.

[10] Davis, J. T.; Spada, G. P. *Chem. Soc. Rev.* **2007**, *36*, 296–313.

[11] Rinaldi, R.; Maruccio, G.; Biasco, A.; Arima, V.; Cingolani, R.; Giorgi, T.; Masiero, S.; Spada, G. P.; Gottarelli, G. *Nanotechnology* **2002**, *13*, 398–403.

[12] Nir, E.; Janzen, C.; Imhof, P.; Kleinermanns, K.; de Vries, M. S. *Phys. Chem. Chem. Phys.* **2002**, *4*, 740–750.

[13] Gottarelli, G.; Masiero, S.; Mezzina, E.; Spada, G. P.; Mariani, P.; Recanatini, M. *Helv. Chim. Acta* **1998**, *81*, 2078–2092.

[14] Giorgi, T.; Grepioni, F.; Manet, I.; Mariani, P.; Masiero, S.; Mezzina, E.; Pieraccini, S.; Saturni, L.; Spada, G. P.; Gottarelli, G. *Chem. Eur. J.* **2002**, *8*, 2143–2152.

[15] Sessler, J. L.; Sathiosatham, M.; Doerr, K.; Lynch, V.; Abboud, K. A. *Angew. Chem. Int. Ed.* **2000**, *39*, 1300–1303.

[16] Giorgi, T.; Lena, S.; Mariani, P.; Cremonini, M. A.; Masiero, S.; Pieraccini, S.; Rabe, J. P.; Samorì, P.; Spada, G. P.; Gottarelli, G. *J. Am. Chem. Soc.* **2003**, *125*, 14741–14749.

[17] Jin, R.; Gaffney, B. L.; Wang, C.; Jones, R. A.; Breslauer, K. J. *Proc. Natl. Acad. Sci. U.S.A.* **1992**, *89*, 8832–8836.

[18] van Mourik, T.; Dingley, A. J. *Chem. Eur. J.* **2005**, *11*, 6064–6079.

[19] Romero Guzmán, M.; Liquier, J.; Brahmachari, S. K.; Taillandier, E. *Spectrochim. Acta A* **2006**, *64*, 495–503.

[20] González-Rodríguez, D.; van Dongen, J. L. J.; Lutz, M.; Spek, A. L.; Schenning, A. P. H. J.; Meijer, E. W. *Nature Chemistry* **2009**, *1*, 151–155.

[21] Víglaský, V.; Bauer, L.; Tlučková, K. *Biochemistry* **2010**, *49*, 2110–2120.

[22] Masiero, S.; Trotta, R.; Pieraccini, S.; De Tito, S.; Perone, R.; Randazzo, A.; Spada, G. P. *Org. Biomol. Chem.* **2010**, *8*, 2683–2692.

[23] Miannay, F.-A.; Banyasz, A.; Gustavsson, T.; Markovitsi, D. *J. Phys. Chem. C* **2009**, *113*, 11760–11765.

[24] Changenet-Barret, P.; Emanuele, E.; Gustavsson, T.; Improta, R.; Kotlyar, A. B.; Markovitsi, D.; Vayá, I.; Zakrzewska, K.; Zikich, D. *J. Phys. Chem. C* **2010**, *114*, 14339–14346.

[25] Hua, Y.; Changenet-Barret, P.; Improta, R.; Vayá, I.; Gustavsson, T.; Kotlyar, A. B.; Zikich, D.; Šket, P.; Plavec, J.; Markovitsi, D. *J. Phys. Chem. C* **2012**, *116*, 14682–14689.

[26] Schwalb, N. K.; Temps, F. *J. Am. Chem. Soc.* **2007**, *129*, 9272–9273.

[27] Schwalb, N. K.; Michalak, T.; Temps, F. *J. Phys. Chem. B* **2009**, *113*, 16365–16376.

[28] Yang, M.; Szyc, L.; Röttger, K.; Fidder, H.; Nibbering, E. T. J.; Elsaesser, T.; Temps, F. *J. Phys. Chem. B* **2011**, *115*, 5484–5492.

[29] Fidder, H.; Yang, M.; Nibbering, E. T. J.; Elsaesser, T.; Röttger, K.; Temps, F. *J. Phys. Chem. A* DOI: 10.1021/jp309237u.

[30] Mariani, P.; Spinozzi, F.; Federiconi, F.; Amenitsch, H.; Spindler, L.; Drevensek-Olenik, I. *J. Phys. Chem. B* **2009**, *113*, 7934–7944.

[31] Crespo-Hernández, C. E.; Cohen, B.; Hare, P. M.; Kohler, B. *Chem. Rev.* **2004**, *104*, 1977–2019.

[32] Schwalb, N. K.; Temps, F. *Science* **2008**, *322*, 243–245.

[33] Serrano-Andrés, L.; Merchán, M. *J. Photochem. Photobiol. C* **2009**, *10*, 21–32.

[34] Middleton, C. T.; de La Harpe, K.; Su, C.; Law, Y. K.; Crespo-Hernández, C. E.; Kohler, B. *Annu. Rev. Phys. Chem.* **2009**, *60*, 217–239.

[35] Gustavsson, T.; Improta, R.; Markovitsi, D. *J. Phys. Chem. Lett.* **2010**, *1*, 2025–2030.

[36] Sobolewski, A. L.; Domcke, W. *Phys. Chem. Chem. Phys.* **2004**, *6*, 2763–2771.

[37] Sobolewski, A. L.; Domcke, W.; Hättig, C. *Proc. Natl. Acad. Sci. U.S.A.* **2005**, *102*, 17903–17906.

[38] Perun, S.; Sobolewski, A.; Domcke, W. *J. Phys. Chem. A* **2006**, *110*, 9031–9038.

[39] Abo-Riziq, A.; Grace, L.; Nir, E.; Kabeláč, M.; Hobza, P.; de Vries, M. S. *Proc. Natl. Acad. Sci. U.S.A.* **2005**, *102*, 20–23.

[40] Samoylova, E.; Lippert, H.; Ullrich, S.; Hertel, I. V.; Radloff, W.; Schulz, T. *J. Am. Chem. Soc.* **2005**, *127*, 1782–1786.

[41] Schwalb, N. K.; Temps, F. *J. Photochem. Photobiol. A* **2009**, *208*, 164–170.

[42] Ogilvie, K. K. *Can. J. Chem.* **1973**, *51*, 3799–3807.

[43] Pancur, T.; Schwalb, N. K.; Renth, F.; Temps, F. *Chem. Phys.* **2005**, *313*, 199–212.

[44] Schwalb, N. K.; Temps, F. *J. Phys. Chem. A* **2009**, *113*, 13113–13123.

[45] Röttger, K.; Siewertsen, R.; Temps, F. *Chem. Phys. Lett.* **2012**, *536*, 140–146.

[46] Lorenc, M.; Ziolek, M.; Naskrecki, R.; Karolczak, J.; Kubicki, J.; Maciejewski, A. *Appl. Phys. B: Lasers Opt.* **2002**, *74*, 19–27.

[47] Dobryakov, A. L.; Kovalenko, S. A.; Ernsting, N. P. *J. Chem. Phys.* **2003**, *119*, 988–1002.

[48] Dobryakov, A. L.; Kovalenko, S. A.; Ernsting, N. P. *J. Chem. Phys.* **2005**, *123*, 044502.

[49] *LabView 8.0*; National Instruments, 2006.

[50] *Mathematica Version 8.0*; Wolfram Research, Inc., 2011.

[51] Schönborn, J. B. unpublished results.

[52] Trantírek, L.; Štefl, R.; Vorlíčková, M.; Koča, J.; Sklenář, V.; Kypr, J. *J. Mol. Biol.* **2000**, *297*, 907–922.

[53] Štefl, R.; Trantírek, L.; Vorlíčková, M.; Koča, J.; Sklenář, V.; Kypr, J. *J. Mol. Biol.* **2001**, *307*, 513–524.

[54] Barbatti, M.; Lischka, H. *J. Am. Chem. Soc.* **2008**, *130*, 6831–6839.

[55] Barbatti, M.; Aquino, A. J. A.; Szymczak, J. J.; Nachtigallová, D.; Hobza, P.; Lischka, H. *Proc. Natl. Acad. Sci. U.S.A.* **2010**, *107*, 21453–21458.

[56] Barbatti, M.; Szymczak, J. J.; Aquino, A. J. A.; Nachtigallová, D.; Lischka, H. *J. Chem. Phys.* **2011**, *134*, 014304.

[57] Ottiger, P.; Leutwyler, S.; Köppel, H. *J. Chem. Phys.* **2009**, *131*, 204308.

[58] Heid, C. G.; Ottiger, P.; Leist, R.; Leutwyler, S. *J. Chem. Phys.* **2011**, *135*, 154311.

[59] Ottiger, P.; Leutwyler, S.; Köppel, H. *J. Chem. Phys.* **2012**, *136*, 174308.

[60] Kopec, S.; Ottiger, P.; Leutwyler, S.; Köppel, H. *J. Chem. Phys.* **2012**, *137*, 184312.

[61] Elsaesser, T.; Kaiser, W. *Annu. Rev. Phys. Chem.* **1991**, *42*, 83–107.

[62] Kang, H.; Lee, K. T.; Jung, B.; Ko, Y. J.; Kim, S. K. *J. Am. Chem. Soc.* **2002**, *124*, 12958–12959.

[63] Canuel, C.; Mons, M.; Piuzzi, F.; Tardivel, B.; Dimicoli, I.; Elhanine, M. *J. Chem. Phys.* **2005**, *122*, 074316.

[64] Peon, J.; Zewail, A. H. *Chem. Phys. Lett.* **2001**, *348*, 255–262.

[65] Pecourt, J.-M. L.; Peon, J.; Kohler, B. *J. Am. Chem. Soc.* **2001**, *123*, 10370–10378.

[66] Karunakaran, V.; Kleinermanns, K.; Improta, R.; Kovalenko, S. A. *J. Am. Chem. Soc.* **2009**, *131*, 5839–5850.

[67] Miannay, F.-A.; Gustavsson, T.; Bányász, A.; Markovitsi, D. *J. Phys. Chem. A* **2010**, *114*, 3256–3263.

[68] Chen, H.; Li, S. *J. Chem. Phys.* **2006**, *124*, 154315.

[69] Marian, C. M. *J. Phys. Chem. A* **2007**, *111*, 1545–1553.

[70] Yamazaki, S.; Domcke, W. *J. Phys. Chem. A* **2008**, *112*, 7090–7097.

[71] Yamazaki, S.; Domcke, W.; Sobolewski, A. L. *J. Phys. Chem. A* **2008**, *112*, 11965–11968.

[72] Serrano-Andrés, L.; Merchán, M.; Borin, A. C. *J. Am. Chem. Soc.* **2008**, *130*, 2473–2484.

[73] Lan, Z.; Fabiano, E.; Thiel, W. *ChemPhysChem* **2009**, *10*, 1225–1229.

[74] Candeias, L. P.; Steenken, S. *J. Am. Chem. Soc.* **1989**, *111*, 1094–1099.

[75] Jian, L.; Wang, W.-F.; Zheng, Z.-D.; Yao, S.-D.; Zhang, J.-S.; Lin, N.-Y. *Res. Chem. Intermediat.* **1991**, *15*, 293–301.

[76] Wood, P. D.; Redmond, R. W. *J. Am. Chem. Soc.* **1996**, *118*, 4256–4263.

7

ELECTRONIC DEACTIVATION OF THE GC BASE PAIR IN SOLUTION - EXPERIMENTAL EVIDENCE FOR A DIMER-SPECIFIC ADDITIONAL DECAY CHANNEL

7.1 INTRODUCTION

The influence of hydrogen-bonding on the excited-state dynamics of DNA building blocks is a controversially discussed field. The focus of this debate lies on the question whether the electronic deactivation mechanism of the Watson-Crick (WC) G·C base pair is substantially different from the monomer deactivation or not. A detailed discussion about the current state of knowledge and most recent publications is given in Section 1.2.3 in comparison with other H-bonded systems of purine and pyrimidine bases. Here, a short overview of the most important results for the G·C base pair will be given.

It has been proposed by Löwdin in 1965 that a double proton-transfer (DPT) process might occur within DNA base pairs. This hypothesis was checked by a detailed and thorough study of DPT reactions in model systems, e.g., in dimers of 7-azaindole[1–5] and 2-aminopyridine.[6–8] In the heterodimer G·C, an electron-driven proton transfer (EDPT), where only a single proton is transferred from G to C, was theoretically predicted by Sobolewski, Domcke and Yamazaki.[9–12] This process was confirmed by a number of several dynamics simulation studies over the last years that showed a distinct shortening of excited electronic state lifetimes in the G·C base pair compared to the monomers.[13–17] Additionally, the involvement of single-proton transfer from C to G was discussed.[12,18] From the experimental point of view, the results are not unambiguous. Many experimental findings in the gas phase[19] as well as in solution[20,21] hint indeed at a dramatic reduction of lifetimes of electronically excited states in the G·C base pair as was proposed theoretically. However, a recent combined transient absorption and TD-DFT study of the G·C base pair in $CHCl_3$ claimed the involvement of an EDPT process to be unlikely.[22] The employed excitation wavelength in the respective study was 283 nm, which leads to an excitation mainly of C. Since the EDPT process starts with a proton transfer from the electronically excited G, this might explain the small changes between monomer contribution and the G·C base pair specific signal. Altogether, the direct observation of a G·C base pair specific deactivation channel is still missing.

In this Chapter, the preliminary results of femtosecond time-resolved transient absorption measurements of the G·C base pair in $CHCl_3$ after electronic excitation mainly of G will be presented. These measurements were performed to check the suitability of the transient absorption experiment presented in Chapter 2 for a further, thorough investigation of the

G·C base pair. The focus in the data analysis was on spectral characteristics, since the temporal evolution of the observed transient absorption is quite similar for all investigated monomers and dimers. A thorough data analysis yields the transient spectrum of a G·C specific intermediate that shows a remarkable resemblance with the spectrum of the deprotonated guanine radical, in short $(G-H)^{\bullet}$,[23,24] and is therefore a strong evidence for the existence of an EDPT process during the deactivation.

7.2 EXPERIMENTAL DETAILS

MATERIALS

2′,3′,5′-O-(Tert-butyldimethylsilyl) protected nucleosides were synthesized following a modified protocol of Ogilvie.[25] Anhydrous $CHCl_3$ (stabilized with amylene) was purchased from Sigma Aldrich and additionally dried with molecular sieve to remove residual water. Solvent and sample purity were checked via UV/vis and IR absorption spectroscopy.

TRANSIENT ABSORPTION MEASUREMENTS

All measurements were carried out using the transient absorption experiment described in Chapter 2 following photoexcitation at $\lambda_{pump} = 260$ nm. Optical densities of 0.2 and 1.0 at an optical pathlength of 0.1 mm were used for all measurements. These optical densities mark the approximate lower and upper limits for transient absorption measurements for nucleosides in $CHCl_3$. The optical pathlength of 0.1 mm was chosen to keep the intensity of coherent artifact as low as possible. $CHCl_3$ at an optical pathlength of 1 mm produces coherent signals with intensities on the order of $\Delta OD = 20 \times 10^{-3}$ and a duration of $\approx$ 500 fs, making a reliable analysis in this time range difficult. Since $C(TBDMS)_3$ in $CHCl_3$ is particularly sensitive to photochemical damage, the measurement at higher optical densities than 0.2 turned out to be impossible due to the accumulation of photoproducts. For the same reason, transient absorption of C was measured with only 500 single measurements per delay step. G and G·C were measured using 3500 single measurements per delay step. Transient absorption of both concentrations for each molecule and the neat solvent were measured in one experimental run to avoid a change of coherent solvent signals (cf. Chapter 2). Each sample and solvent measurement was repeated three times to ensure reproducibility.

The purity and integrity of the samples was checked before and after each measurement via UV/vis absorption spectroscopy. The water content was reduced by preparing all sample solutions with anhydrous $CHCl_3$ in a flow box purged with dry air and checked before and after the transient absorption measurements via IR spectroscopy.

The concentrations of monomers ([M]) and homodimers ([M · M]) were calculated using the degree of association

$$\beta = \frac{2\,[M \cdot M]}{c_0} = \frac{c_0 - [M]}{c_0}$$

with the initial concentration $c_0 = [M] + 2[M \cdot M]$. Given the association constant

$$K_{M \cdot M} = \frac{[M \cdot M]}{[M]^2} = \frac{\beta}{2c_0[1-\beta]^2}\,,$$

the degree of association can be calculated according to

$$\beta = \frac{1 + 4K_{M \cdot M}c_0 - \sqrt{1 + 8K_{M \cdot M}c_0}}{4K_{M \cdot M}c_0}\,.$$

For heterodimers M·N, assuming an equimolar mixture with $c_0 = [M]_0 = [N]_0$, the degree of association is given by

$$\beta = \frac{[M \cdot N]}{c_0} = \frac{c_0 - [M]}{c_0} = \frac{c_0 - [N]}{c_0}$$

with the initial concentration $c_0 = [M] + [M \cdot N] = [N] + [M \cdot N]$. Consequently, the association constant

$$K_{M \cdot N} = \frac{[M \cdot N]}{[M][N]} = \frac{\beta}{c_0[1-\beta]^2}$$

can be used for calculation of the degree of association according to

$$\beta = \frac{1 + 2K_{M \cdot N}c_0 - \sqrt{1 + 4K_{M \cdot N}c_0}}{2K_{M \cdot N} \times c_0}\,.$$

The initial concentrations and degrees of association used for the time-resolved measurements are summarized in Table 7.1.

Table 7.1: Initial concentrations ($c_0 = [M]_0$ for homodimers M·M, $c_0 = [M]_0 = [N]_0$ for heterodimers M·N) used for the transient absorption experiments in $CHCl_3$ and corresponding degrees of association β. The association constants K_{ass} are taken from Schwalb et al.[20,21] and refer to $K_{ass} = K_{[M]\cdot[M]}$ and $K_{ass} = K_{[M]\cdot[N]}$ for homo- and heterodimers, respectively.

Monomers	K_{ass} / M^{-1}	c_0 / mM	β
G	1010 ± 200	1.5	0.57
G	1010 ± 200	7.7	0.78
C	42 ± 2	10	0.35
G, C	$(3.4 \pm 0.8) \times 10^4$	1.1	0.85
G, C	$(3.4 \pm 0.8) \times 10^4$	5.6	0.93

G AND C

Excitation of G and C in $CHCl_3$ at $\lambda_{pump} = 260$ nm leads to transient absorption changes that are represented in Figure 7.1 as two-dimensional maps. The results of G for both initial concentrations are virtually identi-

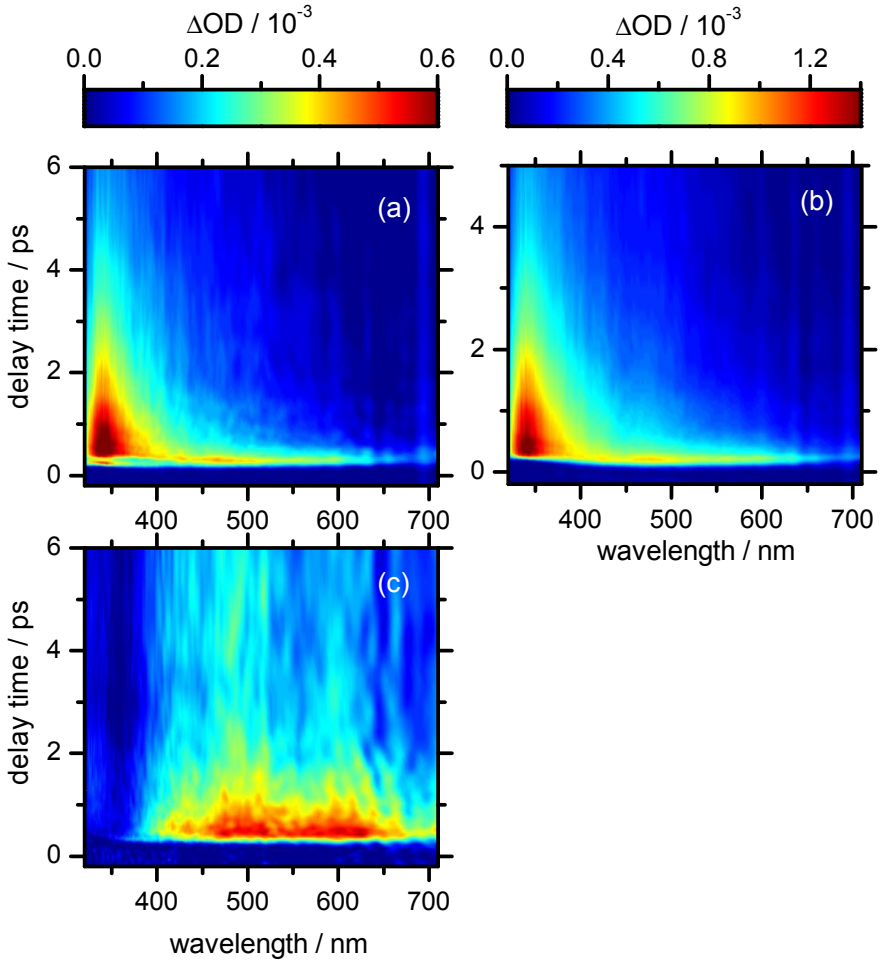

Figure 7.1: Two-dimensional maps of transient absorption changes of G in $CHCl_3$ with (a) $[G]_0 = 1.5$ mM and (b) $[G]_0 = 7.7$ mM, and (c) C in $CHCl_3$ with $[C]_0 = 10$ mM after excitation at 260 nm.

cal and feature two positive, strongly overlapping absorption bands, one around $\lambda_{probe} \approx 350$ nm and a broad and unstructured band at $\lambda_{probe} \geqslant 400$ nm. The slightly delayed rise of the absorption in the UV is caused by stimulated emission. A preliminary data analysis in the time domain show that the decay behavior found for the two concentrations are similar both in amplitudes and decay times, thus preventing a reliable distinction of monomer and dimer contributions. An unambiguous correlation with the degrees of association β could not be found in the global data analysis.

The recorded signal of C at $[C]_0 = 10$ mM shows two spectral characteristics, the first one being a broad and unstructured positive absorption band at visible probe wavelengths which can be assigned to excited state absorption. The second is a weak negative contribution at UV wavelengths attributed to stimulated emission (SE). Both bands show no significant spectral shifts. The signal of C is much less intense than the signal of G as is common for this nucleobase in aqueous solution.[26]

Generally, it can be stated that the population of long-lived states can be excluded for all investigated molecules on the basis of additional measurements at $\lambda_{probe} = 244$ nm. The obtained time profiles (not shown) revealed a ground state recovery on the time scale of ≈ 10 ps that reflects the time scale of vibrational cooling, which is much less efficient in $CHCl_3$ than in H_2O.[27–30] Since this process is slower than the observed excited state depopulation, the determination of overall electronic excited state lifetimes is not possible by following the ground state recovery.

G·C BASE PAIR

The transient absorption measurements of the G·C were performed at two initial concentrations of G and C, the corresponding degrees of association of the heterodimer are given in Table 7.1. The respective two-dimensional representations of transient absorption changes after excitation at 260 nm are depicted in Figure 7.2(c) and (d). Both concentrations give rise to three overlapping ESA bands with maxima at $\lambda_{probe} \approx 340$ nm, ≈ 400 nm and ≈ 480 nm. The initial delayed rise at UV wavelength is caused by stimulated emission, as was found for G and C. A preliminary data analysis of G·C, G and C signals in the time domain shows decay times on altogether comparable time scales. The simple comparison of decay times is therefore not sufficient for identification of G·C specific signals.

Instead, the *spectral* characteristics of G·C on the one hand and G and C on the other hand were examined. For comparison with the lower G·C concentration, the mathematical sum of G and C was calculated using the results of G at $[G]_0 = 1.5$ mM and C at $[C]_0 = 10$ mM. Each data set was scaled to $[G]_0 = [C]_0 = 1.1$ mM and weighted according to their respective extinction coefficient at 260 nm. For comparison with the higher concentration of G·C, the sum of G at $[G]_0 = 7.7$ mM and C at $[C]_0 = 10$ mM, each scaled to 5.6 mM, was calculated accordingly. The results are depicted in Figure 7.2(a) and (b). A comparison of these results with the G·C results (Fig. 7.2(c) and (d)) reveal that the ESA band at $\lambda_{probe} \approx 400$ nm is a contribution from the G·C pair that is present neither for "pure" G nor "pure" C, as was expected considering the spectral shapes of the contributing signals (cf. Sec. 7.3).

A more precise picture can be derived from the difference spectra of measured and calculated transient absorption changes, which are given in Figure 7.2(e) and (f). The respective transient absorption arise exclusively from the G·C base pair and show three positive ESA bands with a distinct

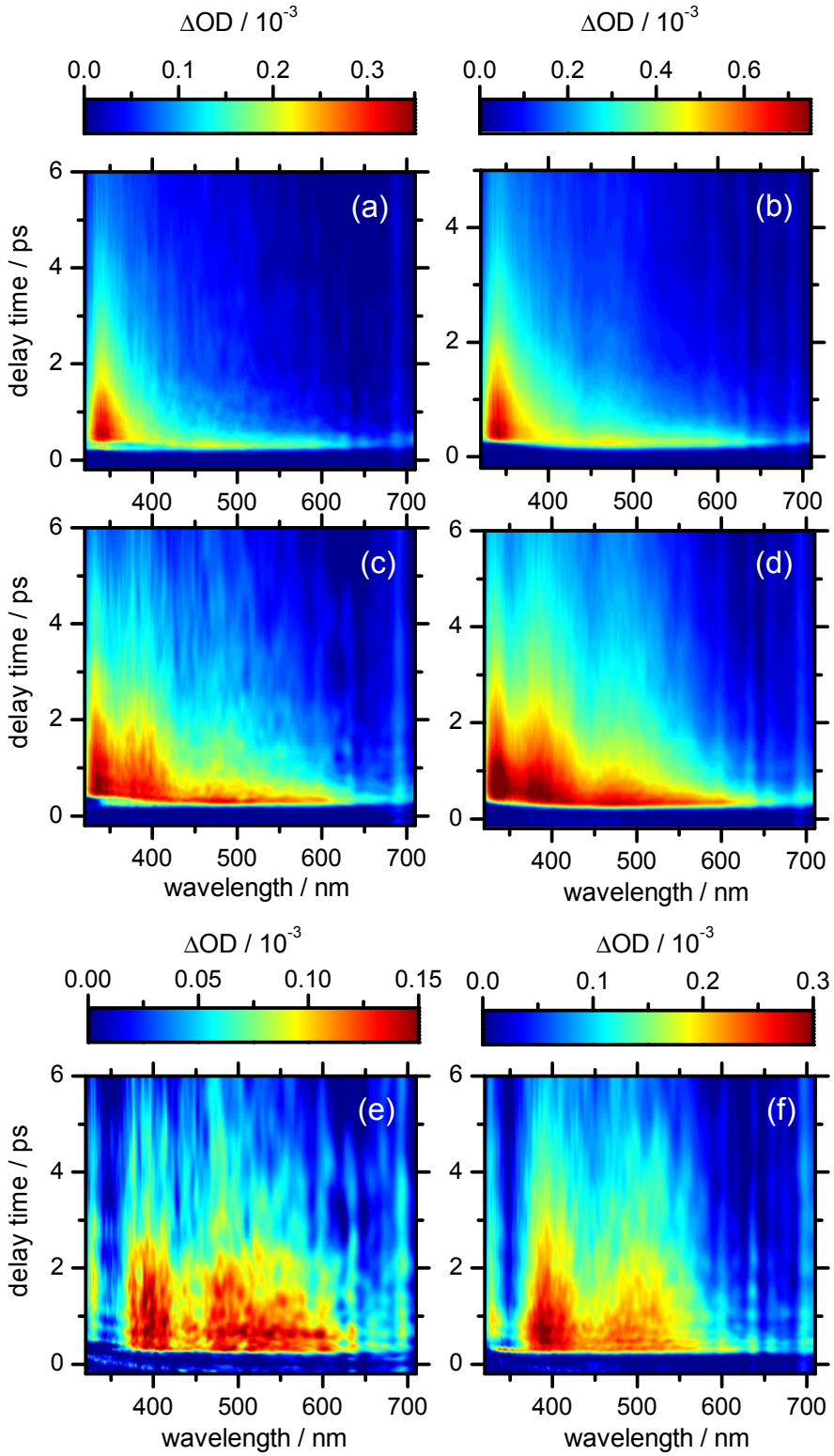

Figure 7.2: Top row: calculated sums of transient absorption of G and C. (a) Scaled sum of G and C maps shown in Fig. 7.1(a) and (c) (each scaled to $[G]_0 = [C]_0 = 1.1$ mM), (b) scaled sum of G and C maps shown in Fig. 7.1(b) and (c) (each scaled to $[G]_0 = [C]_0 = 5.6$ mM) after excitation at 260 nm (see text for details). Middle row: two-dimensional maps of transient absorption changes of G·C in $CHCl_3$ at (c) $[G]_0 = [C]_0 = 1.1$ mM and (d) $[G]_0 = [C]_0 = 5.6$ mM. Bottom row: difference of the G·C results and the calculated sums for (e) $[G]_0 = [C]_0 = 1.1$ mM and (f) $[G]_0 = [C]_0 = 5.6$ mM. Especially the latter map shows the signal of the G·C base pair without residual G and C contribution.

maximum at ≈ 400 nm and less pronounced bands around ≈ 340 nm and ≈ 480 nm. This result will be discussed in the following.

7.4 DISCUSSION

The difference spectrum of the simulated G+C signal and the G·C measurement at $\Delta t = 2$ ps after excitation is shown in Figure 7.3 together with the spectrum of the (G−H)$^{\bullet}$ radical that is known from literature.[23] Both

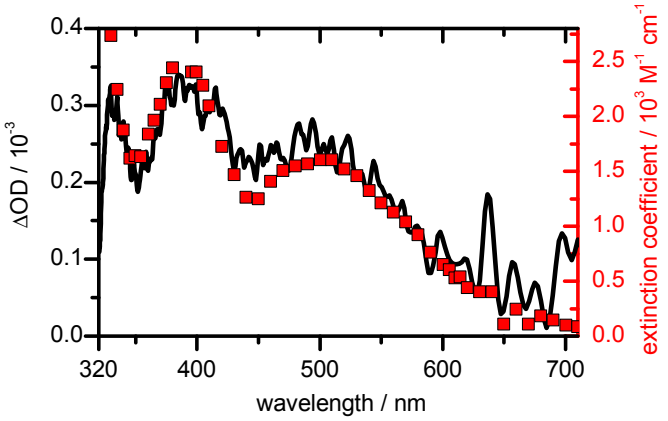

Figure 7.3: Transient difference spectrum at $\Delta t = 2$ ps (black line) and spectrum of (G−H)$^{\bullet}$ (red, taken from Candeias et al.[23]). The black axis on the left refers to the black spectrum, the red axis on the right to the red spectrum.

spectra show a close resemblance, which is a strong hint at the existence of the theoretically predicted EDPT process, during which the (G−H)$^{\bullet}$ radical is an important intermediate. A data analysis of the temporal evolution of the difference spectrum revealed a lifetime of ≈ 3 ps for the G·C specific transient absorption signal. Together with the immediate presence of the respective signal, this shows that the at least in $CHCl_3$ the radical state is immediately formed and lives for several picoseconds before relaxation to the electronic ground state occurs.

It has to be noted at this point that a possible charge-transfer-to-solvent (CTTS) state is known to be accessible for halocarbon solvents. In this state, an electron is transferred to a solvent molecule, thus forming $CHCl_2^{\bullet}$ and solvated Cl^-. The geminate recombination of electron and oxidized species of comparable systems have been determined to be on the order of some tens or hundreds of ps, as was shown by Kohler and coworkers.[31,32] These time scales differ dramatically from the ones found for the deactivation times of G and C in $CHCl_3$ and therefore, it can safely be concluded that the involvement of CTTS is most unlikely.

In summary, the close spectral resemblance of the G·C specific ESA band found after electronic excitation of the G·C base pair with the spectrum of the (G−H)$^{\bullet}$ radical is a strong hint at the existence of an electron-driven

proton transfer as a possible deactivation mechanism. For a definite assignment, the absorption spectrum of the protonated C radical $(C+H)^{\cdot}$ as the second intermediate should be included in the data analysis. However, the respective spectrum is not yet published in the literature to the best of the author's knowledge.

The results presented in this Chapter showed that further investigations of the G·C base pair with transient absorption spectroscopy are promising. The use of different concentrations and excitation wavelengths might help revealing the details of the G·C base pair specific deactivation pathway.

BIBLIOGRAPHY

[1] Ingham, K.; El-Bayoumi, M. A. *J. Am. Chem. Soc.* **1974**, *96*, 1674–1682.

[2] Fuke, K.; Kaya, K. *J. Phys. Chem.* **1989**, *93*, 614–621.

[3] Takeuchi, S.; Tahara, T. *J. Phys. Chem. A* **1998**, *102*, 7740–7753.

[4] Douhal, A.; Kim, S. K.; Zewail, A. H. *Nature* **1995**, *378*, 260–263.

[5] Sekiya, H.; Sakota, K. *J. Photochem. Photobiol., C* **2008**, *9*, 81–91.

[6] Schultz, T.; Samoylova, E.; Radloff, W.; Hertel, I. V.; Sobolewski, A. L.; Domcke, W. *Science* **2004**, *306*, 1765–1768.

[7] Ottiger, P.; Frey, J. A.; Frey, H.-M.; Leutwyler, S. *J. Phys. Chem. A* **2009**, *113*, 5280–5288.

[8] Ottiger, P.; Leutwyler, S.; Köppel, H. *J. Chem. Phys.* **2009**, *131*, 204308.

[9] Sobolewski, A. L.; Domcke, W. *Chem. Phys.* **2003**, *294*, 73–83.

[10] Sobolewski, A. L.; Domcke, W. *Phys. Chem. Chem. Phys.* **2004**, *6*, 2763–2771.

[11] Sobolewski, A. L.; Domcke, W.; Hattig, C. *Proc. Natl. Acad. Sci. U.S.A.* **2005**, *102*, 17903–17906.

[12] Yamazaki, S.; Taketsugu, T. *Phys. Chem. Chem. Phys.* **2012**, *14*, 8866–8877.

[13] Groenhof, G.; Schäfer, L.; Boggio-Pasqua, M.; Goette, M.; Grubmüller, H.; Robb, M. A. *J. Am. Chem. Soc.* **2007**, *129*, 6812–6819.

[14] Markwick, P. R. L.; Doltsinis, N. L. *J. Chem. Phys.* **2007**, *126*, 175102.

[15] Markwick, P. R. L.; Doltsinis, N. L.; Schlitter, J. *J. Chem. Phys.* **2007**, *126*, 045104.

[16] Alexandrova, A. N.; Tully, J. C.; Granucci, G. *J. Phys. Chem. B* **2010**, *114*, 12116–12128.

[17] Zelený, T.; Ruckenbauer, M.; Aquino, A. J.; Müller, T.; Lankaš, F.; Dršata, T.; Hase, W. L.; Nachtigallova, D.; Lischka, H. *J. Am. Chem. Soc.* **2012**, *134*, 13662–13669.

[18] Guallar, V.; Douhal, A.; Moreno, M.; Lluch, J. M. *J. Phys. Chem. A* **1999**, *103*, 6251–6256.

[19] Abo-Riziq, A.; Grace, L.; Nir, E.; Kabelac, M.; Hobza, P.; de Vries, M. S. *Proc. Natl. Acad. Sci. U.S.A.* **2005**, *102*, 20–23.

[20] Schwalb, N. K.; Temps, F. *J. Am. Chem. Soc.* **2007**, *129*, 9272–9273.

[21] Schwalb, N. K.; Michalak, T.; Temps, F. *J. Phys. Chem. B* **2009**, *113*, 16365–16376.

[22] Biemann, L.; Kovalenko, S. A.; Kleinermanns, K.; Mahrwald, R.; Markert, M.; Improta, R. *J. Am. Chem. Soc.* **2011**, *133*, 19664–19667.

[23] Candeias, L. P.; Steenken, S. *J. Am. Chem. Soc.* **1989**, *111*, 1094–1099.

[24] Rokhlenko, Y.; Geacintov, N. E.; Shafirovich, V. *J. Am. Chem. Soc.* **2012**, *134*, 4955–4962.

[25] Ogilvie, K. K. *Can. J. Chem.* **1973**, *51*, 3799–3807.

[26] Malone, R. J.; Miller, A. M.; Kohler, B. *Photochem. Photobiol.* **2003**, *77*, 158–164.

[27] Rothschild, W. G.; Rosasco, G. J.; Livingston, R. C. *J. Chem. Phys.* **1975**, *62*, 1253–1268.

[28] Graener, H.; Seifert, G. *J. Chem. Phys.* **1993**, *98*, 36–45.

[29] Graener, H.; Zürl, R.; Hofmann, M. *J. Phys. Chem. B* **1997**, *101*, 1745–1749.

[30] Sibert, E. L.; Rey, R. *J. Chem. Phys.* **2002**, *116*, 237–257.

[31] Peon, J.; Hess, G. C.; Pecourt, J.-M. L.; Yuzawa, T.; Kohler, B. *J. Phys. Chem. A* **1999**, *103*, 2460–2466.

[32] Xia, C.; Peon, J.; Kohler, B. *J. Chem. Phys.* **2002**, *117*, 8855–8866.

8

SUMMARY AND OUTLOOK

The main goal of this Thesis was the investigation of the complex interplay of structural modifications and hydrogen bonds on the ultrafast electronic deactivation dynamics of DNA and rare RNA building blocks. The obtained results provided insight into the crucial role of substitution pattern and steric restraints on the purine backbone. Generally, the investigation of deactivation mechanisms in DNA building blocks is a rather challenging task for two reasons: First, the depopulation of electronically excited states takes place on a femtosecond to picosecond time scale, thus calling for femtosecond time-resolved spectroscopic techniques such as fluorescence up-conversion and transient absorption spectroscopy. The second challenge arises from the low fluorescence and transient absorption signals of DNA and RNA building blocks, which makes the use of spectroscopic techniques with high sensitivities inevitable.

8.1 TRANSIENT ABSORPTION SETUP

A major part of the present Thesis project was the development of a new, highly sensitive and versatile transient absorption experiment. The respective setup, shown schematically in Figure 8.1, allows for a simultaneous measurement of broadband transient absorption spectra in the wavelength range $310 - 700$ nm and the additional detection of transient absorption at a single wavelength, which was used for the detection of vibrational cooling and ground state recovery in the deep UV. A 1 kHz readout-rate

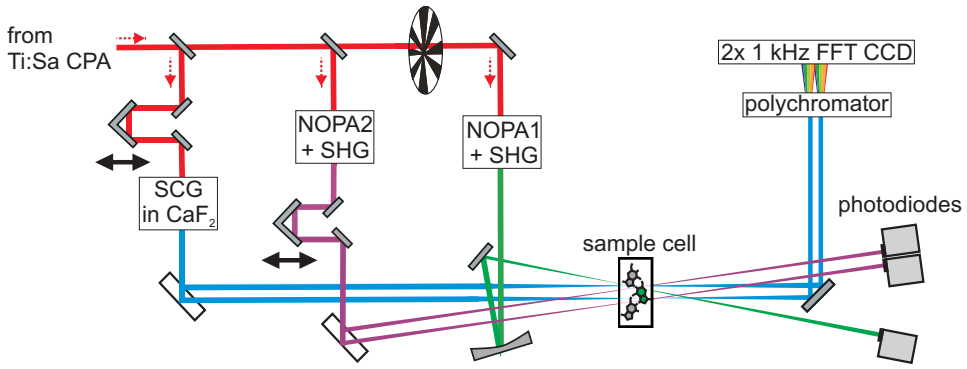

Figure 8.1: Scheme of the femtosecond transient absorption setup for simultaneous UV/VIS broadband and deep-UV single-color measurements.

and the implementation of a single-shot data analysis allowed for measurements with typical sensitivities of the order of 2×10^{-5} and 5×10^{-6} for broadband and single-color detection, respectively. The time resolution was of the order of $\Delta\tau \approx 50$ fs (broadband) and $\Delta\tau \approx 80$ fs (single-color). The setup was optimized to ensure a straightforward, stable and repro-

ducible operation that can be adjusted to the individual needs of different samples within a reasonable amount of time. The capability of this experiment was proved investigating a number of different samples, which will be summarized below.

Further improvement of the transient absorption setup is possible by extending the probe wavelength range down to $\lambda_{probe} = 270$ nm by using the frequency-doubled laser fundamental at 387 nm for supercontinuum generation in CaF_2. This would require a careful investigation of the necessary modifications regarding focus size, pulse length, and pulse intensity in the crystal as well as a characterization of the stability of the supercontinuum. An extended probe wavelength range would make the improvement of spectral resolution, in particular in the UV range, desirable. This could be done by implementation of FFT-CCD sensors with larger sensor areas.

The present setup forms the basis for a number of other experiments. The high sensitivities makes the implementation of a femtosecond time-resolved stimulated Raman experiment and transient absorption measurements of highly sensitive samples in a single shot mode possible. The single color probe pulse can in principle be set to any wavelength, and a simple setup for UV pump-IR single color probe experiment is accessible by tuning the second NOPA to the near-IR region and using IR sensitive photodiodes. Furthermore, the transient absorption setup can easily be transformed to a pump-repump-broadband probe or pump-dump-broadband probe experiment. This requires a second chopper that needs to be placed in the single-color probe beam which then serves as the second pump pulse. The chopper must be set to a frequency that equals 1/4 of the laser frequency, which results in the pulse trace schematically shown in Figure 8.2. The pulses at position 1 result in a pump-repump-probe signal, po-

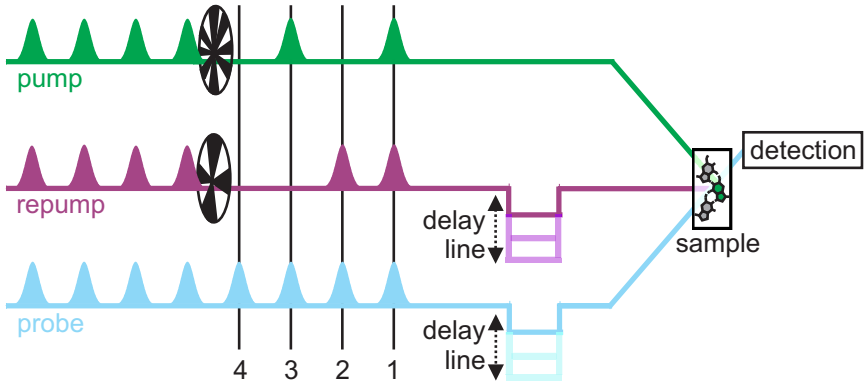

Figure 8.2: Schematic overview of the pump-repump-probe transient absorption experiment.

sition 2 in the repump-probe signal, position 3 in a pump-probe signal and position 4 is the background signal for all preceding pulses. Both the repump and probe pulses can be delayed individually with respect to the pump pulse. The necessary LabVIEW program and the setup were written and tested in this Thesis. This experiment could be useful for the investigation of multichromophores or the control of complicated photoinduced

reactions such as the ring closure and opening reactions of fulgides and in the analysis of state couplings in multichromophor DNA base systems.

8.2 STRUCTURALLY MODIFIED 6-OXOPURINES

Two structurally modified 6-oxopurines, namely xanthosine monophosphate (XMP) and hypoxanthine (Hyp), both of which are rare RNA bases and structurally related to guanine, were investigated using a combination of the above described femtosecond time-resolved transient absorption experiment and fluorescence up-conversion spectroscopy.

The xanthine chromophore, shown in Figure 8.3(a) and (b), features a carbonyl group at the C(2) position and therefore no double bond at C(2)-N(3). It is known from literature that this leads to an increase of acidity that

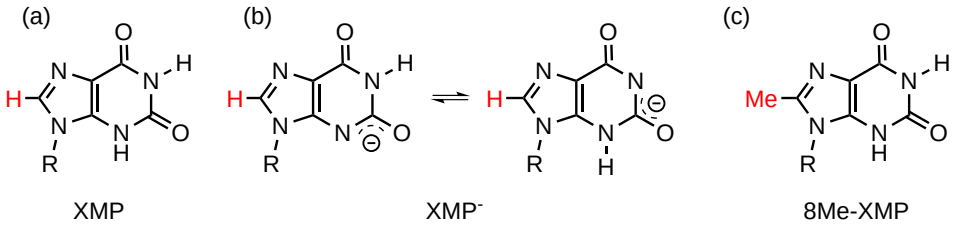

Figure 8.3: Structures of (a) neutral xanthosine monophosphate (XMP) and (b) deprotonated xanthosine monophosphate (XMP^-). R corresponds to ribosyl monophosphate. (c) Structure of 8-methyl-xanthosine monophosphate. The substituents at the C(8) position are colored.

is unique among the purine nucleotides: At pH$\geqslant$ 5.5, the xanthine moiety is deprotonated, and the negative charge is located either at the N(3) or N(1) position. As was discussed, the neutral and the anionic xanthine moiety might feature quite similar electronic structures in the electronic ground state. This interpretation was supported by time-resolved transient absorption and fluorescence up-conversion measurements at different excitation wavelengths on both the neutral (XMP) and anionic (XMP^-)[1] nucleotide. The results showed a similar spectro-temporal behavior for both species, which was dominated by two time scales for both XMP and XMP^-, namely

$$\tau_1 \approx 0.3 \pm 0.1 \text{ ps},$$
$$\tau_2 \approx 1 \pm 0.2 \text{ ps}.$$

Based on the spectral characteristics, the sub-picosecond component was assigned to depopulation of the initially excited Franck-Condon region. The detection of the ground state recovery (GSR) in the deep UV showed that the main part of the initially excited molecules return to the electronic ground state within τ_2. Consequently, this decay time was attributed to the barrierless evolution of the wavepacket in the direction of a conical intersection with the electronic ground state. The relaxation coordinate is

1 The charge of the phosphate group is omitted in this notation.

most likely the out-of-plane deformation of the five-membered ring, as it was theoretically proposed for xanthine by Yamazaki, Sobolewski and Domcke. Selective excitation in the first or second electronically excited state leads to virtually identical results, suggesting an ultrafast conversion into the lower excited state on a time scale that is below the experimental time resolution. For XMP^-, a third, minor important component decaying with $\tau_3 = 4 \pm 1$ ps with amplitudes of a few percent was found. Apparently, some part the excited-state population relax through a less favored deactivation channel, tentatively assigned to the out-of-plane deformation of the six-membered ring. This pathway is crucial for the electronic relaxation of other 6-oxopurines, but less favored in case of xanthine. A further investigation of the deactivation mechanism of XMP is possible by methylation at the C(8) position, shown in Figure 8.3(c). The methyl group might induce steric restraints and consequently energy barriers for the out-of-plane deformation of the five-membered ring, if this is the main relaxation coordinate.

The second investigated structurally modified 6-oxopurine was hypoxanthine (Fig. 8.4(a)), which is structurally closely related to guanine, but lacks the exocyclic amino group at the C(2) position. The results of time-

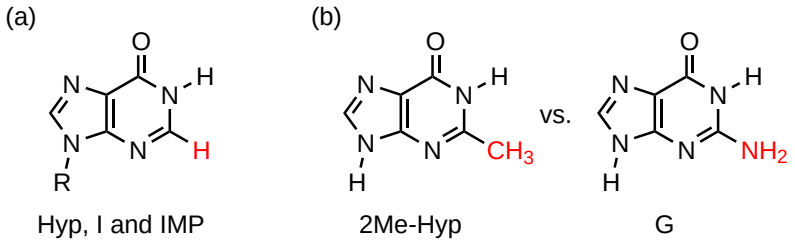

Figure 8.4: (a) Structures of hypoxanthine (Hyp, R = H), inosine (I, R = ribosyl) and inosine monophosphate (IMP, R = ribosyl monophosphate). (b) Structures of 2-methyl-hypoxanthine and guanine. The substituents at the C(2) position are colored. The methyl group induces only a sterical hindrance of the out-of-plane deformation of the six-membered ring, the amino group is responsible for electronic and steric effects, and the H-atom causes neither of these effects.

resolved fluorescence and absorption spectroscopy of Hyp, its nucleoside inosine (I) and nucleotide inosine monophosphate (IMP) in water revealed a rapid relaxation after excitation at $\lambda_{pump} = 260$ nm back to the electronic ground state within

$$\tau_1 \leqslant 0.21 \pm 0.08 \text{ ps}$$

through a conical intersection. Subsequent vibrational cooling was found to occur with a decay time of

$$\tau_2 = 1.8 \pm 0.4 \text{ ps}.$$

The relaxation coordinate is expected to be the out-of-plane deformation of the six-membered ring, which was proposed to be the most important deactivation pathway for other purine nucleosides. The picture obtained for Hyp was explained by the absence of the large amino group at the C(2) position, which leads to a barrierless relaxation to the electronic ground state. This interpretation hints at the crucial role that the C(2) position plays for the deactivation of guanine. Here, it is known from literature that the deactivation is characterized by at least one minimum or planar region, leading to a complex excited-state depopulation. A further investigation on the question whether electronic or steric effects are responsible for the difference between guanine and hypoxanthine is possible by substitution of the H(2) proton by a methyl group. The situation is depicted in Figure 8.4(b).

8.3 HYDROGEN-BONDED SYSTEMS

The results obtained for Hyp, I and IMP in water formed the basis for an investigation of the influence of hydrogen bonds on the deactivation dynamics of the inosine dimer, shown in Figure 8.5(a). This system was cho-

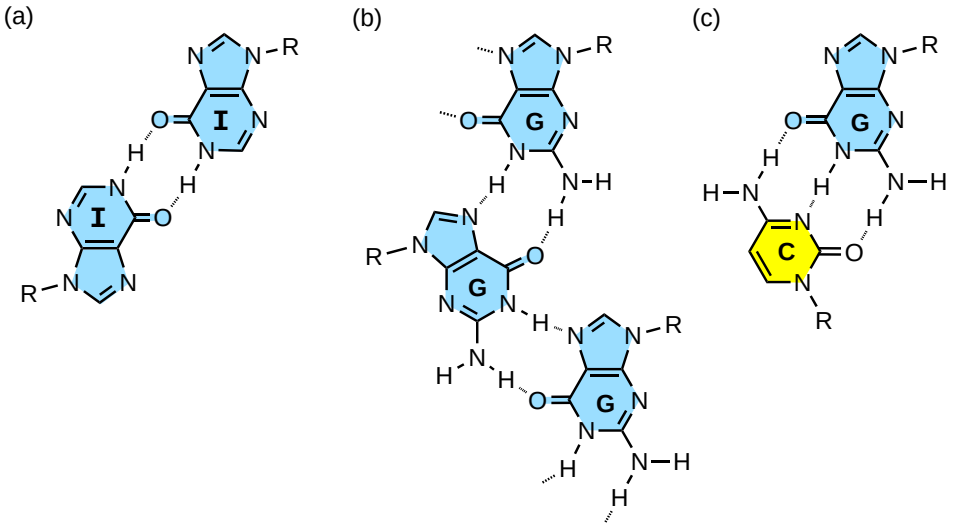

Figure 8.5: Structures of the hydrogen-bonded assemblies that were investigated in this Thesis: (a) Inosine dimer in $CHCl_3$, (b) example of a guanine assembly in *n*-hexane, (b) G·C Watson-Crick base pair in $CHCl_3$. R corresponds to 2′,3′,5′-O-TBDMS protected ribosyl residues. The 6-oxopurine backbones are highlighted in blue, the pyrimidine backbone in yellow.

sen because of its well-defined structure that is formed in aprotic solvents. The formation of the dimer was thoroughly characterized by temperature-

and concentration dependent 1D and 2D ^{1}H NMR, IR and UV/vis spectroscopy and an association constant of

$$K_{I\cdot I} = 690 \pm 200 M^{-1}$$

was found. The picture that emerged from transient absorption experiments after excitation at $\lambda_{pump} = 260$ nm is similar to that of the monomer in water: Electronic excitation at $\lambda_{pump} = 260$ nm leads to a rapid depopulation of the excited state within

$$\tau \approx 0.1 \text{ ps}$$

through a conical intersection with the electronic ground state. The partial overlapping of the respective signals with hot ground state absorption, which decayed within 9 ± 1 ps, made the accurate determination of the electronic excited state lifetime difficult. However, the picture that was obtained for the electronic deactivation dynamics resembled that of the monomer in water. On the basis of these results, it was concluded that dimerization does not lead to a complete change of the deactivation mechanism via the out-of-plane deformation of the six-membered ring. Consequently, this supports the outstanding importance of the C(2) position for the electronic deactivation of 6-oxopurines, since neither the C(2) nor the N(3) atom are involved in the dimerization, but are crucial for the deformation of the 6-membered ring. The straightforward results obtained for the inosine dimer qualifies it as a test case for more complicated systems such as the G·C and the A·T base pairs.

A completely different picture emerged for larger hydrogen-bonded aggregates, mostly ribbons, of guanosine in *n*-hexane. The aggregates were characterized using a combination of IR-, CD- and UV/vis spectroscopy. An exemplary ribbon structure is given in Figure 8.5(b). The combined results from time-resolved fluorescence and absorption experiments after excitation at $\lambda_{pump} = 260$ nm showed that the aggregation gives rise to complex excited-state dynamics on four time scales, namely

$$\begin{aligned}
\tau_1 &= 0.63 \pm 0.03 \text{ ps}, \\
\tau_2 &= 5.90 \pm 0.30 \text{ ps}, \\
\tau_3 &= 62.0 \pm 7.0 \text{ ps}, \\
\tau_4 &= 3.6 \pm 1.0 \text{ ns}.
\end{aligned}$$

The dynamics were attributed to a complex excited-state geometry and trapping of some part of excited-state population, possibly in an $n\pi^*$ state that is stabilized compared to that of guanine in water. Besides these solvent effects, sizable energy barriers en route to the electronic ground state could well be induced by numerous steric constraints in the assemblies. The transient spectra obtained at delay times $\geqslant 1$ ns after excitation

showed no resemblance to the spectra of any species such as the (G−H)$^{\cdot}$ H-abstraction product, or triplet species like the ^{3}G$^{\cdot}$ radical or ^{3}GMP that are known as possible photoproducts of guanine. Additionally, the results from detection of the ground state recovery gave no evidence for such persistent species. A recent investigation on the same system by Kleinermanns, Kovalenko and coworkers claimed the formation of a (G−H)$^{\cdot}$ radical after excitation at $\lambda_{pump} = 284$ nm and consequently the existence of an electron-proton transfer in the guanine assemblies. However, the respective radical should be present in the results obtained in this Thesis as well, and the absence makes the definite assignment to such a deactivation mechanism questionable.

Beside the above discussed assemblies made up of one monomeric building block, the excited-state dynamics of the Watson-Crick G·C dimer in $CHCl_3$ were investigated after excitation at $\lambda_{pump} = 260$ nm, which leads to absorption of excitation photons mainly by the guanine chromophores. As was discussed in Chapter 1.2.3, an electron coupled proton transfer (EDPT) from G to C, i.e., the population of an intermediate CT state with (G−H)$^{\cdot}$ and (C+H)$^{\cdot}$ radicals, was predicted theoretically to be an important relaxation pathway that leads to an ultrafast return to the electronic ground state, where electron and proton are transferred back to G. However, a recent experimental investigation on the G·C dimer did not lead to the observation of such a process, and the authors proposed the deactivation by monomer-like mechanisms. In opposition to that, time-resolved transient absorption experiments on the G·C base pair and a qualitative data analysis that were performed in this Thesis gave evidence for the existence of a (G−H)$^{\cdot}$ radical with a lifetime of $\approx$ 3 ps, which is the first direct observation of the EDPT process in the Watson-Crick G·C base pair.

Further investigations of the impact of hydrogen bonds on the deactivation mechanism can be done using a number of possible systems, such as combinations of hypoxanthine and guanosine. Another interesting aspect is the investigation of the G·C base pair in water. Since base pairing of free nucleobases is not favored in water due to ubiquitous H-bond donors and acceptors, a "caged" structure would be necessary to enforce dimerization. This would require a careful analysis of optimal linker length and structure as it was already performed successfully for a small G·C double strand in the PhD Thesis of M. Stuhldreier. H. Nicken found in his PhD thesis evidence for an efficient, radiationless deactivation mechanism in a 5-aminoindazole-indazole dimer after excitation of the indazole which might also be a proton transfer reaction as was found for the G·C base pair. The investigation of this system in solution might help shedding light on the respective relaxation pathway. From the experimental point of view, the investigation of hydrogen-bonded species with femtosecond time-resolved UV pump-IR probe spectroscopy would be desirable. These experiments provide direct insight into the geometrical changes in the electronic excited states.

APPENDIX

A

TRANSIENT ABSORPTION LABVIEW PROGRAM

The most important features of the LabVIEW program that was written for the transient absorption experiment will be explained in the following. All positions and distances of the delay stages are given in fs for convenience. In Figure A.1, the complete user interface of the transient absorption program is shown. The following controls and indicators of experimental parameters are displayed:

- **Message** gives the current status, i.e. the type of experiment which is currently running or error messages. A running measurement is also indicated by the green light labeled "busy".
- **Current position (fs)** gives the current positions of delay stages for broadband (whitelight) and single color (NOPA Probe) detection.
- The controls labeled with **Sample** etc. can be filled by the user and are written in a file that contains the respective information.
- The four **graphs** in the middle and right column show the results of current measurements. They are updated on-line after measurement at each delay step.
- **File path** can be set by the user and is the default file path for saving the measured data. After each measurement, a dialog will show up that allows to set file path and file name.

The runtime menu **Measure** includes the following menu items:

- **Set delays** allows to set the number and size of delay steps and maximum delay time for a temporal scan. The respective scan profile consists of three parts: A linear one, which is usually used for the measurement of the baseline before the experimental time zero, a second part with linear step sizes, which is used for the temporal scan at delay times up to $\approx$ 1 ps after the experimental time zero. For the third part, the step sizes are increased exponentially. The respective LabVIEW routine is based on a LabVIEW program written by F. Renth.
- **Set delays (two exponential steps)** allows to set the number and size of the delay steps and maximum delay time for a temporal scan as described above, but additionally, another part of the scan profile with larger exponentially increasing step sizes is included to reduce the number of delay steps. This is the preferred scan mode.
- **Take CCD measurement** starts a live scan of camera and photodiode signals.

- **Take optimization measurement** allows to measure the change of optical density without moving the delay stages.
- **Take temporal scan** starts a temporal scan of broadband and single color detection with the defined temporal scan profile. The acquired data are saved at the end of the scan.

The runtime menu **Translation Stage** includes the following menu items:

- **Move absolute** allows to move the delay stages individually or synchronously to an absolute position.
- **Move relative** allows to move the delay stages individually or synchronously by a relative value.
- **Go home** moves both delay stages to a predefined home position (usually at the beginning of the delay stage).
- **Get position** updates the current position display on the main user interface.

The runtime menu **Whitelight Measurement** starts a temporal scan of the broadband detection. The acquired data are saved at the end of the scan.
The runtime menu **Calibration** starts the recording of the whitelight spectrum. The acquired data are saved.
The runtime menu **Photodiode Measurement** starts a temporal scan of the single color detection. The acquired data are saved at the end of the scan.

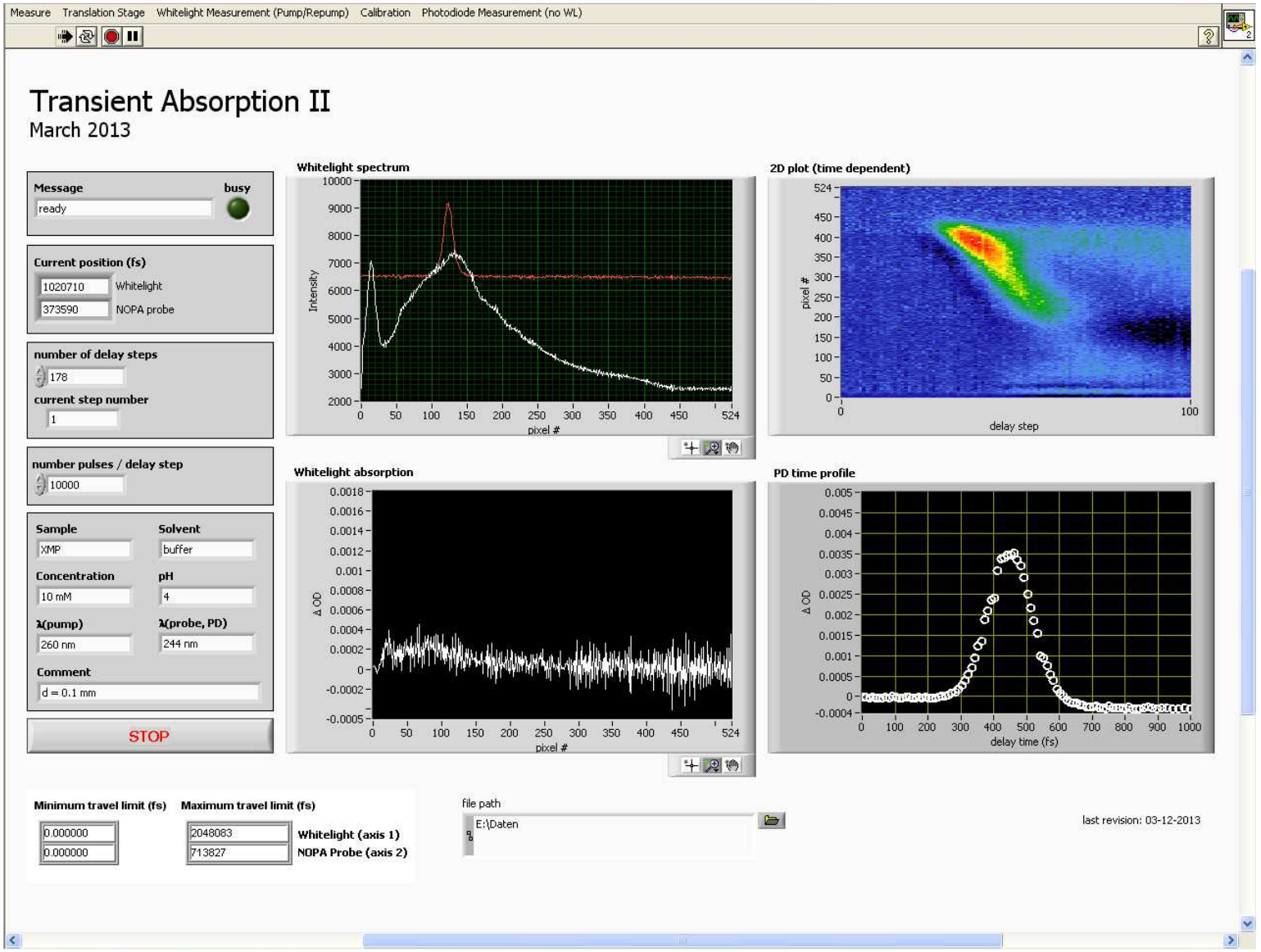

Figure A.1: Screenshot of the user interface of the LabVIEW program that was used for controlling the transient absorption experiment.

DANKSAGUNG

An erster Stelle möchte ich meinem Doktorvater Prof. Friedrich Temps für seine engagierte und wertvolle Unterstützung während der letzten Jahre danken. Seine ansteckende Leidenschaft für die Wissenschaft und sein unermüdlicher Einsatz für die Schaffung bester Arbeitsbedingungen haben diese Arbeit erst möglich gemacht.

Ganz besonders bedanken möchte ich mich bei allen aktuellen und ehemaligen Mitgliedern der Arbeitskreise Temps und Friedrichs für Zusammenhalt, Hilfsbereitschaft und alles Wissenschaftliche und Unwissenschaftliche, was ich von euch lernen durfte.

Dabei möchte ich vor allem Ron Siewertsen danken, dessen kompetente und geduldige Einführung in den Femtokeller und seine vielen Ratschläge und Hinweise wesentlich zu dieser Arbeit beigetragen haben. Mein Dank gilt auch Nina Schwalb und Falk Renth, die mir besonders in der Anfangszeit geholfen haben.

GD geht an Julia Bahrenburg für jahrelanges engstes Zusammensein in allen Lebens-, Studiums- und Institutslagen. Das muss man erstmal aushalten. Mayra Stuhldreier danke ich für alle gemeinsam durchlebten Stunden und Jahre außerhalb und innerhalb der Wissenschaft, und auch Alexander Thrun darf in diesem Absatz nicht fehlen: Danke nicht nur für alle Computer- und Latexlösungen, sondern auch für alles andere. Ihr habt für mich das meiste einfacher und vieles schöner gemacht. Bsf.

Auch allen anderen Kellerkindern, insbesondere Anja Köhntopp, Hendrikje Neumann, Ole Hüter und Uta Corinna Stange, danke ich sehr herzlich für die schöne und von großer Hilfsbereitschaft geprägte Zeit.

Prof. Frank Sönnichsen danke ich für die Übernahme der Zweitbetreuung dieser Arbeit, für die vielen NMR-Messreihen, die immer sehr fruchtbaren Diskussionen und die gelegentliche terminliche Spontanität.

Herrn Joachim Gripp gebührt mein Dank für seine geduldige Hilfe in allen Synthese-, Geräte- und sonstigen Fragen des Laboralltags und diverse Synthesen der geschützten Nukleobasen.

Den Mitarbeitern der Werkstatt, Klaus-Dieter Will, Frank Herzog, Frank Laasch und Andreas Sievers gilt großer Dank für die gelegentliche Planung und immer zügige Beschaffung diverser Bauteile und alle kurzfristigen Reparaturen, die im Laufe der Zeit gebraucht wurden, und für die

immerwährende gute Laune.

Den Herren Uwe Eggers, Klaus Warns und Michael Karstens danke ich herzlich für ihre immer schnelle und bereitwillige Unterstützung bei allen IT- und Elektroproblemen und ihre beständige Bereitschaft, mein Wissen in diesen und anderen Gebieten zu erweitern.

I would like to thank Rongrong "Tracy" Zhang for her seemingly endless capacity of cheerfulness and her help with the TA measurements, especially during my teaching duties.

"Meinen" Praktikanten, Hiwis und BSc-Kandidaten danke ich für ihren wissenschaftlichen Einsatz und die Bereicherung unseres AK-Lebens.

Thomas Michalak und den aktuellen und ehemaligen Mitarbeitern des Arbeitskreises Hartke gilt großer Dank für die Hilfe bei allen Gaussian- und ORCA-Problemen.

Thanks to the MBI crew, in particular Ming Yang, Łukasz Szyc, Henk Fidder, Erik Nibbering and Thomas Elsaesser, for introducing me to the wonders of photon echo spectroscopy. It was a pleasure working with you.

Bei Frau Ursula von der Heydt möchte ich mich sehr herzlich für die immer schnelle und oft unbürokratische Lösung aller kleinen und großen Probleme und viele schöne gemeinsame Stunden innerhalb und außerhalb der Uni bedanken. Tanja Sharif danke ich für die organisatorische Unterstützung während der letzten Monate dieser Arbeit.

Großer Dank geht auch an die Korrekturleser Julia, Mayra, Anja und Uta.

Meinen Freunden, den Kielern und den Soestern, möchte ich für Zeit, Zuversicht, Geduld und alles andere danken. Bessere Freunde kann man sich nicht wünschen.

Meinen Eltern und Geschwistern gilt mein größter Dank für ihre dauerhafte Unterstützung in jeder Hinsicht, und auch für die beständige Erweiterung meines kulturellen Horizonts in alle Richtungen.